

## AN ABSTRACT OF THE DISSERTATION OF

Andrea M. Allan for the degree of Doctor of Philosophy in Geography presented on  
August 16, 2012.

Title: Analyzing the Present and Future Pacific-North American Teleconnection using Global and Regional Climate Models

Abstract approved: \_\_\_\_\_  
Steven W. Hostetler

In this thesis I present the results of a comprehensive assessment of the Pacific-North American (PNA) teleconnection pattern in general circulation models (GCMs) and a regional climate model (RCM). The PNA teleconnection pattern is a quasi-stationary wave field over the North Pacific and North America that has long been recognized as a robust feature of Northern Hemisphere atmospheric circulation, and directly affects the interannual variability of North American temperature and precipitation. The teleconnection is evaluated under present (1950-2000) and future (2050-2100) climate in a coupled GCM (MPI/ECHAM5) and a high-resolution regional climate model (RegCM3). I further assess the PNA in 27 atmosphere-ocean GCMs and earth system models (ESMs) from the ongoing fifth phase of the Coupled Model Intercomparison Project (CMIP5). The National Centers for Environmental Prediction and Atmospheric Research (NCEP/NCAR) Reanalysis serves a quasi-observational baseline against which the models are evaluated. For each analysis, changes in the spatial and temporal patterns of the PNA spatial are assessed for both the present and future climates, and these changes are then related to changes in climate and surface hydrology in North America.

Coupling the NCEP and ECHAM5 GCMs with RegCM3 is very successful in that the PNA is resolved in both models with little loss of information between the GCMs and RegCM3, thereby allowing an assessment of high-resolution climate with an inherent skill comparable to that of the global models. The value of the PNA index is generally independent of the method used to calculate it: three- and four-point modified linear pointwise calculations for both the RegCM3 and ECHAM5 model simulations produce very similar indices compared with each other, and compared with those extracted from a rotated principle component analysis (RPCA) which is also used to determine the PNA spatial pattern. The spatial pattern of the PNA teleconnection emerges as a leading mode of variability from the RPCA, although the strength of the teleconnections are consistently weaker than NCEP as defined by four main “centers of action”. This discrepancy translates into the strength of the controls of the PNA on surface climate. Maps of the correlations between the GCM PNA indices and RCM surface climate variables are compared to the results from the NCEP/NCAR Reanalysis. I find that correlation patterns with temperature and precipitation are directly related to the positioning of the Aleutian low and Canadian high, the two main drivers of upper-atmospheric circulation in the PNA sector.

The CMIP5 models vary significantly in their ability to simulate the quasi-observed features of the PNA teleconnections. The behavior of the models relative to NCEP is more definite than the trends within the models. Most models are unable to resolve the temporal variability of NCEP; however, on the other hand most of the models are able to capture the PNA as a low-frequency quasi-oscillation. Many

of the models are unable to simulate the barotropic instability that initiates wave energy propagation through the 500-hPa geopotential height field, thereby leading to phase-locking and thus the positive and negative modes of PNA are indistinguishable. The behavior and the spatial patterns of the PNA throughout the 21<sup>st</sup> century are consistent with other projections of future climate change in that most models exhibit a lengthening of the eddy length scale and a poleward shift of the mid-latitude jet stream associated with polar amplification of greenhouse-gas driven global warming.

Finally, my analyses underscore the robustness of multi-model means, suggesting that the cumulative results of multiple climate models outperform the results from individual models because ensemble means effectively cancel discrepancies and hereby expose only the most robust common features of the model runs. While ensembles provide better representation of the average climate, they potentially mask climate dynamics associated with inter-annual and longer time scales. Relying on ensemble means to limit model spread and uncertainties remains a necessity in using models to project future climate.

© Copyright by Andrea M. Allan  
August 16, 2012  
All Rights Reserved

Analyzing the Present and Future Pacific-North American Teleconnection  
using Global and Regional Climate Models

by  
Andrea M. Allan

A DISSERTATION

submitted to

Oregon State University

in partial fulfillment of  
the requirements for the  
degree of

Doctor of Philosophy

Presented August 16, 2012  
Commencement June 2013

Doctor of Philosophy dissertation of Andrea M. Allan presented on August 16, 2012.

APPROVED:

---

Major Professor, representing Geography

---

Dean of the College of Earth, Ocean, and Atmospheric Sciences

---

Dean of the Graduate School

I understand that my dissertation will become part of the permanent collection of Oregon State University libraries. My signature below authorizes release of my dissertation to any reader upon request.

---

Andrea M. Allan, Author

## ACKNOWLEDGEMENTS

I would like to extend my deepest gratitude to my major advisor, Steve Hostetler. An advisor can make or break your graduate career, and Steve made mine possible. From the first day I walked into Steve's office, he believed in me, encouraged me, and allowed me to evolve as both a student and an academic professional. Graduate school is not just about classes, research, and theses. It's about defining yourself as a person, and challenging yourself to take risks and jump over hurdles you once thought were too high. The journey through my PhD was a roller-coaster at times, and somehow Steve was able to stick with me through all the ups, downs, and loop-de-loops. He always knew when to push me toward a goal or when to just let me work independently. He was available when a problem arose, and provided necessary guidance for my research while allowing me to come up with all the important questions and answers. During the depths of writing my dissertation, Steve spent countless hours editing my chapters and providing invaluable feedback, inevitably making me a better writer. He taught me that in graduate school there is no point in asking easy questions, and after your preliminary oral exam you're supposed to feel like a complete idiot! Because of Steve's mentorship I've discovered my place in academia, redefined my passion for science, and gained a wonderful colleague and friend.

I want to thank my committee, Nick Pisias, Julia Jones, and Eric Skyllingstad for continuously supporting me throughout the completion of my PhD. I thank Nick for helping me sort out my research directions and for constantly stopping in my office

to ask the daunting question, “Did you finish your paper yet?” I thank Julia for reinforcing the “geography” aspect of my dissertation, and I thank Eric for keeping me sharp on my meteorology and atmospheric science skills.

I am grateful for the support of my various officemates and classmates throughout the years for keeping me entertained, distracting me when appropriate (and when not appropriate), and for commiserating with me on the life of a grad student. I want to extend a special thanks to Jay Alder for his eagerness and willingness to help me debug many IDL codes, fix computer problems, and share special IDL routines he wrote because the ones included in the software weren’t good enough.

I would not be the person I am today without the unconditional love and endless support I receive from my parents. From help with grade school science projects to a college education, my parents taught me the values of working hard and doing what you love, and for this I am forever grateful. I am also lucky to have the best brother a sister could ask for, and I thank him for being a friend, fantastic babysitter, and for providing endless comic relief.

Finally, I thank my husband, Robert, for everything. I thank him for his love and support, for keeping my head out of the clouds and my feet firmly on the ground, and for allowing me to be me. He is amazingly patient and understanding, and learned about my research so he could listen to and discuss my thoughts and ideas. He is my inspiration and motivation, and I would not be Dr. Dre without him.

## CONTRIBUTION OF AUTHORS

Steve Hostetler provided guidance, advice, and largely contributed to the completion of each chapter in this dissertation by providing thorough and timely edits. Steve Hostetler and Jay Alder provided a great deal of assistance with the RegCM3 model runs, including pre- and post-processing of the model output, as well as input on the interpretation and analysis of the data for Chapter 1.

## TABLE OF CONTENTS

	<u>Page</u>
Chapter 1. Introduction.....	1
1.1 Motivation.....	1
1.2 Physical background.....	3
1.3 Thesis overview.....	15
1.4 References.....	15
Chapter 2. Analyzing the present and future Pacific-North American teleconnection and its relationship to climate using the ECHAM5 global and RegCM3 regional climate models.....	18
2.1 Abstract.....	19
2.2 Introduction.....	20
2.3 Model simulations and calculation methods.....	23
2.3.1 Global and regional models.....	23
2.3.2 Teleconnection index calculation methods.....	26
2.3.3 Teleconnection pattern calculation methods.....	29
2.4 Temporal variability.....	31
2.5 Spatial variability.....	36
2.6 Relationship to present climate.....	42
2.6.1 Correlation analysis.....	42
2.6.2 Extremes.....	49
2.7 Relationship to future climate.....	56
2.7.1 Correlation analysis.....	56
2.7.2 Extremes.....	60
2.8 Conclusions.....	66

## TABLE OF CONTENTS (continued)

	<u>Page</u>
2.9 Acknowledgements.....	67
2.10 References.....	68
Chapter 3. Analyzing the Pacific-North American teleconnection and its relationship to climate in the CMIP5 models, Part I: Historical simulation.....	71
3.1 Abstract.....	72
3.2 Introduction.....	73
3.3 Model data and calculation methods.....	75
3.3.1 AOGCMs and ESMs.....	75
3.3.2 Teleconnection index and pattern calculations.....	76
3.4 Results and discussion.....	80
3.4.1 Temporal variability.....	80
3.4.2 Spatial variability.....	85
3.4.3 Model performance.....	97
3.4.4 Relationship to surface climate.....	102
3.5 Conclusions.....	117
3.6 Acknowledgements.....	119
3.7 References.....	119
Chapter 4. Analyzing the Pacific-North American teleconnection and its relationship to climate in the CMIP5 models, Part II: Future simulation.....	124
4.1 Abstract.....	125
4.2 Introduction.....	126
4.3 Model data and methods.....	128
4.3.1 AOGCMs and ESMs.....	128

## TABLE OF CONTENTS (continued)

	<u>Page</u>
4.3.2 Teleconnection index and pattern calculation methods.....	130
4.3.3 Surface climate analysis methods.....	131
4.4 Results and discussion.....	132
4.4.1 Temporal variability.....	132
4.4.2 Spatial variability.....	140
4.5 Model performance.....	152
4.6 Relationship to surface climate.....	162
4.6.1 Correlation analysis.....	162
4.6.2 Extreme events.....	167
4.7 Conclusions.....	178
4.8 Acknowledgements.....	181
4.9 References.....	181
Chapter 5. Conclusions.....	187

## LIST OF FIGURES

<u>Figure</u>		<u>Page</u>
1.1	The Pacific-North American teleconnection pattern.....	2
1.2	The global energy balance.....	5
1.3	The balance between the global annual mean net shortwave and net longwave radiation at the top of the atmosphere for all latitudes.....	6
1.4	General global circulation patterns as defined by the Hadley, Ferrel, and Polar cells.....	8
1.5	General global wind patterns associated with the surface flow from the Hadley, Ferrel, and Polar circulation cells.....	8
1.6	The influence of El Nino and La Nina events on the location and strength of the polar and Pacific jet streams.....	14
2.1	The 1950-2000 PNA index for all months.....	32
2.2	The 1950-2000 PNA index for the DJF winter season.....	33
2.3	As in Fig. 2.2, for the 2050-2100 PNA indices.....	33
2.4	Smoothed power spectra for monthly PNA index time series.....	37
2.5	The January Pacific-North American patterns as shown by rotated EOFs.....	38
2.6	500-hPa surface contours.....	40
2.7	Correlations between the PNA index and surface field anomalies for the 1982-2000 regional NCEP Reanalysis model run.....	43
2.8	As in Fig. 2.7, for the regional ECHAM5 simulation for the years 1950-2000.....	44
2.9	Composite anomaly maps for the top 66% of PNA indices for NCEP years 1982-2000 (left column of figure) and the top 33% of ECHAM5 years 1950-2000 (right column of figure).....	50

## LIST OF FIGURES (continued)

<u>Figure</u>	<u>Page</u>
2.10 Composite anomaly maps for the bottom 66% of PNA indices for NCEP years 1982-2000 (left column of figure) and the bottom 33% of ECHAM5 years 1950-2000 (right column of figure).....	51
2.11 Correlations between the PNA index and surface field anomalies for the regional ECHAM5 years 2050-2100.....	57
2.12 As in Fig. 2.12, for the difference between the regional ECHAM5 years 2050-2100 and 1950-2000.....	58
2.13 Composite anomaly maps for the top 33% of PNA indices (PNA+) for present (left column of figure) and future (right column of figure) ECHAM5 years.....	61
2.14 As in Fig. 2.13, for the bottom 33% of PNA indices (PNA-).....	62
2.15 Differenced composite anomaly maps for the top 33% (PNA+; left column of figure) and bottom 33% (PNA-; right column of figure) of PNA indices for ECHAM5 for 2050-2100 minus 1950-2000.....	64
2.16 a) 500-hPa geopotential heights and b) 2-m temperature averaged over the ECHAM5-RegCM3 domain for the years 2050-2100.....	65
3.1 Pacific-North American time series for January 1950-2000, calculated using the RPCA method.....	81
3.2 The 12-month smoothed power spectra for all models using the unsmoothed monthly PNA index time series for the years 1950-2000.....	84
3.3 a) The 12-month smoothed power spectra for 1950-2000, as in Fig. 2, and b) the cross-correlation analysis for the four CMIP5 models with zero-lag cross-correlation coefficients $>0.7$ .....	86
3.4 The January Pacific-North American pattern as shown by the second leading mode of a rotated-EOF analysis on monthly standardized 500-hPa geopotential height anomalies.....	88
3.5 The loading patterns associated with the PNA for NCEP and all CMIP5 models for the years 1950-2000.....	89

## LIST OF FIGURES (continued)

<u>Figure</u>	<u>Page</u>
3.6 The spatial distribution of each center P1, P2, and P3 for each model.....	92
3.7 The PNA teleconnection loading pattern as defined by projecting the time series of the PNA index for each model back onto the 500-hPa geopotential height anomaly field used to calculate the index for all Januaries from 1950-2000.....	94
3.8 Composite spaghetti plots of three different isohyps – 5280 m, 5460 m, and 5640 m – on the 500-hPa pressure surface during both positive (indices greater than 0.5) and negative (indices less than -0.5) PNA years.....	98
3.9 500-hPa isohyps for positive (greater than 0.5; red lines) and negative (less than -0.5; blue lines) PNA indices.....	99
3.10 The temporal correlation between the 2-m surface temperature anomalies and the PNA index for the month of January relative to the DJF winter season for the years 1950-2000.....	104
3.11 As in Fig. 3.10, for the precipitation rate.....	105
3.12 Composite maps for the temperature anomalies for the top 33% of positive PNA years for the Historical simulation.....	110
3.13 As in Fig. 3.12, for the bottom 33% of negative PNA index years.....	111
3.14 Composite maps for the precipitation anomalies for the top 33% of positive PNA years for the Historical simulation.....	113
3.15 As in Fig. 3.14, for the bottom 33% of negative PNA index years.....	114
4.1 Pacific-North American time series for January 2006-2050, calculated using the RPCA method with respect to the 2006-2050 base period.....	133
4.2 Relative frequency distribution of the PNA index time series.....	138
4.3 The 12-month smoothed power spectra.....	141
4.4 The loading patterns associated with the PNA for each CMIP5 model for RCP85 years 2050-2100.....	143

## LIST OF FIGURES (continued)

<u>Figure</u>	<u>Page</u>
4.5 The spatial distribution of each center P1, P2, and P3 for each model.....	149
4.6 The mapped spatial distribution of each center P1, P2, and P3 .....	150
4.7 The PNA teleconnection loading pattern as defined by the projection of the PNA index time series for each model onto the 500-hPa geopotential height anomaly field used to calculate the index for all Januaries from 1950-2000.....	153
4.8 500-hPa isohypsес for positive (greater than 0.5; red lines) and negative (less than -0.5; blue lines) PNA indices for 2050-2100.....	159
4.9 The temporal correlation between the 2-m surface temperature anomalies and the PNA index for the month of January relative to the DJF winter season for RCP85.....	164
4.10 As in Fig. 4.9, for the precipitation rate anomalies.....	166
4.11 2-m temperature averaged over the PNA sector for the years 2006-2100.....	169
4.12 Composite maps for the temperature anomalies during the top 33% of positive PNA years for RCP85.....	170
4.13 As in Fig. 4.12, for the bottom 33% of negative PNA years.....	171
4.14 Composite maps for the precipitation anomalies during the top 33% of positive PNA years for RCP85.....	174
4.15 As in Fig. 3.13, for the bottom 33% of negative PNA years.....	175

## LIST OF TABLES

<u>Table</u>	<u>Page</u>
2.1 Results from the rotated EOFs shown in Fig. 2.5.....	39
3.1 List of descriptive characteristics for the CMIP5 climate models used in the study.....	77
3.2 The mean, standard deviation, and positive-to-negative index area ratio for NCEP and each CMIP5 model.....	82
3.3 The rotated-EOF mode and explained variance associated with the PNA teleconnection pattern for each model.....	90
3.4 The longitudinal ( $\Delta\text{lon}$ ) and latitudinal ( $\Delta\text{lat}$ ) distance from NCEP for P1, P2, and P3 in degrees for each CMIP5 model.....	93
3.5 The P1, P2, and P3 center anomaly differences, in meters, between the CMIP5 models and NCEP for the Historical time period.....	95
3.6 The see-saw index (SSI), difference factor (DF), and ranking value (SSI+DF) for each model.....	101
4.1 The mean, standard deviation, and positive-to-negative index area ratio for both future time periods.....	134
4.2 The p-values from a Student's t-test to verify if the means of the PNA index time series are significantly different from each other.....	136
4.3 Skewness of the NCEP and CMIP5 DJF PNA index time series distributions for the Historical and RCP85 time periods.....	139
4.4 The rotated-EOF mode and explained variance associated with the PNA teleconnection pattern for each model for the RCP8.5 future simulation.....	144
4.5 The longitudinal ( $\Delta\text{lon}$ ) and latitudinal ( $\Delta\text{lat}$ ) shift in location of P1, P2, and P3 in degrees for each CMIP5 model between the Historical and RCP85 time periods.....	146
4.6 As in Table 4.5, for the difference between NCEP and RCP85.....	147
4.7 The P1, P2, and P3 center anomaly differences, in meters, between the Historical and RCP85 time periods.....	154

## LIST OF TABLES (continued)

<u>Table</u>		<u>Page</u>
4.8	As in Table 4.7, for the difference between NCEP and RCP85.....	155
4.9	The see-saw index (SSI) for the Historical and RCP85 time periods.....	157
4.10	The difference factor (DF) for the Historical and RCP85 time periods.....	160
4.11	The overall model ranking, with respect to NCEP, for the Historical and RCP85 time periods.....	161

For Robert

# Analyzing the Present and Future Pacific-North American Teleconnection using Global and Regional Climate Models

## Chapter 1: Introduction

### 1.1 Motivation

The Pacific-North American (PNA) teleconnection pattern has long been recognized as a robust feature of Northern Hemisphere atmospheric circulation and more specifically represents the structure of the quasi-stationary wave field over the North Pacific and North America. In its nominal state, the PNA pattern features an upper level ridge over western North America followed by a trough east of the Rockies; the PNA index simply measures the amplification (positive index) or dampening (negative index) of this wave (Fig. 1.1). Numerous studies exist that analyze the PNA in both observations and model simulations; however, few of these assess its influence over North American climate, and those that have were limited both temporally and spatially (e.g., Coleman and Rogers (2002); Lau, 1981; Notaro et al., 2006).

The PNA is the most dominant control over intra- and interannual climate variability in North America. Correlations with winter surface air temperatures and precipitation in North America and the patterns associated with these spatial correlations are robust and consistent throughout observations (Wallace and Gutzler, 1981; Leathers *et al.*, 1991). Future climate change projections indicate up to 8°C of

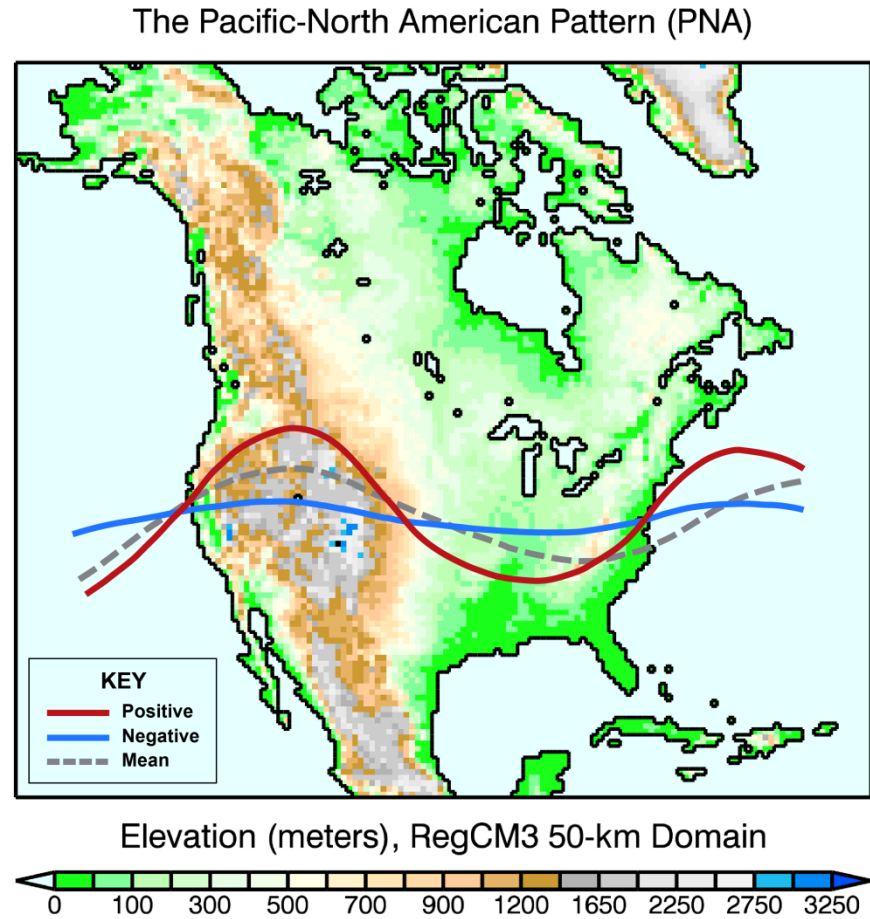


**Figure 1.1** The Pacific-North American teleconnection positive (red line), negative (blue line), and mean state (gray line) flow patterns. The map shows the elevation and 50-km domain used in the RegCM3 simulations. *Figure adapted from Leathers et al., 1991.*

warming on average across the globe, with even larger increases in higher latitudes, due to increases in atmospheric greenhouse gas concentrations (IPCC, 2007). Global climate changes of this magnitude will undoubtedly trigger changes in large-scale atmospheric dynamics. Understanding the role of the PNA in the present climate allows us to better understand how the PNA might change in future climates scenarios.

## 1.2 Physical background

The energy balance on Earth is the primary driver for most physical processes in the Earth's climate system. Energy is broken into radiative (longwave and shortwave) and non-radiative (sensible and latent heat) fluxes at the Earth's surface, and at any level in the atmosphere the energy budget is simply a balance among these components (Fig. 1.2). An object can interact with radiation in three ways: absorption, reflection, and emission. Net radiation quantifies the amount of energy remaining after these interactions and ultimately determines temperature. In turn, the temperature of an object generally determines the amount of radiation emitted by that object. Albedo defines the portion of incoming shortwave radiation ("insolation") that is directly reflected back to space. Surfaces with high albedos, such as snow and ice, have a higher reflectivity than surfaces with low albedos, such as black dust. Consequently, given the same amount of incoming energy, clean ice will reflect more radiation than ice covered with black dust, allowing the dusty surface to absorb more radiation than the clean ice. Objects can absorb both shortwave and longwave radiation; however, emission occurs primarily as thermal infrared longwave radiation,

as the kind of radiation emitted by an object depends on temperature, and the temperatures on Earth generally range only in the infrared part of the spectrum. Low-latitudes not only receive more insolation due to the Earth-Sun geometry, but the combined albedo of the oceans and land is much lower than the snow- and ice-covered poles. The net radiation at the top of the atmosphere, calculated as incoming shortwave minus outgoing longwave radiation, varies by latitude and leads to an energy surplus at the equator and an energy deficit at the poles (Fig. 1.3). To balance the equator-to-pole distribution of energy, heat is transferred from the equator toward the poles through both oceanic and atmospheric heat transport. If the Earth's surface was homogeneous, this equator-to-pole, or "meridional", heat transport would be uniform across the entire globe; however, the Earth is a heterogeneous mixture of water and land surfaces, which interrupts the otherwise direct transport of energy by both the atmosphere and the ocean.

The atmosphere displays three, semi-permanent large meridional circulation features called the Hadley, Ferrel, and Polar cells (Fig. 1.4). The Hadley cell is located between the equator and subtropics and is initiated by intense surface heating at the equator. As the moist, tropical equatorial air just above the surface warms enough to become unstable, it rises due to convection and creates the Intertropical Convergence Zone (ITCZ). The ITCZ is characterized by towering cumulonimbus clouds whose vertical growth is limited only by the temperature inversion that defines the boundary between the troposphere and the stratosphere, known as the tropopause.

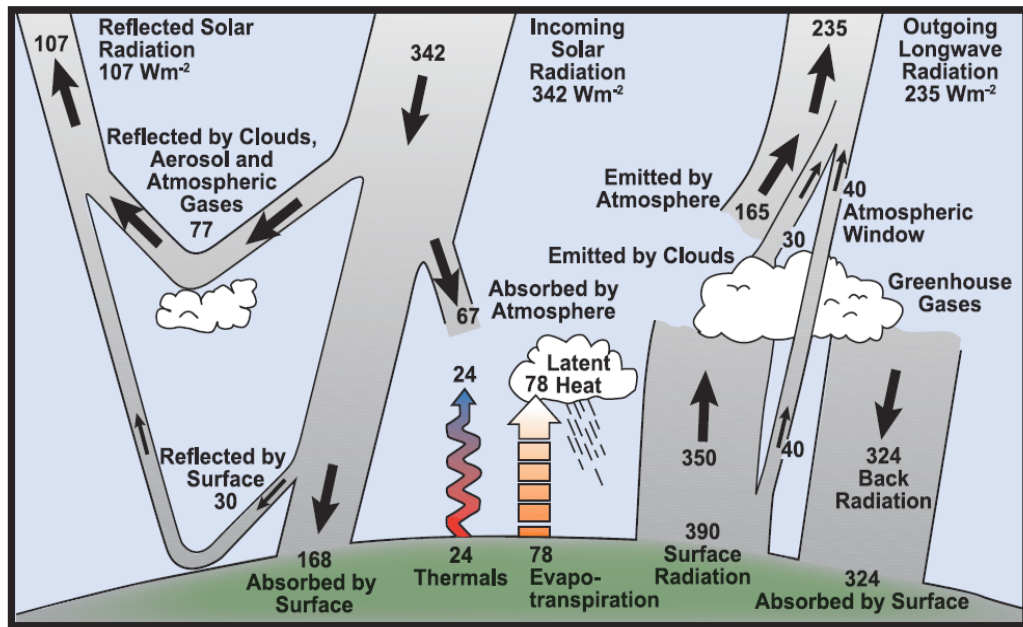


**Figure 1.2** The global energy balance. Units are in  $\text{W m}^{-2}$  and relative to the global mean incoming solar radiation of  $342 \text{ W m}^{-2}$ . *Figure from IPCC (2007).*

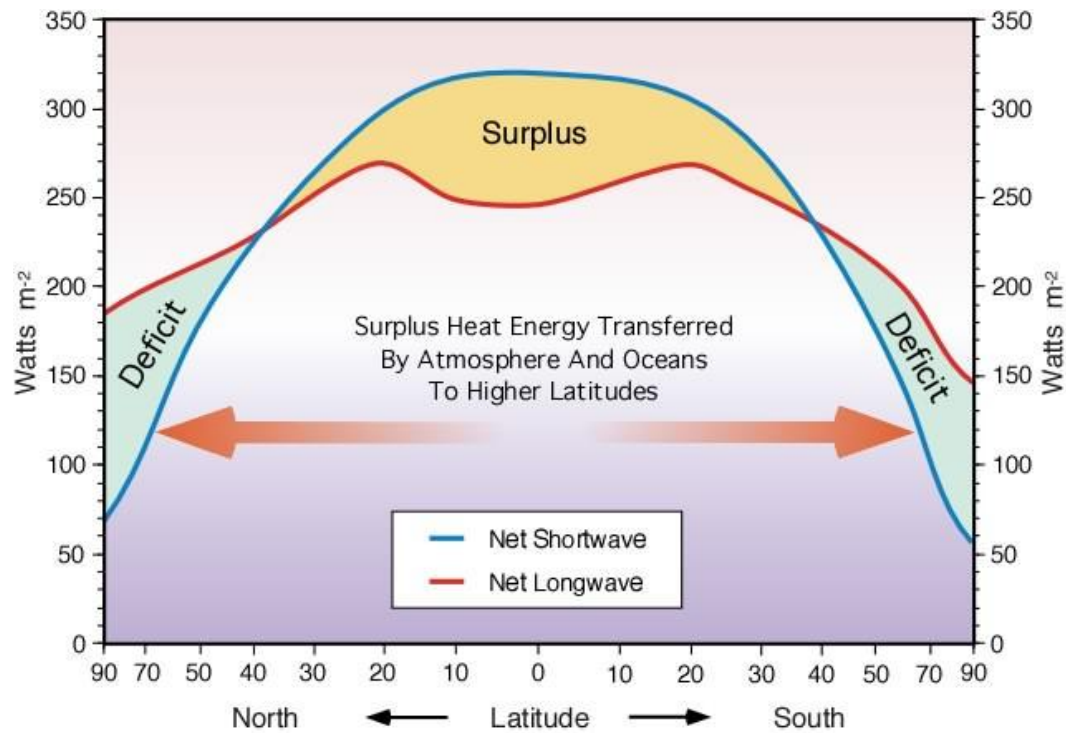


**Figure 1.3** The balance between the global annual mean net shortwave and net longwave radiation at the top of the atmosphere for all latitudes. *Figure from Pidwirny (2006).*

At this boundary ascending air is forced to the north and south and, as the air flows poleward in the upper atmosphere, it cools and loses moisture through precipitation and evaporation processes. Eventually, the air cools enough to become denser than the surrounding air and it subsides toward the surface in the subtropics around 30°N/S latitude. Subsiding air expands and warms, further evaporating any remaining moisture, and this process is responsible for the presence of the semi-permanent subtropical highs and the Earth's largest deserts, such as the Sahara Desert in Northern Africa. As the sinking air reaches the surface it is once again forced to diverge north and south, which, in the Northern Hemisphere, completes the Hadley cell to the south and begins the Ferrel cell to the north. Combined with the Coriolis force associated with the rotation of the Earth, the southward flow of air at the surface in the Hadley cell creates the trade winds, while the northward flow of air in the Ferrel cell creates the mid-latitude westerlies (Fig 1.5). The trade winds from both hemispheres converge at the surface near the equator, contributing to the ascending air associated with the ITCZ. In the Northern Hemisphere, the Ferrel cell interacts to the north with the Polar cell. Cold, dense air at the poles sinks to create the Polar high, and as this air flows outward at the surface it converges with the relatively warm and moist air that is carried northward by the westerlies. The convergence of these two air masses causes the air to rise, forming the boundaries of the Ferrel and Polar cells around 60°N latitude. Similar to the ITCZ, as this rising air reaches the tropopause it is forced to the north and south and thus completes the circulation for each of these cells.

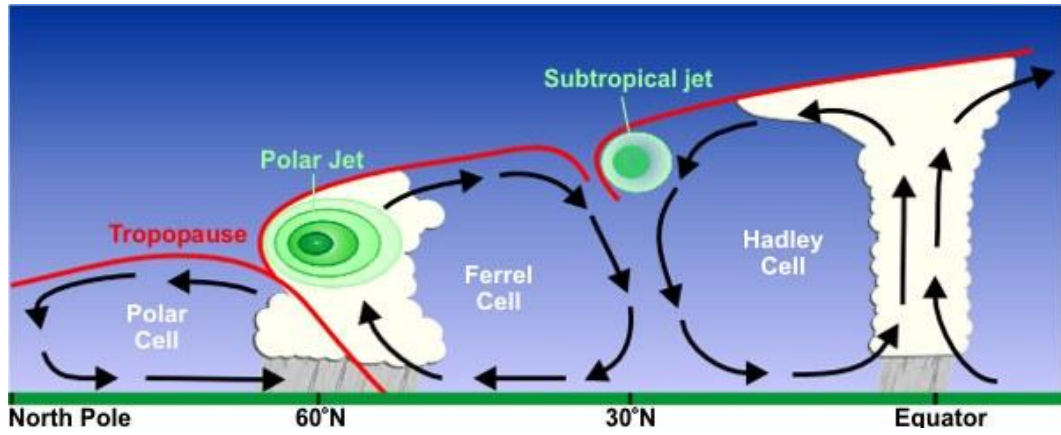


**Figure 1.4** General global circulation patterns as defined by the Hadley, Ferrel, and Polar cells. *Figure from NOAA (2008).*

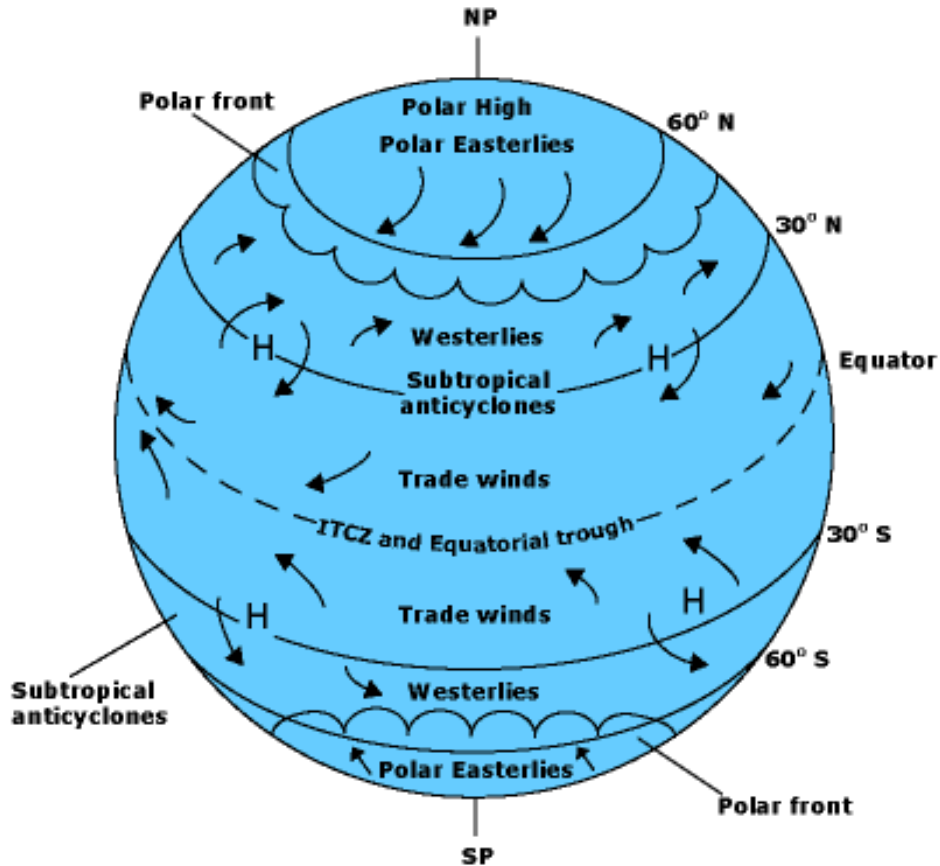


**Figure 1.5** General global wind patterns associated with the surface flow from the Hadley, Ferrel, and Polar circulation cells. *Figure from the National Snow and Ice Data Center.*

Large temperature gradients, or “fronts”, define the boundaries between each of the three cells where relatively cold, dry air from the north meets warm, moist air from the south. Zonal wind jets, or fast-flowing currents of air, form along these frontal boundaries due to the thermal wind relation. The strongest frontal boundary is that between the Ferrel and Polar cells and is marked by the presence of the polar jet, which is often referred to simply as the mid-latitude jet stream. In the upper atmosphere, away from the influences of surface friction, air parcels are acted upon only by gravity, the pressure gradient force, and the Coriolis force. These forces tend to be in both hydrostatic and geostrophic balance. Hydrostatic balance refers to the balance between the pressure gradient force and the force of gravity in the vertical direction, while geostrophic balance refers to the balance of the pressure gradient force and the Coriolis force in the horizontal direction. Winds in the upper atmosphere are referred to as “geostrophic” because the movement of air is governed solely by changing pressure gradient and Coriolis forces.

Along the polar front, the convergence of the opposing air masses affects the height of the tropopause. Because cold air is more dense than warm air, the “geopotential height” of an atmospheric pressure level is lower over a cold air mass than over warm air. The height of the tropopause is therefore much lower on the colder, northern side of the polar front (~7-8 km or 400 mb) than it is on the warmer, southern side (~10-11 km or 250 mb) (Palmén and Newton, 1969). Consequently, the strength of the horizontal temperature gradient, and thus the geostrophic wind, increases with height across the polar front between 400 mb and 250 mb. This creates

a vertical shear in the geostrophic wind and subsequent vertical rotation of air in the upper troposphere. The influence of the Coriolis force in the Northern Hemisphere causes an air parcel to move eastward in an effort to keep the horizontal and vertical forces in balance, thus creating a jet stream (Carlson, 1998; Holton, 2004).

The north-south boundaries between the Northern Hemisphere continents and oceans cause undulations in the mid-latitude jet stream thereby preventing the flow from remaining purely zonal around the globe. Differential heating between land and ocean surfaces causes seasonal high and low pressure centers to form; these differences are largest during the winter months when the oceans are generally warmer than land due to the large heat capacity of water. In general, at mid- and high-latitudes low pressure forms over the oceans, while high pressure forms over land. In the Western hemisphere, the Aleutian low over the North Pacific Ocean allows for the intrusion of cold, dry air from the north, while the continental high over North America “blocks” these cold air intrusions and instead induces the flow of warm, moist air from the south. As a result, “troughs” form in the mid-latitude jet stream where cold air descents from the north and “ridges” form where warm air ascends from the south, a process known as “baroclinic instability”. These troughs and ridges, or “Rossby waves”, are the source of the storm tracks that form along the path of the mid-latitude jet stream throughout the winter months.

Interannual variability in equatorial Pacific sea surface temperatures (SSTs) influences the location and strength of the mid-latitude jet stream. Normal or neutral conditions in the equatorial Pacific are characterized by a large east-to-west SST

gradient. Ocean upwelling in the eastern margins and along the west coast of South America brings cold, nutrient-rich waters to the surface, while warm surface waters “pool” in the western part of the basin (Hartmann, 1994). The location of the warm pool defines the Pacific Walker cell, an east-west atmospheric circulation similar to the Hadley cell that is characterized by rising air and deep convection over the western warm pool, and sinking, dry air over the cool ocean waters and South America in the east. The easterly trade winds in equatorial Pacific region apply stress to the surface waters, pushing warm water and air toward the west, which reinforces the east-west temperature gradient. These conditions create a region of low surface pressure in the west and high surface pressure in the east. The Southern Oscillation describes fluctuations in this east-west surface pressure gradient across the equatorial Pacific and is quantified by the Southern Oscillation Index (SOI). A negative (positive) SOI corresponds to anomalously high (low) pressure in the west and anomalously low (high) pressure in the east. Consequently, a positive SOI increases the pressure gradient across the Pacific, while a negative SOI decreases the pressure gradient.

The El Niño-Southern Oscillation (ENSO) describes how the Southern Oscillation affects both oceanic and atmospheric conditions within the equatorial Pacific. A negative SOI leads to a weakening of the trade winds and allows the western warm pool to extend eastward, often across the entire Pacific basin to the coast of South America, creating anomalously warm SSTs throughout the equatorial Pacific. These conditions are referred to as the El Niño or warm phase of ENSO. The eastward shift of the warm pool displaces the rising branch of the Walker circulation

to the east, repositioning wet conditions more centrally over the equatorial Pacific.

The La Niña or cold phase is associated with positive SOIs and refers to anomalously cold SSTs. A positive SOI describes a stronger-than-normal east-west pressure gradient across the equatorial Pacific and leads to stronger trade winds, increased upwelling along the eastern Pacific margin, and the “piling up” of warm waters in the western part of the Pacific basin. The Walker circulation shifts westward and as a result, La Niña events bring monsoon-like conditions to Indonesia and the western Pacific, while the rest of the equatorial Pacific remains cool and dry due to colder-than-normal SSTs (Hartmann, 1994; CPC, 2005).

The oscillation between El Niño and La Niña in the equatorial Pacific causes contrasting climate conditions across the globe, thereby defining ENSO as a teleconnection. The occurrence of a warm or cold ENSO event affects SSTs and circulation patterns throughout the Pacific basin and therefore influences the upper-atmosphere jet streams, which in turn affects the climate in North America (Fig. 1.6). During the winter months, warmer-than-normal SSTs associated with an El Niño event can enhance the low pressure positioned over the North Pacific, which amplifies the mid-latitude jet stream and brings warm, wet conditions to much of western North America. On the other hand, a La Niña event can weaken the Aleutian low and create a relative high pressure center over the North Pacific due to the presence of anomalously cold SSTs, effectively shifting the jet stream poleward. The positioning of the mid-latitude jet is directly related to the Pacific-North American teleconnection pattern (PNA). The PNA is defined by the juxtaposition of the Aleutian low and

continental high over Western North America at the 500-hPa level, and also includes the subtropical high over Hawaii and a low pressure over the southeastern United States. Anomalies associated with these pressure centers dictate the shape of the mid-latitude jet stream and determine positive and negative phases of the PNA. Studies show a correlation between ENSO and the PNA, particularly El Niño events and positive PNA phases; however, the PNA is driven by internal variability in the climate system associated with the baroclinic instability in the mid-latitudes (Strauss and Shukla, 2002; CPC, 2012). As a result, the PNA persists as the dominant influence of climate in North America.

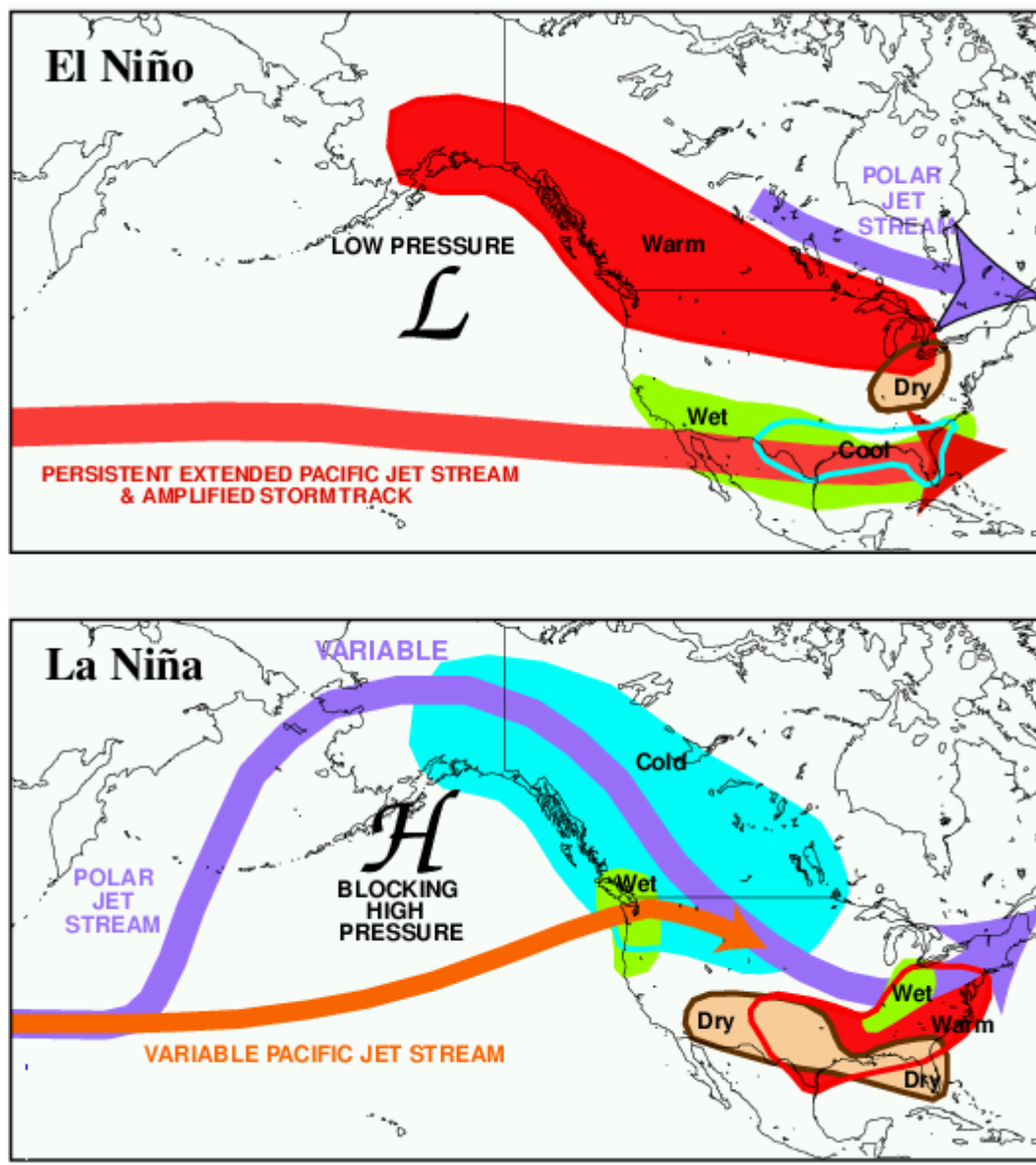


**Figure 1.6** The influence of El Niño and La Niña events on the location and strength of the polar and Pacific jet streams. *Figure from the Climate Prediction Center (2005).*

### 1.3 Thesis overview

This thesis focuses on the presence and robustness of the PNA in both global and regional climate models. We use the global circulation model (GCM) MPI/ECHAM5 and the high-resolution regional climate model (RCM) RegCM3 to assess the ability of the models to reproduce the PNA, to evaluate the influence of the PNA on surface climate in North America, and explore the relationship between the PNA patterns in both a GCM and nested RCM (Chapter 2). The release of model output from the fifth phase of the Coupled Model Intercomparison Project (CMIP5) in February 2011 allowed for the assessment of the PNA in 27 atmosphere-ocean GCMs (AOGCMs) and earth system models (ESMs). Model output is available under a number of past, present, and future climate scenarios; we chose to analyze the Historical (Chapter 3) and RCP8.5 (Chapter 4) simulations, as these best represent the current state of the climate (Le Quéré et al., 2009; Ganguly et al., 2009). The comprehensive analyses presented in this thesis provide a qualitative and quantitative assessment of the PNA using the most state-of-the-art climate models available today.

### 1.4 References

- Carlson, T.N. (1998): *Mid-Latitude Weather Systems*. American Meteorological Society, 507 pp.
- Coleman, J. S. M. and J. C. Rogers (2003): Ohio River Valley winter moisture conditions associated with the Pacific-North American teleconnection pattern. *J. Climate*. **16**, 969-981.
- Ganguly, A.R., K. Steinhaeuser, D.J. Erikson III, M. Branstetter, E.S. Parish, N. Singh, J.B. Drake, and L. Buja (2009): Higher trends but larger uncertainty and

- geographic variability in 21st century temperature and heat waves. *PNAS*, **106**(37), 15555-15559.
- Hartmann, D.L. (1994): *Global Physical Climatology*. Academic Press, San Diego, 411 pp.
- Holton, J.R. (2004): *An Introduction to Dynamic Meteorology*, 4<sup>th</sup> Ed. Academic Press, San Diego, 535 pp.
- IPCC (2007): Climate Change 2007: The Physical Science Basis. Contribution of Working Group I to the Fourth Assessment Report of the Intergovernmental Panel on Climate Change [Solomon, S., D. Qin, M. Manning, Z. Chen, M. Marquis, K.B. Averyt, M.Tignor and H.L. Miller (eds.)]. Cambridge University Press, Cambridge, United Kingdom and New York, NY, USA.
- Lau, N.-C. (1981): A diagnostic study of recurrent meteorological anomalies appearing in a 15-year simulation with a GFDL general circulation model. *Mon. Wea. Rev.*, **109**, 2287-2311.
- Le Quéré, C., M.R. Raupach, J.G. Canadell, G. Marland, L. Bopp, P. Ciais, T.J. Conway, S.C. Doney, R.A. Feely, P. Foster, P. Friedlingstein, K. Gurney, R.A. Houghton, J.I. House, C. Huntingford, P.E. Levy, M.R. Lomas, J. Majkut, N. Metzl, J.P. Ometto, G.P. Peters, I.C. Prentice, J.T. Randerson, S.W. Running, J.L. Sarmiento, U. Schuster, S. Sitch, T. Takahashi, N. Viovy, G.R. van der Werf, and F.I. Woodward (2009): Trends in the sources and sinks of carbon dioxide. *Nat. Geo.*, **2**, 831-836.
- Leathers, D.J., B. Yarnal, M.A. Palecki (1991): The Pacific/North American teleconnection pattern and United States climate. Part I: Regional temperature and precipitation associations. *J. Climate*, **4**, 517-528.
- Notaro, M., W-C. Wang, and W. Gong (2006): Model and observational analysis of the Northeast U.S. regional climate and its relationship to the PNA and NAO patterns during early winter. *Mon. Wea. Rev.*, **134**, 3479-3505.
- Palmén, E. and C.W. Newton (1969): *Atmospheric Circulation Systems*. Academic Press, New York.
- Pidwirny, M. (2006): "Global Heat Balance: Introduction to Heat Fluxes". *Fundamentals of Physical Geography, 2nd Edition*. Online 19 September 2012: <http://www.physicalgeography.net/fundamentals/7j.html>.

Straus, D.M. and J. Shukla (2002): Does ENSO force the PNA? *J. Climate*, **15**, 2340-2358.

Wallace, J.M. and D.S. Gutzler (1981): Teleconnections in the geopotential height field during the Northern Hemisphere winter. *Mon. Wea. Rev.*, **109**, 784-812.

Chapter 2: Analyzing the present and future Pacific-North American  
teleconnection and its relationship to climate using the ECHAM5 global  
and RegCM3 regional climate models

Andrea M. Allan<sup>1</sup>, Steven W. Hostetler<sup>2</sup>, and Jay R. Alder<sup>2</sup>

<sup>1</sup>College of Earth, Ocean, and Atmospheric Sciences, Oregon State University,  
Corvallis, Oregon, 97331

<sup>2</sup>U.S. Geological Survey, Oregon State University, Corvallis, Oregon, 97331

## 2.1 Abstract

The Pacific-North American (PNA) teleconnection pattern is a quasi-stationary wave field over the North Pacific and North America that has long been recognized as a robust feature of Northern Hemisphere atmospheric circulation, and directly affects the interannual variability of North American temperature and precipitation. Here we use the general circulation model (GCM), MPI/ECHAM5 (T63 resolution), and the high-resolution regional climate model, RegCM3 (RCM; 50-km grid spacing), to assess the ability of the models to reproduce the PNA, to evaluate the influence of the PNA on surface climate, and explore the relationship between the PNA patterns in both a GCM and nested RCM. The model output from both the GCM and RCM covers 240 years (1890-2100) representing the present (IPCC 20C) and future (IPCC A2 SRES) climates. We examine the spatial and temporal changes in the PNA pattern and index over the length of the model runs, and investigate future changes in the PNA, climate and surface hydrology in North America.

Strong correlations exist between the PNA monthly index and both surface temperature and precipitation in North America (Leathers *et al.*, 1991). Studies have found a shift of the PNA index toward more positive values in recent years, which has resulted in warmer temperatures in the Western half of the United States, contributing to more of the precipitation falling as rain rather than snow, as well as increased snow melt and an earlier spring onset (Wallace and Gutzler, 1981; Abatzoglou, 2010; Fauria and Johnson, 2008). Changes in the PNA spatial pattern also greatly influence climate in central North America due to the location of the “neutral zone”, a zone where

surface climate variables such as temperature and precipitation experience zero correlation with the PNA pattern, although regions of positive and negative correlations border on either side. This zone can shift during strong positive or negative PNA events, which can mean the difference between an anomalously warm versus an anomalously cold winter season. To illustrate these influences, we produce maps of the correlations between the GCM PNA indices and RCM surface climate variables and compare the results to those from the NCEP/NCAR Reanalysis. We analyze the effect of extreme positive and negative PNA events on surface climate anomalies to gain an understanding of the extent to which the PNA can influence climate. The results from this study will explore the PNA as an important, robust feature in observed atmospheric circulation, which has strong influences over the climate of North America.

## 2.2 Introduction

The Pacific-North American (PNA) teleconnection pattern has long been recognized as a robust feature of Northern Hemisphere atmospheric circulation and more specifically represents the structure of the quasi-stationary wave field over the North Pacific and North America. Numerous studies exist that analyze the PNA in both observations and model simulations; however, few of these assess its influence over North American climate, and those that have were limited both temporally and spatially (e.g., Lau, 1981; Notaro et al., 2006). Yu and Zwiers (2007) examined the response of climate in the PNA sector to ENSO and the PDO using 1,000 years of

modeled output from the Canadian Centre for Climate Modelling and Analysis (CCCma) coupled global climate model and found that all three teleconnections were represented in the GCM and compared well to observations. The study, however, focused on the strength of teleconnections and did not investigate the behavior of the PNA index nor its influence over North American climates. Kawamura et al. (1995) used a low-resolution GCM to simulate low-frequency modes of variability in the northern extratropics. A rotated-EOF analysis revealed the PNA as the leading winter mode in observations and the third leading mode in the simulation. When compared to observations, the modeled PNA exhibited very similar spatial patterns; however, variability at interannual and interdecadal time frames was quite different from observations.

The PNA is the most dominant control over intra- and interannual climate variability in North America. Correlations with winter surface air temperatures and precipitation in North America, and the patterns associated with these spatial correlations, are robust and consistent throughout observations (Wallace and Gutzler, 1981; Leathers *et al.*, 1991). Coleman and Rogers (2002) focused on the relationship between the PNA and precipitation in the Ohio River Valley, and their data support the high negative correlation in this region. They found that the polarity of the PNA directly influences the hydrology of the region and extreme negative PNA winters can cause a 100% increase in river discharge. Rodionov and Aseel (2001) investigated the consistency of the positive and negative PNA patterns based on the value of the index alone and found that the locations of the ridges and troughs were not consistent.

External forcings, such as strong El Niño events and the distribution of Pacific SSTs, played a large role in the shape of the wave field. The authors found that slight changes in the shape of the wave field between one strong positive PNA event to the next can offset the positions of the associated ridges and troughs enough that a specific location can experience anomalously cold temperatures during one event and normal—or even warmer than average temperatures—during another similar event. Thus, climatological averages of the PNA pattern are meant for large-scale assessments, as the influence of individual events at the regional scale can vary substantially.

Because the PNA influences surface temperature so strongly it consequently controls the form of precipitation that falls in a region. Anomalous warm surface temperatures will raise the 0°C isotherm, affecting both the elevation at which precipitation falls as snow and seasonal snowpack in mountainous regions. Studies have found a shift of the PNA index toward more frequent positive modes during the late winter months, particularly after the 1950s (Leathers and Palecki, 1992). This shift has resulted in warmer temperatures in the Western half of the United States, contributing to more of the precipitation falling as rain instead of snow, suggesting an earlier onset of spring snow melt. This warming has led to an overall decline of mountain snowpack in the western United States during the latter half of the 20<sup>th</sup> century (Abatzoglou, 2010). Positive PNA indices also may be related to active wildfire years, particularly in the Southern Canadian Rockies, as warmer temperatures

and less precipitation typically lead to drier conditions during the summer fire season during positive PNA events (Fauria and Johnson, 2008).

The Pacific-North American pattern is quantified using an index value that typically ranges between  $\pm 3$ . Several methods have been developed to calculate the index, beginning with the linear pointwise method by Wallace and Gutzler (1981). Barnston and Livezey (1987) provide the first comprehensive empirical orthogonal function (EOF) analysis of the Northern Hemisphere teleconnections using interpolated and gridded observed geopotential height data.

Here we explore the PNA teleconnection in the global circulation model (GCM) MPI/ECHAM5 as applied to the regional climate model RegCM3. In the next section we describe both climate models and the methods used to calculate the PNA temporal index and spatial pattern. In Sections 2.4 and 2.5 we assess the changes in temporal and spatial variability between the present and future climate simulations, in Sections 2.6 and 2.7 we explore the relationship between the PNA and climate, and in Section 2.8 we conclude with a discussion of the results.

## 2.3 Model simulations and calculation methods

### 2.3.1 Global and regional models

In order to investigate the regional effects of the Pacific-North American pattern on the past and future climates of North America, it is necessary for the PNA to be resolved in both global and regional climate models. There is little research regarding the presence of the PNA pattern in climate models; however, because the

pattern is such a robust feature in the atmosphere and has been shown to greatly influence climate in North America, it is important that climate models also demonstrate the PNA in order to accurately portray atmospheric circulation patterns.

The climate models employed here are the National Centers for Environmental Prediction/Atmospheric Research (NCEP/NCAR) Reanalysis, a quasi-observational GCM used as the observational basis (Kalnay et al., 1996), ECHAM5, the coupled global atmosphere-ocean general circulation model (AOGCM) developed by the Max-Planck Institute for Meteorology, and RegCM3, a 50-km resolution regional climate model developed at the Abdus Salam International Center for Theoretical Physics (ICTP). The atmospheric component of ECHAM5 has a T63 horizontal resolution ( $\sim 1.875^\circ \times 1.875^\circ$ ) and 31 vertical levels and the ocean component has a  $1.5^\circ$  resolution and 40 vertical depth levels (Roeckner et al., 2003; Jungclaus et al., 2005; Marsland et al., 2003). ECHAM5 is part of a group of global AOGCMs that have been applied as part of the Intergovernmental Panel on Climate Change (IPCC) Assessment Report 4 (AR4) to assess global climate changes and their effects on society, including potential adaption and mitigation efforts. The IPCC AR4 introduced six greenhouse gas emissions scenarios as part of the Special Reports on Emissions Scenarios (SRES). These scenarios project global temperature and sea-level rise as a result of varying rates of change of primary greenhouse gases due to both anthropogenic and natural contributions. Based on these scenarios, AOGCMs project global temperatures to rise between  $0.3^\circ\text{C}$  and  $6.4^\circ\text{C}$  by the year 2100. ECHAM5, as part of this ensemble of AOGCMs, provides global model output for

241 years (1860-2100) and is composed of two datasets: the 20<sup>th</sup>-century run (hereafter 20C; years 1860-2000) and the SRES A2 run (hereafter A2; years 2001-2100). The 20C run is designed to represent increases in greenhouse gases as observed throughout the 20<sup>th</sup> century. The A2 emissions scenario describes a heterogeneous world, where “the underlying theme is that of strengthening regional cultural identities, with an emphasis on family values and local traditions, high population growth, and less concern for rapid economic development” (IPCC, 2009). By the end of the 21<sup>st</sup> century, the A2 scenario describes a doubling of the world population and atmospheric carbon dioxide (CO<sub>2</sub>) concentrations exceed 800 ppmv.

RegCM3 is the third generation of a regional climate model that is originally based on the joint National Centers for Atmospheric Research (NCAR)-Pennsylvania State University (PSU) Mesoscale Model version 4 (MM4; Anthes et al., 1987). Since then, several increasingly complex versions have emerged (e.g., Giorgi and Mearns, 1999), leading to the release of RegCM3 in 2006. The atmospheric component of RegCM3 is hydrostatic and compressible and includes the radiative transfer scheme from NCAR’s CCM3 (Kiehl et al., 1996). In addition to a large-scale precipitation scheme, RegCM3 also includes the option for a convective precipitation parameterization (Pal et al., 2000; Grell 1993). RegCM3 features a lake model (Hostetler et al., 1993) and a fully-interactive Biosphere-Atmosphere Transfer Scheme (BATS) is implemented within the model to determine radiation, momentum, heat, and moisture components in the atmosphere, within a canopy, and at the Earth’s surface (Dickinson et al., 1993).

The NCEP Reanalysis and ECHAM5 20C and A2 datasets are used to create lateral and surface boundary conditions to use as input to RegCM3. The regional model runs independently on 6-hour time steps that are then used to create monthly averages on a 50-km grid for NCEP years 1982-2000, and the same 241-year period as the ECHAM5 GCM, 1860-2100. Our RegCM3 domain spans  $\sim 20^{\circ}$ - $175^{\circ}$ W longitude and  $\sim 12^{\circ}$ - $75^{\circ}$ N latitude. Post-processing produces model output on 13 vertical sigma levels and includes a suite of both atmospheric and surface climate variables, such as 500-hPa heights, vertical profiles of wind, temperature and moisture, surface air temperature, precipitation, soil moisture, and snow cover, which we use to assess the influence of the PNA over the past, present, and future climate of North America.

It is necessary to make clear distinctions between the use of the GCM and GCM-forced RegCM3 datasets. When referencing either NCEP or ECHAM5, the use of “global” refers to the GCM and “regional” refers to the GCM-forced RegCM3 simulation. We may also use “NCEP-GCM” or “ECHAM5-GCM”, as well as “NCEP-RegCM3” or “ECHAM5-RegCM3” to refer to the global and regional simulations, respectively.

### 2.3.2 Teleconnection index calculation methods

The PNA index measures the amplification (positive index) or dampening (negative index) of the quasi-geostrophic upper-level wave field over North America. The index is typically calculated from 500-hPa heights using one of two methods: 1) a linear pointwise equation that sums the 500-hPa geopotential height anomalies at four

centers of action (Wallace and Gutzler, 1981), or 2) a rotated principle component analysis (RPCA) that is representative of the entire flow field in the Northern Hemisphere (Barnston and Livezey, 1987). The methods produce comparable index values; however, there are some advantages and disadvantages of each method. The linear pointwise method is the more straightforward approach in that it requires only the 500-hPa heights at four locations in the Pacific-North American region:

$$PNA = \frac{1}{4} [z^*(20^\circ\text{N}, 160^\circ\text{W}) - z^*(45^\circ\text{N}, 165^\circ\text{W}) \\ + z^*(55^\circ\text{N}, 115^\circ\text{W}) - z^*(30^\circ\text{N}, 85^\circ\text{W})] \quad (\text{Eq. 1}),$$

However, because the locations used for the computation are invariant, the method cannot account for the natural variability of the actual location of the height centers, and may consequently present biases in the index value. The need to account for location variability gives rise to the application of a RPCA to utilize 500-hPa height information from the entire Northern Hemisphere flow field (Barnston and Livezey, 1987). While the RPCA can be viewed as a more comprehensive analysis of the PNA, it is also slightly more cumbersome and requires a much larger domain to obtain accurate results. The National Oceanic and Atmospheric Administration (NOAA) Climate Prediction Center (CPC; <http://www.cpc.ncep.noaa.gov/data/teledoc/pna.shtml>) provides time series of the PNA index calculated using both of the linear pointwise and RPCA methods, as well as a “modified” pointwise method that attempts to capture the spatial variability mentioned above without requiring a full RPCA:

$$\text{PNA} = \frac{1}{4} [z^*(15-25^\circ\text{N}, 180-140^\circ\text{W}) - z^*(40-50^\circ\text{N}, 180-140^\circ\text{W}) \\ + z^*(45-60^\circ\text{N}, 125-105^\circ\text{W}) - z^*(25-35^\circ\text{N}, 90-70^\circ\text{W})] \quad (\text{Eq. 2}),$$

where  $z^*$  is the 500-hPa height anomaly. As with the original linear pointwise method, the height anomaly values at each of these points or “centers” represent the locations of the climatological high and low pressure areas that drive the PNA pattern. Due to the limited domain of RegCM3 that does not allow for a RCPA using the entire Northern Hemisphere, we use the modified linear pointwise method to calculate the PNA index that is used in the following climate analyses. The CPC identifies high correlations between the indices produced by each of these methods (correlation coefficients 0.9 and higher; documentation found here: [http://www.cpc.ncep.noaa.gov/products/precip/CWlink/pna/month\\_pna\\_index2.shtml](http://www.cpc.ncep.noaa.gov/products/precip/CWlink/pna/month_pna_index2.shtml)), and thus using one index calculation method over another does not degrade the analysis. Research and observations show that the PNA is most prominent during the winter months (e.g., Wallace and Gutzler, 1981; Leathers *et al.*, 1991); however, we compute both seasonal and monthly PNA indices for the subsequent analyses to quantify changes in both the indices and contemporaneous and season-ahead surface fields.

We break our analysis into two time periods, 1950-2000 (often referred to as “20C” or “present”) and 2050-2100 (often referred to as “A2” or “future”), to evaluate the differences between the present and future simulated climates in ECHAM5. Increasing global temperatures throughout the next century increase atmospheric geopotential heights, creating biases in the 500-hPa standardized anomalies that are used in the index calculations. Thus, to remove the effects of global warming we

standardized the PNA indices using the respective time period, rather than a using constant climatology. As such, the index time series for the present (1950-2000) are standardized using the 1950-2000 climatology, while the time series for the future (2050-2100) are standardized using the 2050-2100 climatology.

### 2.3.3 Teleconnection pattern calculation methods

We present the spatial PNA teleconnection pattern in several ways, including through a rotated empirical orthogonal function (rEOF) analysis that closely follows those methods employed by the CPC. Monthly and seasonal EOFs are calculated using the monthly standardized 500-hPa geopotential height anomalies. For each grid point, the monthly anomaly value is standardized using the three months surrounding the month of interest, such that the January anomalies are differenced from the December through February climatology. As with the index calculation methods, these values are standardized using their respective climatologies. A correlation coefficient is then computed for the time series of 500-hPa standardized height anomalies between each grid cell between 20-90°N, creating a matrix of correlation coefficients that contains the same number of rows and columns as x- and y-dimensions in the data. We perform an EOF analysis on this correlation matrix, retaining the ten leading eigenvectors, then rotating these eigenvectors orthogonally according to the varimax criterion (Kaiser 1958). The varimax rotation technique seeks to maximize the sum of the variances, effectively producing a more defined set

of EOFs. We analyze the resulting rotated EOFs (rEOFs) individually to identify the PNA teleconnection pattern mode for each month.

We focus on three of the four centers of action, omitting the center over Hawaii, as these have the largest influence over climate in North America. Previous studies have shown that analyzing the three remaining centers provides more explanatory power with regard to wave energy propagation over North America, and that including the subtropical center when calculating a pointwise index can actually lead to biases in the index value if variability of the PNA is a result of anomalies in the East Asian jet (Leathers et al., 1991). Additionally, the CPC notes that the shift from positive to negative PNA phases is directly related to the eastward or westward shift of the exit region of the East Asian jet further supporting our choice to exclude the subtropical center. The three centers, hereafter referred to as P1, P2, and P3, will be used to assess the spatial patterns of PNA teleconnection.

Similar to the coupling between ECHAM5-GCM and RegCM3, we use RegCM3 simulations forced by the NCEP/NCAR Reanalysis GCM output for the years 1982-2000 as the quasi-observational climatological basis for all regional analyses presented here. Sea surface temperature data necessary for the completion of the 1950-2000 50-year time period used in the regional ECHAM5 analyses was not available at the time of data acquisition, and thus the temporal extent of the regional NCEP simulations are truncated.

## 2.4 Temporal variability

We first verify that the PNA teleconnection is present and consistent in ECHAM5-GCM and that the pattern is propagated into RegCM3 by calculating time series of the PNA index using output from both model simulations. The modeled indices should be representative of the amplitude and frequency found in observations, although the exact values will differ. Our calculated index for the NCEP-GCM data matches exactly the index values available from the CPC website (found online at: [http://www.cpc.ncep.noaa.gov/products/precip/CWlink/pna/month\\_pna\\_index.shtml](http://www.cpc.ncep.noaa.gov/products/precip/CWlink/pna/month_pna_index.shtml)), thereby verifying that our calculations are accurate. The ECHAM5-GCM index displays comparable amplitude and frequency to the CPC time series, with monthly values ranging from  $\pm 3.5$  in the 20C run between 1950 and 2000 (Fig. 2.1). Due to the more limited extent of the RegCM3 domain, we modified the CPC's linear pointwise equation to include three instead of four centers. The PNA center located at (15-25°N, 180-140°W) is not included in the RegCM3 domain, which reduces Eq. 2 to:

$$\text{PNA} = \frac{1}{3} [-z^*(40-50^\circ\text{N}, 180-140^\circ\text{W}) + z^*(45-60^\circ\text{N}, 125-105^\circ\text{W}) - z^*(25-35^\circ\text{N}, 90-70^\circ\text{W})] \text{ (Eq. 3.)}$$

To evaluate any differences between the 3- and 4-point indices, we calculated time series using both equations for the global and regional ECHAM5 simulations (Figs. 2.2 and 2.3). The 3- and 4-point indices are remarkably similar for both present and future time periods, with correlation coefficients  $>0.9$  for both the monthly and DJF time series. Differences between the global and regional time series are small and

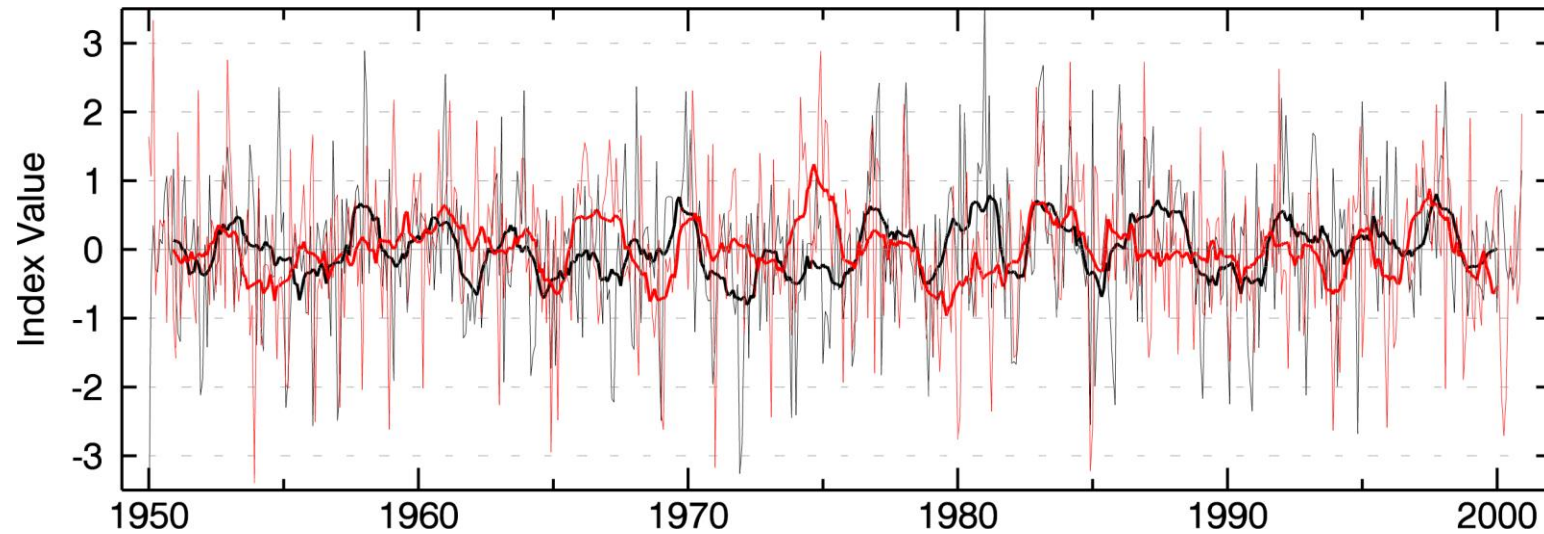


**Figure 2.1** The 1950-2000 PNA index for all months for global NCEP (black) and ECHAM5 (red). The bold lines represent the 12-month smoothed data.

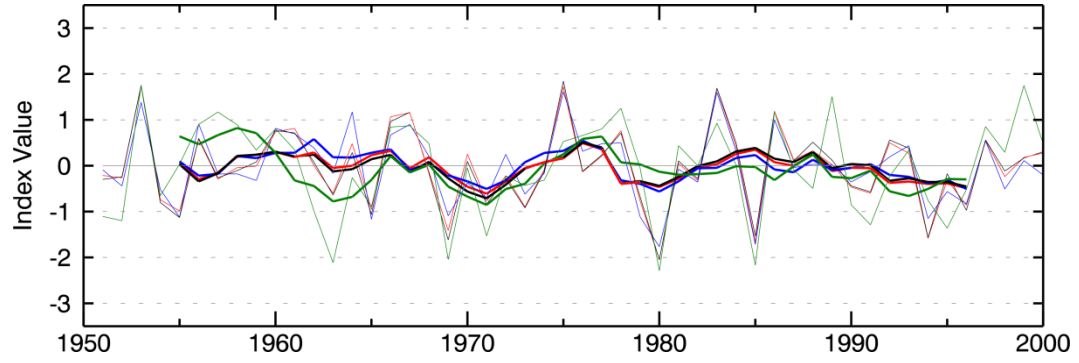


**Figure 2.2** The 1950-2000 PNA index for the DJF winter season for the global ECHAM5 4-point pointwise index (black lines), and global ECHAM5 modified 3-point pointwise index (red lines), for regional ECHAM5 modified 3-point index (blue lines), and the global ECHAM5 RPCA (green lines). The bolded lines represent the 5-year smoothed data.

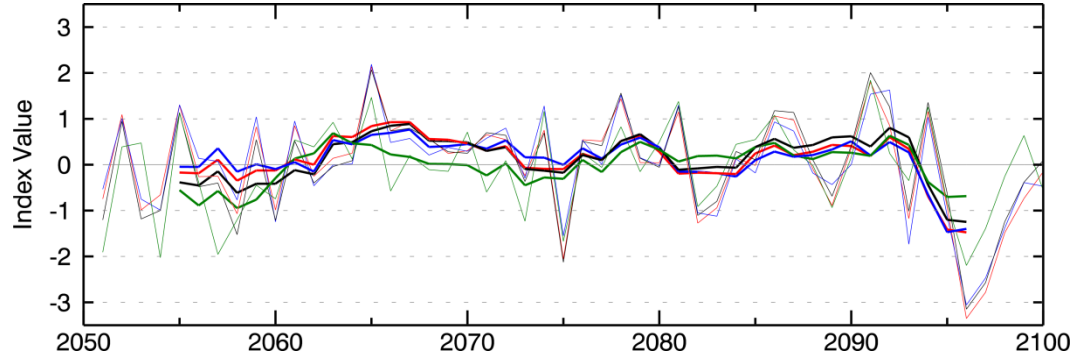


**Figure 2.3** As in Fig. 2.2, for the 2050-2100 PNA indices.

can be attributed to the atmospheric dynamics equations in the respective models that lead to slightly different simulations of 500-hPa geopotential heights. The means of the 20C and A2 ECHAM5 time series are not significantly different according to a Student's t-test, with respective means of  $-0.03 \pm 0.85$  and  $0.004 \pm 1.10$ ; however, the variances of the two time series are significantly different at the 95% level, according to an F-test. The mean of the 20C time series is not significantly different from the CPC, which exhibits a mean of  $0.02 \pm 1.06$  for 1950-2000, while the variances are significantly different at the 90% level. The variability in the ECHAM5 indices increase slightly in the future, as indicated by anomalously low DJF values toward the end of the 21<sup>st</sup> century and as reflected in the results of the F-test. The time series extracted from the RPCA during the PNA pattern calculations also compares well to both pointwise methods. Because the RPCA uses geopotential height information from the entire Northern Hemisphere, discrepancies exist between the RPCA and the global 4-point linear pointwise indices; nonetheless, the time series exhibit correlation coefficients  $>0.7$  for both the present and future time periods.

Based on the analyses of each index calculation method, we use the global 4-point linear pointwise index (Eq. 2) in all regional surface climate analyses presented here. We believe this index best represents the PNA teleconnection in both the global and regional models. Because we cannot calculate an index using the RPCA or the 4-point linear pointwise method for RegCM3, yet RegCM3 is nested within and forced by the global ECHAM5 model, we find it most appropriate to use the global 4-point linear pointwise index combined with the RegCM3 output. From hereafter, unless

otherwise specific, all references to the “PNA index” refer to the global model (for both ECHAM5 and NCEP) 4-point linear pointwise index.

The PNA varies on both intraseasonal (2–90 days) and interannual (2–20 years) time scales (Feldstein, 2000). The model simulation output used for this study is limited to monthly averages; thus, our time series analysis focuses on the intraannual (60–120 days) and interannual time periods. We calculate 12-month smoothed power spectra for the monthly global NCEP and ECHAM5 PNA index time series for the 20C and A2 simulations, as well as for the regional ECHAM5 time series (Fig. 2.4). Each line displays a comparable spectral shape: the spectra are generally “red” in character, indicating there is more power at lower frequencies; however, the amount of power associated with very low frequencies (greater than 5 years) gradually tapers off. The spectral pattern for NCEP-GCM exhibits a seasonal and annual signal with peaks at 3, 4, 6, and 12-24 months. A strong low-frequency signal is present between 3-7 years, a likely connection to ENSO. The CPC states that positive (negative) phase PNA events are often associated with warm (cold) phase ENSO events, which supports the 3-7 year period seen in the NCEP-GCM power spectra. Both global and regional ECHAM5 generally demonstrate low-frequency dominant spectra as well, but with some obvious differences from NCEP-GCM and between time periods. The global and regional spectra show similar shapes and generally produce peaks in the same locations, particularly at higher frequencies. At frequencies lower than ~12 months, the spectra begin to deviate slightly, especially with ECHAM5 years 1950-2000. While the global model produces spectral peaks at

~12 months and again between 3-7 years (Fig. 2.4, solid green line), the regional model fails to produce a peak at 12 months and the width of the low-frequency peak extends from ~2-10 years (dashed green line). The amount of power associated with this low-frequency peak, however, is comparable to NCEP-GCM. Both ECHAM5 2050-2100 spectra fail to produce a low-frequency peak at this location, which suggests a much more periodic index in the future and more frequent fluctuations between positive and negative PNA modes.

## 2.5 Spatial variability

The PNA displays a robust spatial pattern in the global NCEP Reanalysis (Fig. 2.5a); the four centers of action used in the index equation appear as distinct regions of high and low variability in the 500-hPa geopotential height field. The rotated EOF for the ECHAM5-GCM 20C simulation displays a comparable spatial pattern but with lower magnitudes than that of the NCEP (Fig. 2.5b). The difference between the global NCEP and ECHAM5 simulations are also reflected in the mode of variability and amount of explained variance calculated from the rotated EOF analysis (Table 2.1). The PNA appears as the second leading mode of variability in the NCEP for 1950-2000 and this mode explains 13.07% of the variance in the 500-hPa geopotential height field. The ECHAM5 PNA patterns appear as different modes for different time periods.

While the general PNA spatial pattern remains the same throughout the 21<sup>st</sup> century, there are notable changes in the orientation of the pressure centers,

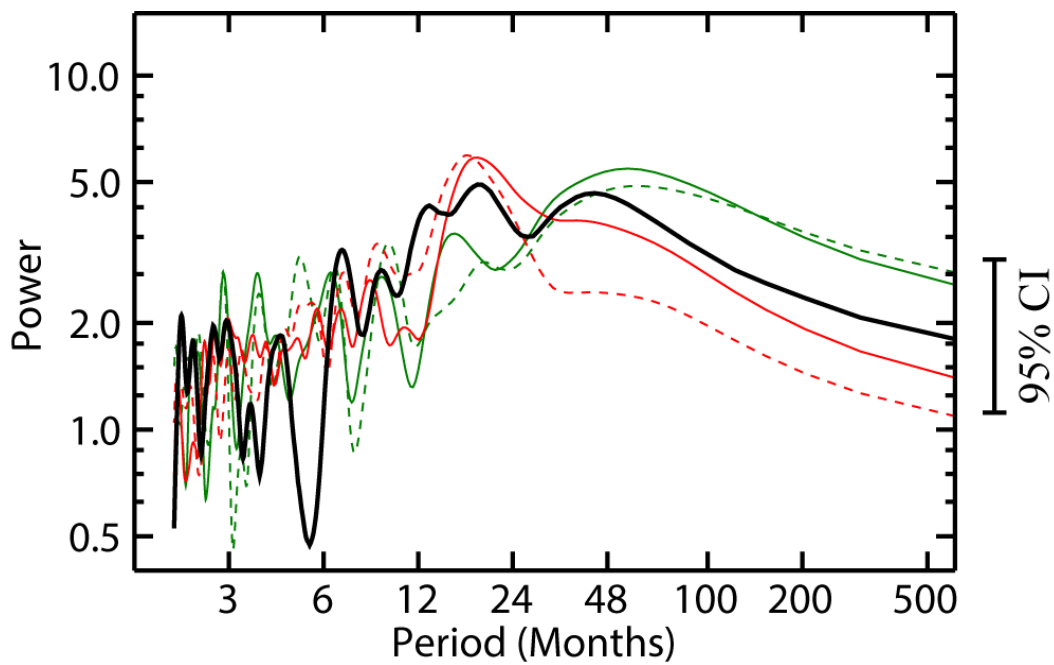


**Figure 2.4** Smoothed power spectra for monthly PNA index time series calculated from the 1950-2000 NCEP Reanalysis (black line), and ECHAM5 (green line) years 1950-2000 and 2050-2100 (red line). The dotted lines show the regional ECHAM5 spectra for the same years. The 95% confidence interval is displayed.

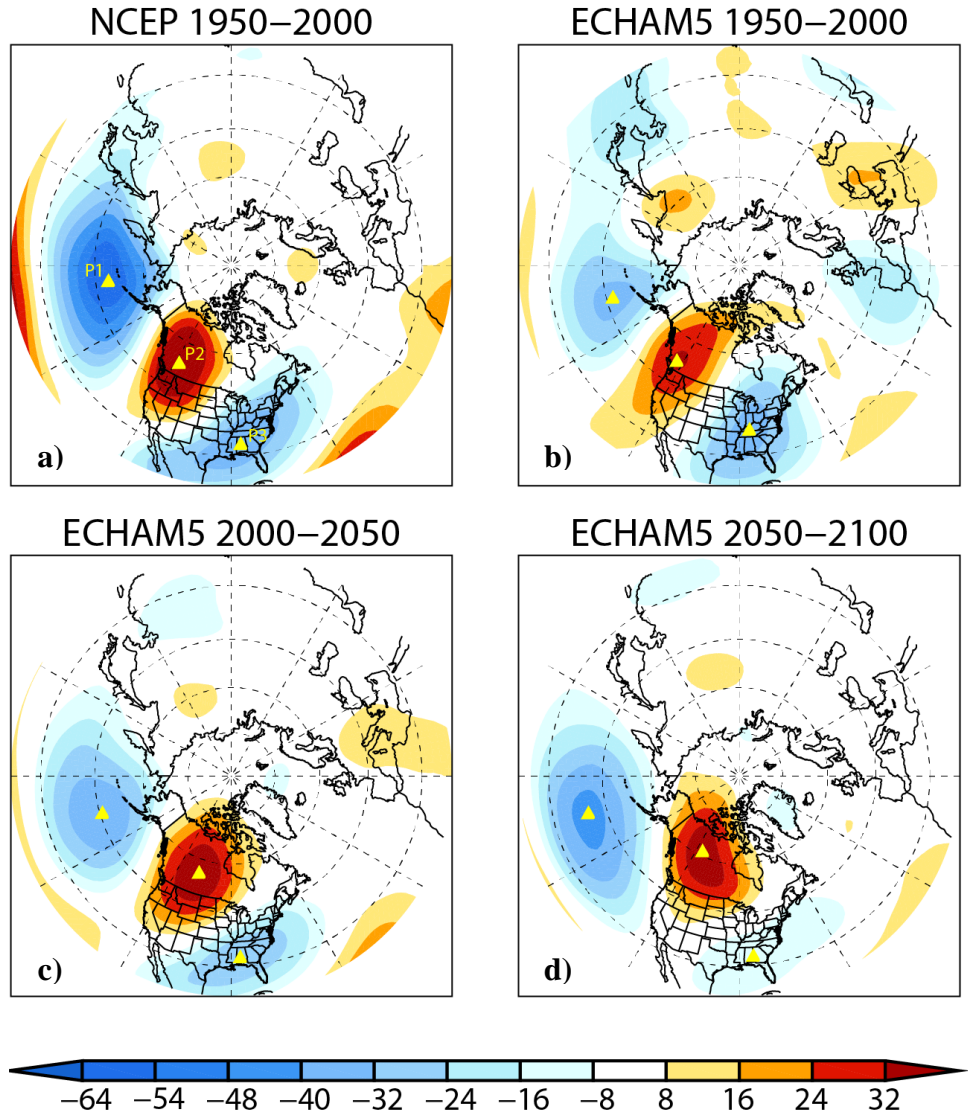


**Figure 2.5** The January Pacific-North American patterns as shown by rotated EOFs for a) NCEP 1950-2000, b) ECHAM5 1950-2000, c) ECHAM5 2000-2050, and d) ECHAM 2050-2100. Centers P1, P2, and P3 are labeled on the NCEP map and marked by yellow triangles on the ECHAM5 maps. The anomalies are standardized by the respective climatology for each time period. The rotated EOF modes and explained variance for each time period are listed in Table 2.1

**Table 2.1** Results from the rotated EOFs shown in Fig. 2.5. The EOF analyses were divided into 50-year increments to show changes in variability.

Model (Time period)	Mode	EV (%)
NCEP (1950–2000)	2	13.07
ECHAM5 (1950–2000)	5	6.20
ECHAM5 (2000–2050)	3	8.85
ECHAM5 (2050–2100)	10	2.63

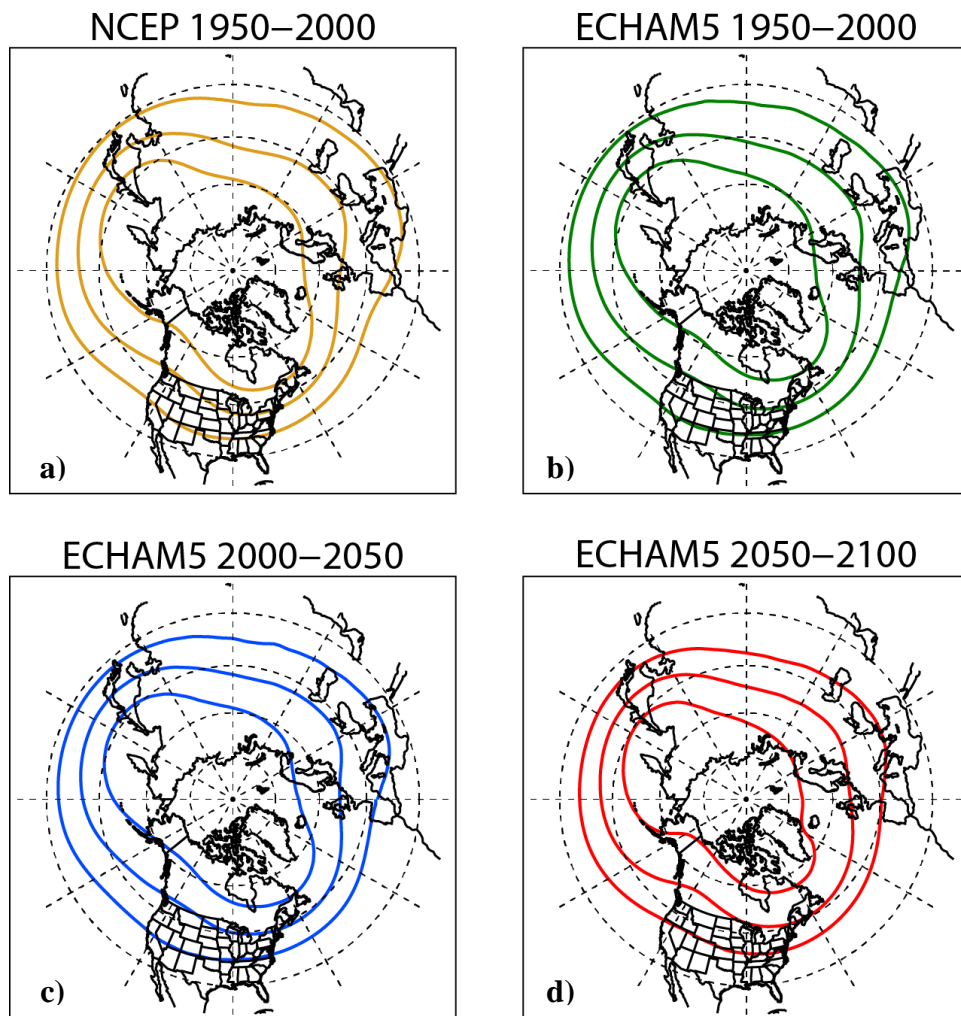


**Figure 2.6** 500-hPa surface contours for a) NCEP 1950-2000, b) ECHAM5 1950-2000, c) ECHAM5 2000-2050, and d) ECHAM 2050-2100. The northernmost contours are for the 5280-m surface, the middle contours are for the 5460 m surface, and the southernmost contours are for the 5640 m surface.

particularly the high over Western North America (P2; Fig. 2.5c,d). This behavior is further illustrated with 500-hPa geopotential height surface contours (Fig. 2.6). NCEP reveals a clear trough-ridge pattern over the North Pacific and across the west coast of North America. For the ECHAM5 period 1950-2000, the distinction between the trough and ridge is less defined, resulting in the weak PNA pattern in Fig. 2.5b. During 2000-2050 and 2050-2100, a deepening trough in the North Pacific is accompanied by more ridging over the Pacific Northwest and Western Canada, indicating a shift from generally zonal flow in the present (1950-2000) to more meridional flow in the future (2050-2100).

In addition to an overall deepening of the Aleutian low (P1) between the three analyzed ECHAM5-GCM time periods, the location of this center shifts nearly  $10^{\circ}$  equatorward by the end of the 21<sup>st</sup> century (Fig. 2.5). This transition is accompanied by a northward shift of about  $10^{\circ}$  and a counter-clockwise rotation in the orientation of the P2 due to the strengthening and widening Aleutian low. The magnitude of P3 weakens throughout the three time periods, becoming nearly nonexistent by the end of the 21<sup>st</sup> century. The increase in the north-south distance between P1 and P2 suggests increasing meridional flow, which is typically associated with positive PNA indices. These changes lead to significant climatic impacts over North America, notably the West coast; these details are discussed in Section 2.7 of this paper.

## 2.6 Relationship to present climate

Strong correlations exist between the winter PNA monthly index and both surface temperature and precipitation in North America (Leathers *et al.*, 1991). These relationships, in turn, lead to antecedent conditions and slightly less well defined correlations between the PNA and snow water equivalent and soil moisture. We focus on the analysis of four surface climate variables: 2-m air temperature (TA), total precipitation (RT), upper level (3 cm) soil moisture (SMU), and snow water equivalent (SWE). Positive and negative PNA phases or events will be referred to as PNA+ and PNA-, respectively.

### 2.6.1 Correlation analysis

To assess the association between the PNA and surface climate fields, we computed Pearson correlation coefficients ( $R^2$ ) at each grid cell of the RegCM3 domain (Fig. 2.7). The  $R^2$  values are based on a temporal linear regression between the DJF PNA index time series and the variable anomalies for the nested RegCM3 regional climate model. The resulting coefficients quantify the degree to which the variable anomalies at each grid cell co-vary with the index time series, and thus larger values indicate stronger relationships.

#### 2.6.1.1 2-m air temperature

The relationship between the PNA index and 2-m air temperature is well defined, with a large area of a strong positive correlations dominating much of the

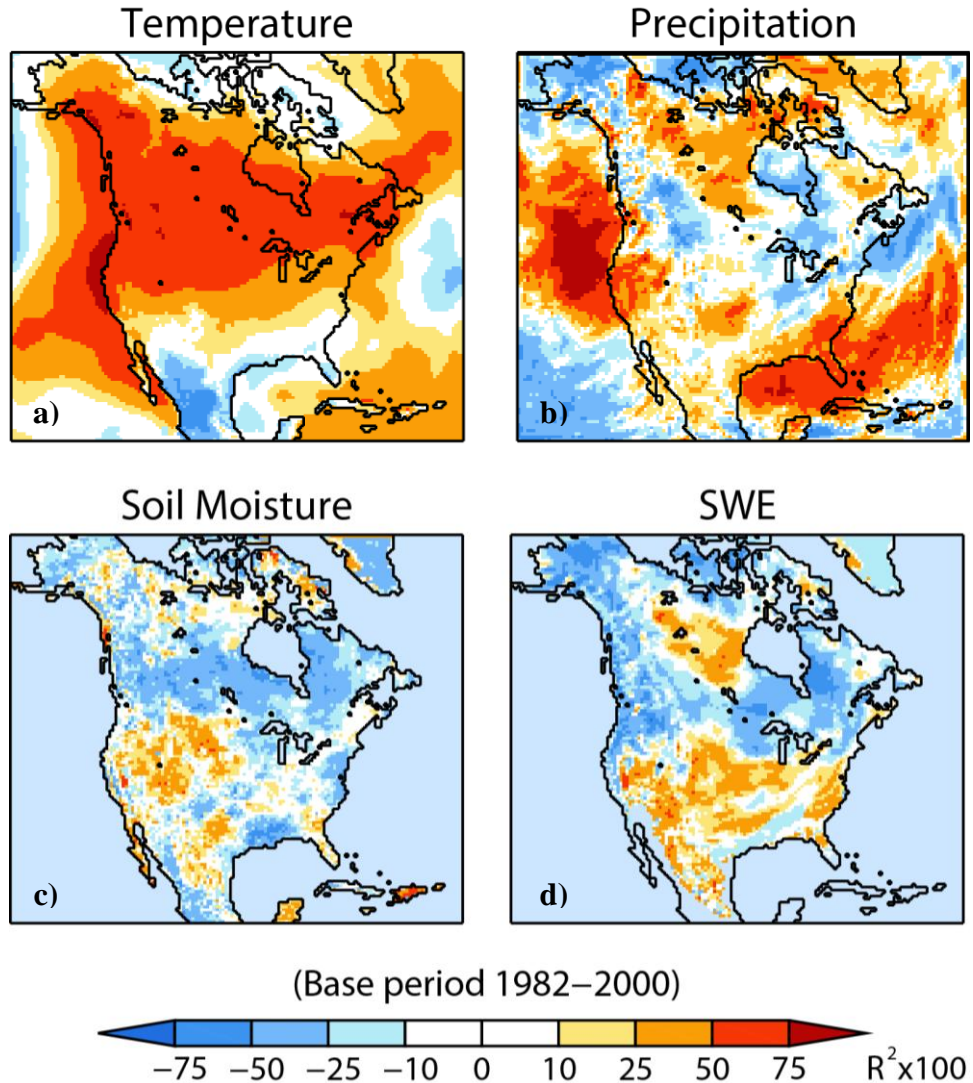


**Figure 2.7** Correlations between the PNA index and surface field anomalies for the 1982-2000 regional NCEP Reanalysis model run. The variables shown are a) 2-m air temperature, b) DJF precipitation, c) JJA soil moisture, and d) March snow water equivalent. The plotted values are the temporal correlations between the DJF PNA index and the anomaly value at each grid point for the given time period. The anomalies are departures from the 1982-2000 climatology.

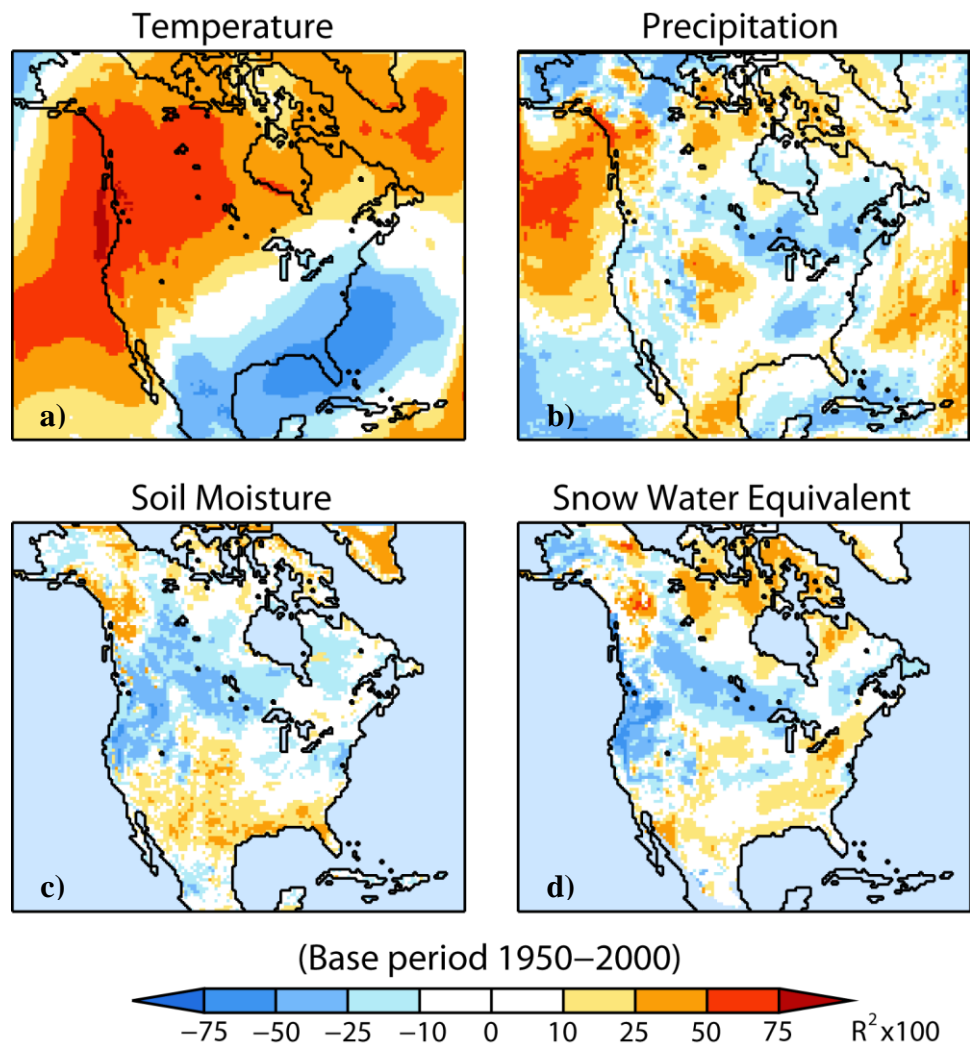


**Figure 2.8** As in Fig. 2.7, for the regional ECHAM5 simulation for the years 1950–2000. The anomalies are departures from the 1950–2000 climatology.

mid- and high latitudes of North America and extending down the west coast past Baja California (Fig. 2.7a). The positive correlation transitions to neutral in the southern U.S. and switches to a negative correlation over the southeast and over the Caribbean and most of Mexico. The correlation patterns derived from the regional ECHAM (“ECHAM5”) simulations (Fig. 2.8a) bear a strong resemblance to those from the regional NCEP simulations (“NCEP”) with some key differences associated with the dissimilarity of the positioning and strength of the Aleutian low in each model (Fig. 2.5). The ECHAM5 temperature correlations are very similar to those produced by NCEP, with the highest correlation values situated just off the coast of the Pacific Northwest (Figs. 2.7a and 2.8a). The influence of temperature across the United States is slightly stronger and extends farther east according to NCEP, while the strongest correlation values in ECHAM5 are concentrated in the northwestern region of the continent.

The most noticeable differences between the NCEP and ECHAM5 correlation patterns appear in the southeast United States where a relatively strong negative correlation is present in ECHAM5, but not in the NCEP output. The positive correlation values associated with the NCEP temperature data extend south of the Great Lakes, whereas this region in ECHAM5 shows no relationship between the PNA and temperature. The centers of action located over North America are spatially much different between NCEP and ECHAM5 (Fig. 2.5). The high pressure center situated over western North America in NCEP is much larger and influences more of the U.S. Pacific Northwest than does the same center in ECHAM5. A relatively strong high

pressure center is partly visible off the southeast coast in both models, yet appears stronger in NCEP and is likely the reason for the positive correlation values seen over the Caribbean Sea (Fig. 2.7a). The corresponding area of high pressure is weaker in ECHAM5 and this is reflected in the weaker correlation values in this region, as well as the stronger negative influence over Florida and the rest of the southeast United States.

#### *2.6.1.2 Precipitation*

The observed relationship between the PNA and precipitation is strong, particularly over the eastern Pacific Ocean and the Gulf of Mexico (Fig. 2.7b). Meridional flow characteristic of a PNA+ brings subtropical air farther north along the west coast of North America and pulls moisture from the Gulf of Mexico, resulting in anomalously wet conditions in the northwest and southeast sectors of North America. The Aleutian low is responsible for bringing warm, moist air associated with “Pineapple Express” events from the subtropics toward the west coast of North America, resulting in the strong positive correlations in this region. The comparably weak P1 center in ECHAM5 suppresses this atmospheric river of moisture, and consequently the influence of the PNA on precipitation is much weaker in ECHAM5, particularly in this region (Fig. 2.8b). The ECHAM5 highest magnitude correlations reside mostly over the Eastern Pacific, the Gulf of Alaska, and extend over land into Western Canada and SW Alaska. The NCEP correlations conversely indicate a relatively strong positive influence over the Pacific Northwest. The largest difference

between the ECHAM5 and NCEP precipitation patterns is the lack of a positive correlation in the in the Gulf of Mexico and Caribbean Sea. The ECHAM5 simulations display a negative correlation of similar strength, but the spatial extent of the pattern is more limited. A possible explanation for this discrepancy goes back to the sign and strength of the low pressure center located over southeast North America. This low pressure is much less defined in the ECHAM5 output, a difference that could very well suppress the formation of precipitation in the model.

#### *2.6.1.3 Soil moisture*

The relationships between the PNA index time series and SMU and SWE are less defined, yet still show coherent patterns that are related to the hydrological effects of temperature and precipitation. The correlations with SMU shown here are for the summer months of June-July-August (JJA) since climatological changes in soil moisture, especially in the West, are most prominent during the summer. Influences of the PNA over precipitation and snow water equivalent (discussed in the next section) contribute to the timing of spring onset, the persistence of mountain snowpack, which ultimately determine water availability during the summer months. NCEP generally shows a positive relationship between the PNA and soil moisture in western North America, while a negative relationship is present throughout much of Canada (Fig. 2.7c). Due to the discrepancies between the magnitudes of P1 and P3 between NCEP and ECHAM5 and the consequences these differences have on the precipitation correlations, the locations of the SMU correlations in the ECHAM5 plots

are shifted south (Fig. 2.8c). As a result, the soil moisture correlation is negative over the Pacific Northwest, parts of southern Alaska, and positive along the Gulf Coast, a large contradiction to the NCEP plot. These differences extend across the contiguous United States, as well, with the correlation fading to near-zero along the eastern seaboard in the ECHAM5 plots, but remaining moderately negative for NCEP.

#### *2.6.1.4 Snow water equivalent*

Much of the Northern Rockies, Canada, and into Alaska show a negative SWE correlation for NCEP, consistent with the positive relationship between the PNA and temperature (Fig. 2.7d). PNA+ patterns are associated with positive temperature anomalies in these regions, consequently resulting in more precipitation falling as rain rather than snow. Thus, these areas show an overall negative correlation between the PNA and SWE. This negative relationship with SWE is reinforced in some regions by a negative correlation with precipitation, especially in north-central Canada west of the Hudson Bay. Contrary to the soil moisture maps, the SWE correlation patterns for NCEP and ECHAM5 are strikingly similar. Comparable to NCEP, ECHAM5 produces a relatively strong negative correlation throughout much of Canada and western North America, with positive correlations encompassing most of the United States. The most noticeable difference is the strengths of the correlation coefficients, as NCEP is about 25% stronger. In addition, ECHAM5 displays a region of positive correlations in extreme northwest Canada, a likely side effect of the extension of the positive precipitation correlation over land.

It is important to remember that many of these relationships between the PNA and climate, with the exception of temperature and precipitation in a few regions, are represented by correlation coefficients ranging between  $30 \leq R^2 \leq 50$ . While these values are high enough to suggest the presence of a relationship between the PNA and climate, it is evident that the PNA is only one of the many influences on climate in these regions.

### 2.6.2 Extremes

The correlation analysis examines how well the PNA and climate variables are related, but such an analysis does not quantify this relationship. We therefore perform an “extreme index” analysis to illustrate the influence of “extreme” PNA events on the selected climate variables. Our analysis consists of composite anomaly maps for the top (bottom) 33% of positive (negative) PNA years in which the index value is greater than (less than) 0.5 for ECHAM5 (Figs. 2.9-2.11). Due to the limited number of years available for the regional NCEP simulation, we chose the top and bottom 66% of PNA index years to ensure an adequate number of years in each composite. The regional NCEP and ECHAM5 maps are grouped for positive (Fig. 2.9) and negative (Fig. 2.10) indices for the present time period. The patterns displayed by the extremes maps generally resemble those seen in the correlation analysis (Figs. 2.7 and 2.8) because, especially for temperature, a positive correlation will relate to a positive anomaly. The processes involved in changes in SMU and SWE are more complex, however, and so

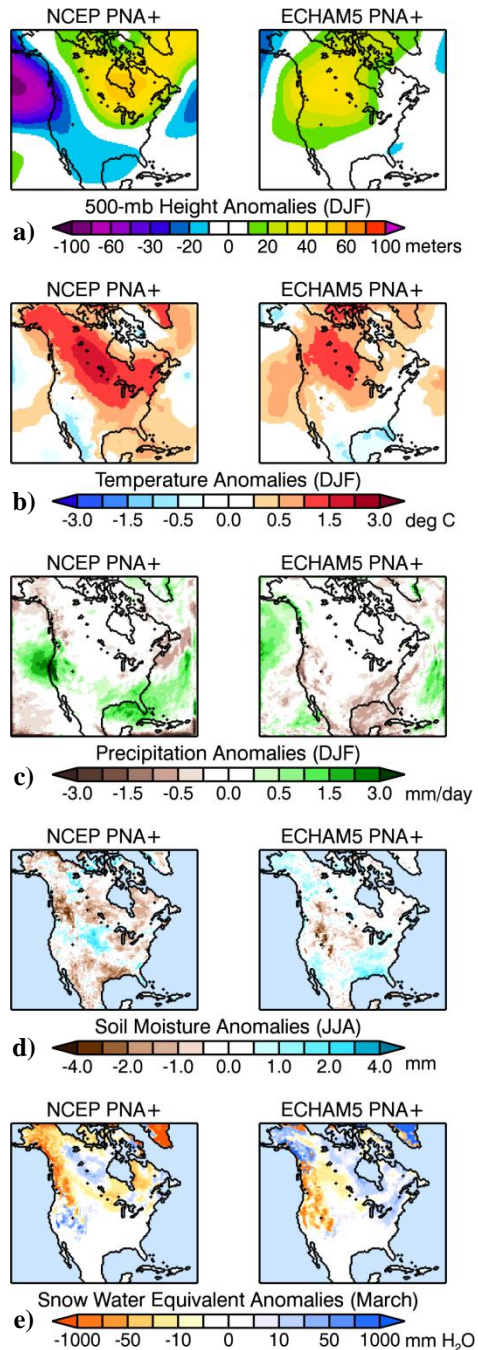


**Figure 2.9** Composite anomaly maps for the top 66% of PNA indices for NCEP years 1982-2000 (left column of figure) and the top 33% of ECHAM5 years 1950-2000 (right column of figure). The variables shown are a) 500-hPa geopotential heights, b) 2-m air temperature, c) precipitation, d) soil moisture, and e) snow water equivalent (SWE).

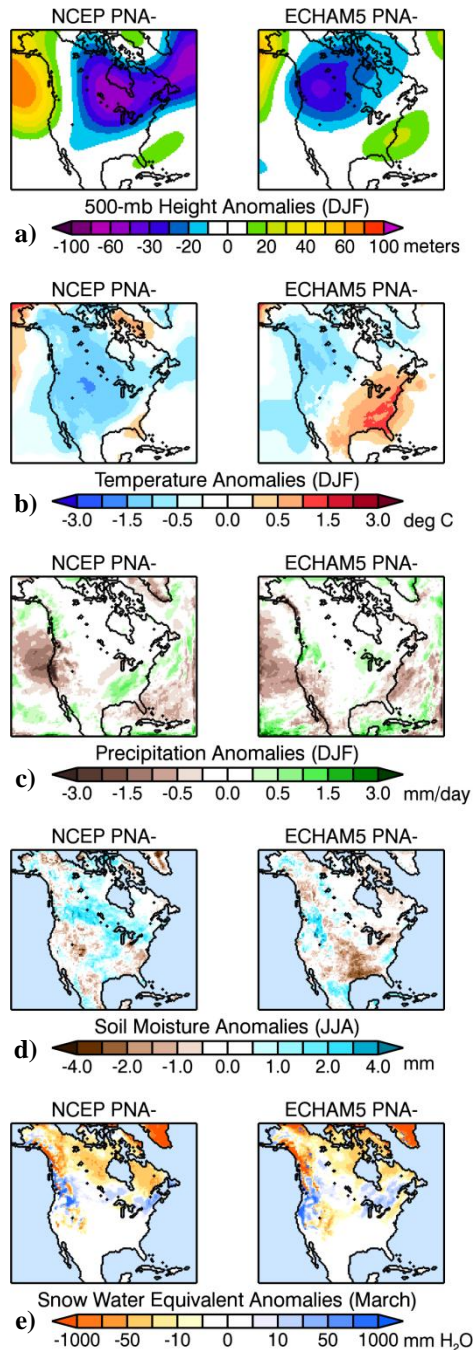


**Figure 2.10** Composite anomaly maps for the bottom 66% of PNA indices for NCEP years 1982-2000 (left column of figure) and the bottom 33% of ECHAM5 years 1950-2000 (right column of figure). The variables shown are a) 500-hPa geopotential heights, b) 2-m air temperature, c) precipitation, d) soil moisture, and e) snow water equivalent (SWE).

their patterns integrate several climate factors, including the effects of temperature and precipitation.

### *2.6.2.1 500-hPa geopotential heights*

PNA+ phases are characterized by a negative geopotential height anomaly off the Northwest coast (Fig. 2.9a), while PNA- phases show positive anomalies over northwest North America and Alaska and negative anomalies over the southeast U.S. (Fig. 2.10a), consistent with the EOF analysis (Fig. 2.5). The variations in geopotential heights drive changes in atmospheric circulation associated with the jet stream, thereby affecting surface climate variables. In ECHAM5, the relative strength of P2:P3 is much smaller than in NCEP, indicating a weaker ridge over North America in ECHAM5 and resulting in a lack of negative height anomalies associated with P3. The positive height anomalies associated with a PNA+ pattern result in positive temperature anomalies for both the NCEP and ECHAM5 simulations, and the patterns are opposite for PNA- events. These relationships are consistent with the positive correlations between PNA index values and temperature anomalies (Figs. 2.7 and 2.8).

### *2.6.2.2 Near-surface air temperature*

The magnitude of the temperature anomalies associated with PNA+ patterns are similar in the NCEP and ECHAM5 simulations, with maximum values reaching 1.5-2°C; however, the location of these maxima differs (Figs. 2.9b). The strongest influence of a PNA+ in ECHAM5 is over Northwest Canada, whereas NCEP displays

a larger area of maximum values over a much larger area of influence. NCEP displays positive anomalies throughout most of the domain, while ECHAM5 shows zero and weak negative anomalies in the southwest.

The negative temperature anomalies in PNA- are less negative in ECHAM5 than those of NCEP by about 1°C, as well contained to the northwest region of North America. This is consistent with the discrepancies between the two models as seen in both the EOF and correlation analyses; ECHAM5 features a weaker P2 center leading to weaker negative anomalies during PNA- (Fig. 2.10b). The largest difference between NCEP and ECHAM5 during PNA- is the region of positive anomalies in the southeast on the ECHAM5 map. This region is consistent with, but stronger and opposite in sign of anomalies on the PNA+ map, and again related to the relative weakness of the P2 center.

### *2.6.2.3 Precipitation*

The precipitation anomalies differ substantially between the two models (Figs. 2.9c and 2.10c). A relatively strong positive precipitation anomaly on the order of 1.5-3 mm/day is located off the West coast in NCEP, representing the influence of the Pineapple express during strong PNA+ events. This feature is nonexistent in ECHAM5, a consequence of weak centers of action, particularly the Aleutian low. The Southern U.S. is another area of disagreement, where NCEP shows substantial moisture associated with the low pressure over the warm Gulf of Mexico. ECHAM5 exhibits drying in this region due to insufficient convection from a weak P3 center, a

discrepancy that extends throughout the southeast. The NCEP maps are mirror images for PNA- events, while ECHAM5 continues to exhibit persistent drying throughout much of the domain.

#### *2.6.2.4 Soil moisture*

Changes in soil moisture during positive and negative PNA phases are a result of the combination of temperature and precipitation, as well as the presence of persistent snowpack in higher elevations (Figs. 2.9d and 2.10d). The extremes shown here are for the JJA summer months, as in Figures 2.7-2.8. Positive PNA events bring negative soil moisture anomalies to most of North America in NCEP due to strong ridging, except for the region encompassing the upper Midwest, while negative PNA events produce opposite results. Extreme drying in the Canadian Rockies can be linked to SWE (see the next section). The large negative anomaly in the mountainous and high plains regions of the United States during negative events is likely related to the lack of precipitation, and thus snowfall, during the winter months.

Summer soil moisture anomalies in the southeast U.S. cannot be linked to winter snowfall, and thus any changes in this region are likely linked to temperature and convective precipitation. These influences create widespread soil moisture deficits throughout much of southern North America during PNA+ due to high pressure and hot temperatures. Atmospheric flow associated with PNA- allows for the intrusion of more moisture to this area, resulting in more precipitation events leading to positive soil moisture anomalies. ECHAM5 presents large differences from NCEP

associated with the discrepancies with precipitation, and thus soil moisture deficits in any regions that lack precipitation are amplified during the summer months.

#### *2.6.2.5 Snow water equivalent*

SWE is dependent on both snowfall accumulation as well as persistent snowpack in higher elevations, thus changes in temperature have a dramatic effect on these anomalies since positive temperature anomalies (as those seen in PNA+ events) will cause more precipitation to fall as rain rather than snow. As in the correlation analysis, we display the SWE anomalies for March relative to the DJF PNA index. The differences in snow water equivalent (SWE) between positive and negative PNA appear as almost mirror images in both models (Figs. 2.9e and 2.10e). In both NCEP and ECHAM5, positive (negative) PNA events result in negative (positive) SWE anomalies, as seen most clearly throughout the Canadian and U.S. Rockies and the Pacific Northwest Coastal Range. The Alaskan panhandle, however, experiences decreases in SWE for both positive and negative PNA events. During PNA+ events, ridging over North America is responsible for these decreases, yet the negative anomalies during PNA- is likely a combination of the weak influence of both temperature and precipitation in this region. If a PNA- does accumulate snowpack during the winter months, then the March SWE anomalies will be negative relative to events where snowpack does accumulate.

## 2.7 Relationship with future climate

To investigate possible future changes in PNA, we apply our analyses to the regional ECHAM5 runs for the IPCC SRES A2 simulations for years 2001-2100. The time period over which the indices are standardized plays a large role in the resulting index value. In the A2 simulations, the effects of global warming increase geopotential heights that ultimately present biases in the PNA indices when using the 1950-2000 climatology. Therefore, the anomalies used in the correlation and extreme analyses for the future are departures from the 2050-2100 climatology. This method effectively removes the influences of global warming and allows us to focus on any absolute changes that would otherwise get overwhelmed by increases in global temperatures.

### 2.7.1 Correlation analysis

The correlation between the future PNA (2050-2100) and each of temperature, precipitation, soil moisture, and SWE anomalies are shown in Figure 2.11 and the magnitude of the differences between the future and present correlation  $R^2$  values are shown in Figure 2.12. Positive (negative)  $R^2$  values correspond to stronger (weaker) correlations in the future years.

The future spatial pattern of 2-m air temperature correlation is similar to that of the present climate (Fig. 2.8a), with the only major differences over the northern latitudes around Greenland where the strength of the correlation becomes much weaker in the future (Figs. 2.11a and 2.12a). In contrast to temperature, the

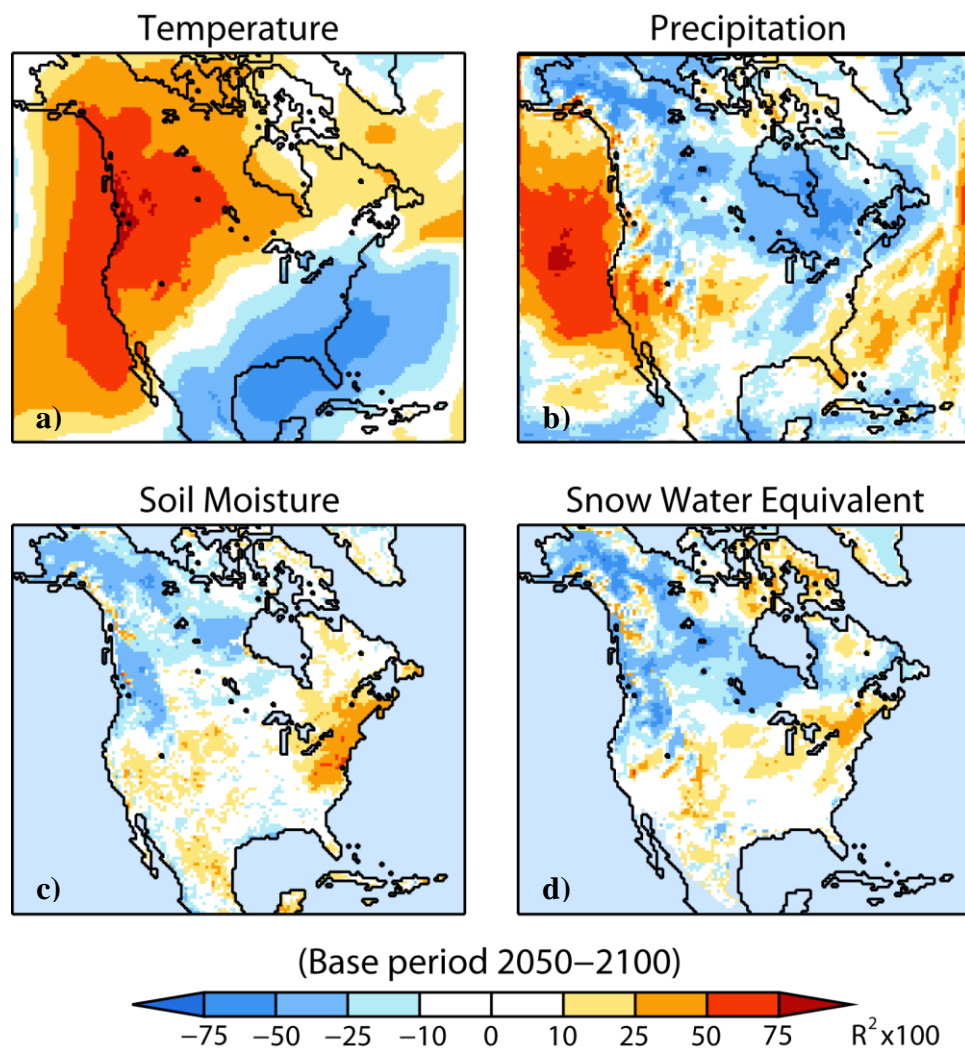


**Figure 2.11** Correlations between the PNA index and surface field anomalies for the regional ECHAM5 years 2050-2100. The variables shown are a) 2-m air temperature, b) DJF precipitation, c) JJA soil moisture, and d) March snow water equivalent. The plotted values are the temporal correlations between the DJF PNA index and the anomaly value at each grid point for the given time period. The anomalies are departures from the 2050-2100 climatology.

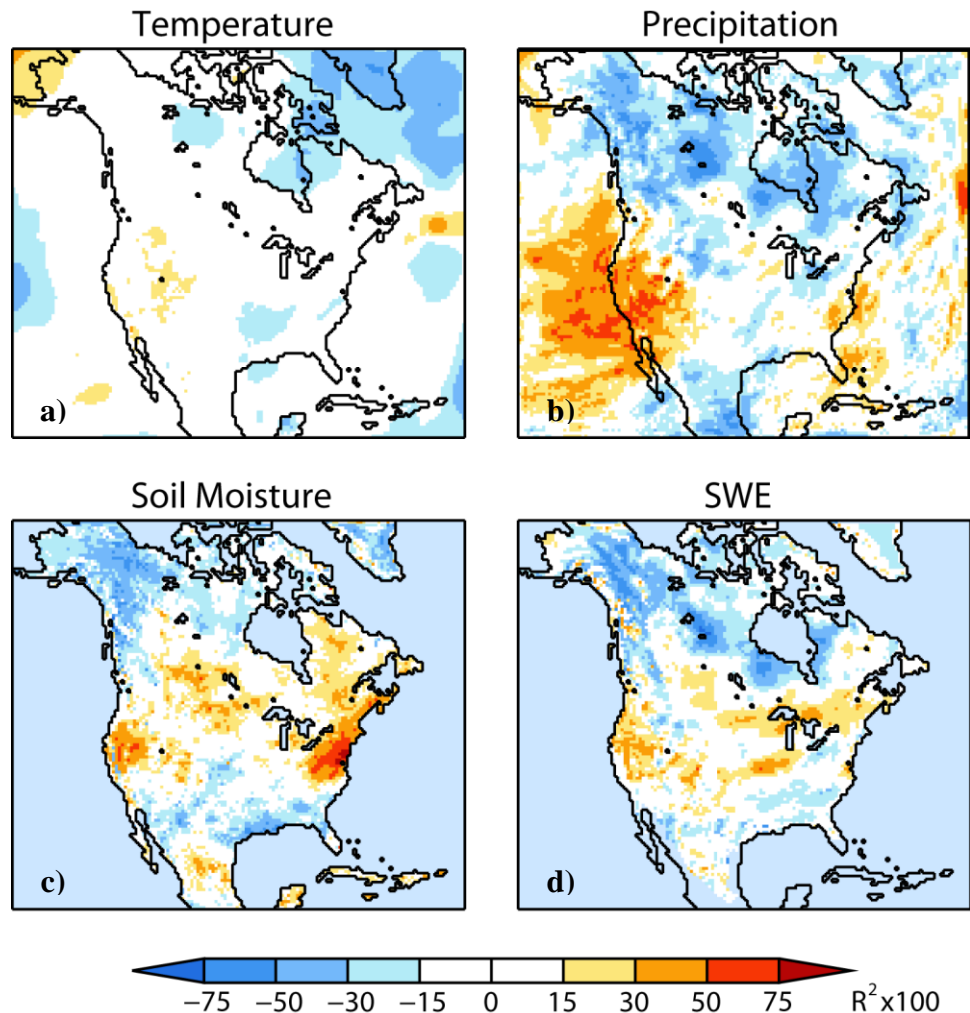


**Figure 2.12** As in Fig. 2.11, for the difference between the regional ECHAM5 years 2050-2100 and 1950-2000.

relationship between the PNA and precipitation changes substantially throughout the domain with relatively large increases in correlations along the West coast of the United States (Figs. 2.11b and 2.12b). Thus, PNA+ events in the future are more strongly associated with increased precipitation in this region, which is likely related to the shift and strengthening of the Aleutian low in the model simulations (Fig. 2.5b-d). The precipitation pattern over most of Canada becomes uniformly negative in the future, indicating a drying associated with PNA+ events (Fig. 2.11b). Again, this change is associated with the shifting of the pressure centers, specifically the counter-clockwise rotation in the orientation of the high positioned over Canada.

Future soil moisture and SWE show a range change throughout the domain with weaker positive correlations and some sign changes over much of Northern Canada and Alaska (Fig. 2.11c,d). This change indicates an overall drying, as PNA+ events are more associated with negative SMU and SWE anomalies in the future. An area of strong positive correlations stands out in the Northeast U.S. for both variables, with the difference in SMU between future and present producing  $R^2$  values close to 0.9 (Fig. 2.12c). The relationship between soil moisture and the PNA completely flips signs in this region however, a change that is possibly related to increased precipitation associated with the shifting pressure centers.

Changes in SWE are less extreme than precipitation and soil moisture, although a notable sign reversal from a positive to a negative correlation occurs in Northern Canada, suggesting an overall decrease in snowfall and/or more melting of the snowpack in that region (Figs. 2.11d and 2.12d). Changes in SWE can be linked

to increases in temperature due to global warming; however, often times circulation changes are the main factor. While increased winter temperatures in the northern latitudes are likely a large contribution to the switch from positive to negative SWE correlations, the strengthening ridge associated with the high pressure center over Canada also plays a role.

### 2.7.2 Extremes

Figures 2.13 and 2.14 show composite anomaly maps for extreme PNA events for the future (2050-2100) ECHAM5 simulations of each of geopotential height, temperature, precipitation, soil moisture, and SWE compared with the present composite anomaly maps. The magnitudes of the future minus present changes in climate are displayed in Fig. 2.15. As in the correlation analysis, the anomalies used here are calculated using the 2050-2100 climatology. In addition, the geopotential heights and temperature data are detrended to remove biases associated with composite maps including a high number of years toward the end of the 21<sup>st</sup> century. Due to global warming, geopotential heights and temperatures increase substantially by the end of the 21<sup>st</sup> century (Fig. 2.16). While using the 2050-2100 climatology is sufficient when computing anomaly time series for the entire time period, as in the correlation analysis, without detrending the individual year anomalies at the end of the 21<sup>st</sup> century are erroneously large and ultimately bias the composite anomaly maps.

Changes in the 500-hPa geopotential heights field are evident for both future positive and negative PNA events (Figs. 2.13a and 2.14a). A strengthening of the

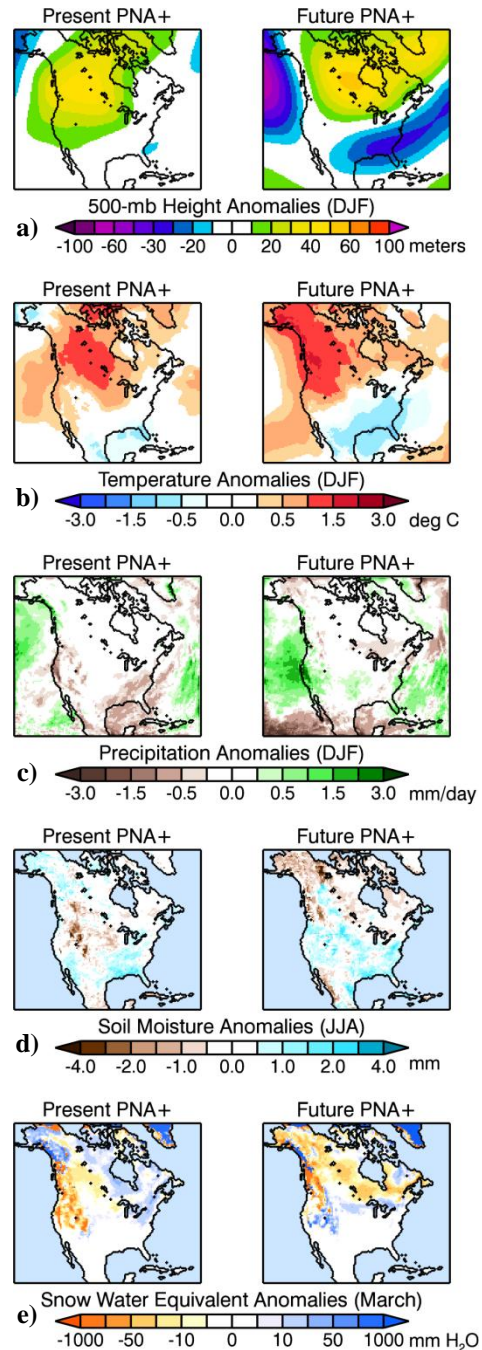


**Figure 2.13** Composite anomaly maps for the top 33% of PNA indices (PNA+) for present (left column of figure) and future (right column of figure) ECHAM5 years. The variables shown are a) 500-hPa geopotential heights, b) 2-m air temperature, c) precipitation, d) soil moisture, and e) snow water equivalent (SWE).

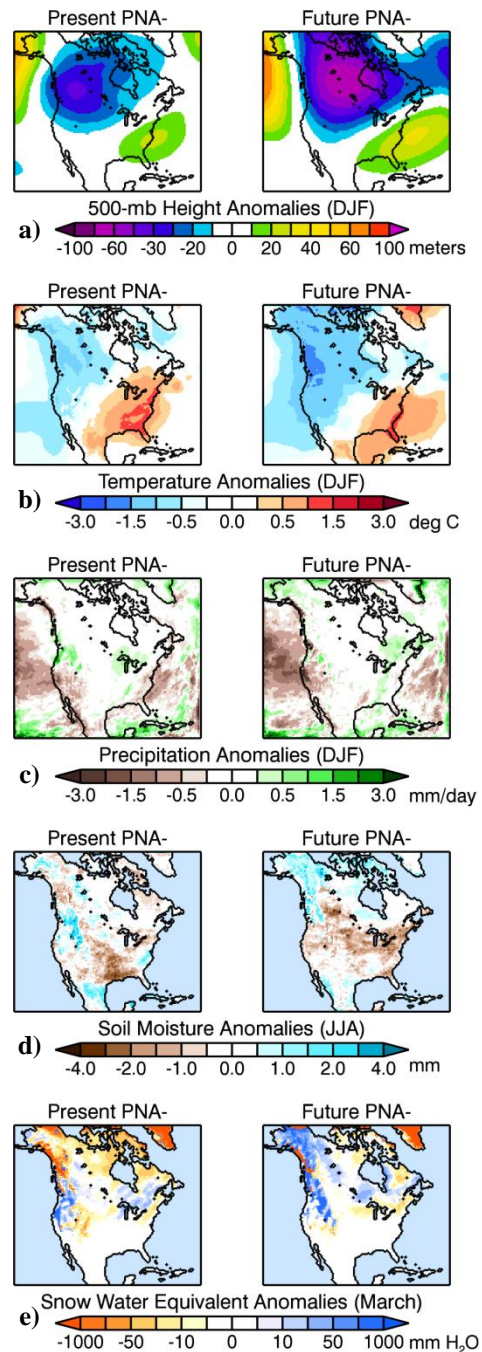


**Figure 2.14** As in Fig. 2.13, for the bottom 33% of PNA indices (PNA-).

500-hPa anomalies in each of the centers of action leads to increases in the magnitudes of these anomalies for both positive and negative events. A large area of negative changes in the heights inhabits the Pacific Northwest under PNA+, suggesting the heights in the future climate are much lower than those of the present (Fig. 2.15a). This reinforces the assertion that the Aleutian low shifts eastward and the strength of the low increases during PNA+ events. On the other hand, the PNA- case shows a positive change in heights in North Pacific, indicating that future height anomalies become increasingly larger during PNA- events, another consequence of a stronger P1 center of action.

Similar to geopotential heights, the largest changes in temperature also occur during PNA- events (Figs. 2.13b and 2.14b). The negative anomalies present in the northwest part of the domain become less negative, while the positive anomalies in the Southeast United States get stronger, indicating an overall warming trend throughout the entire domain during PNA+ events (Fig. 2.15b). The greatest warming occurs throughout Alaska and Canada, with the maximum differences between the future and present scenarios reaching 1.5-3°C.

Changes in precipitation and soil moisture are closely related to each other, as locations of increased (decreased) precipitation generally coincide with locations of increased (decreased) soil moisture (Figs. 2.13c,d and 2.14c,d). These anomalies are also consistent with the circulation patterns represented by the 500-hPa heights (Fig. 2.13a and 2.14a). Areas of higher (lower) height anomalies correspond to a decrease (increase) in precipitation and soil moisture. Snow water equivalent displays a direct

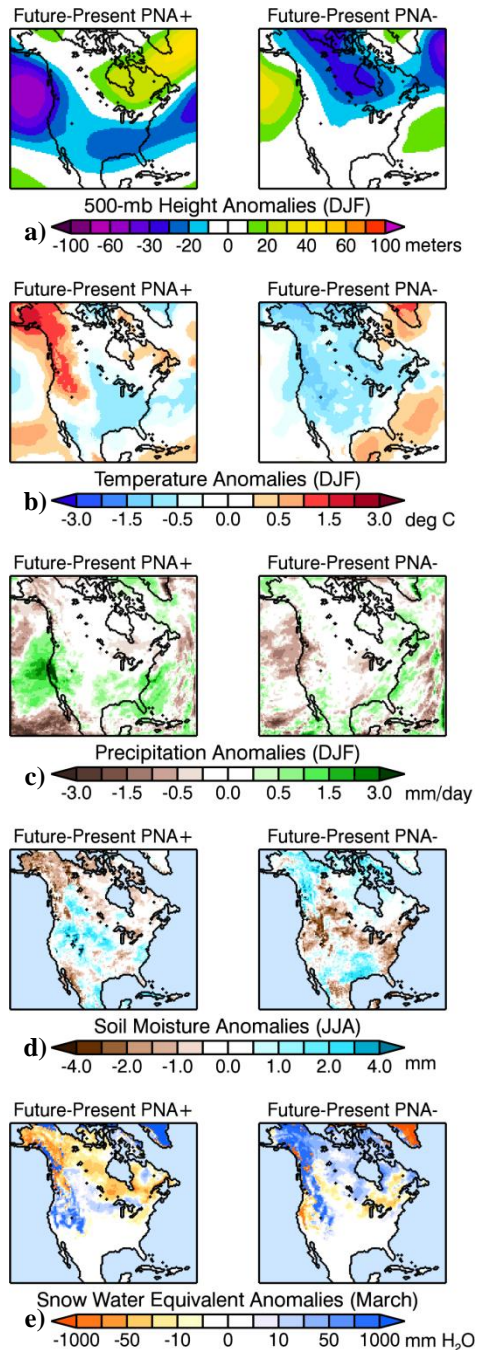


**Figure 2.15** Differenced composite anomaly maps for the top 33% (PNA+; left column of figure) and bottom 33% (PNA-; right column of figure) of PNA indices for ECHAM5 for 2050-2100 minus 1950-2000. The variables shown are a) 500-hPa geopotential heights, b) 2-m air temperature, c) precipitation, d) soil moisture, and e) snow water equivalent (SWE).

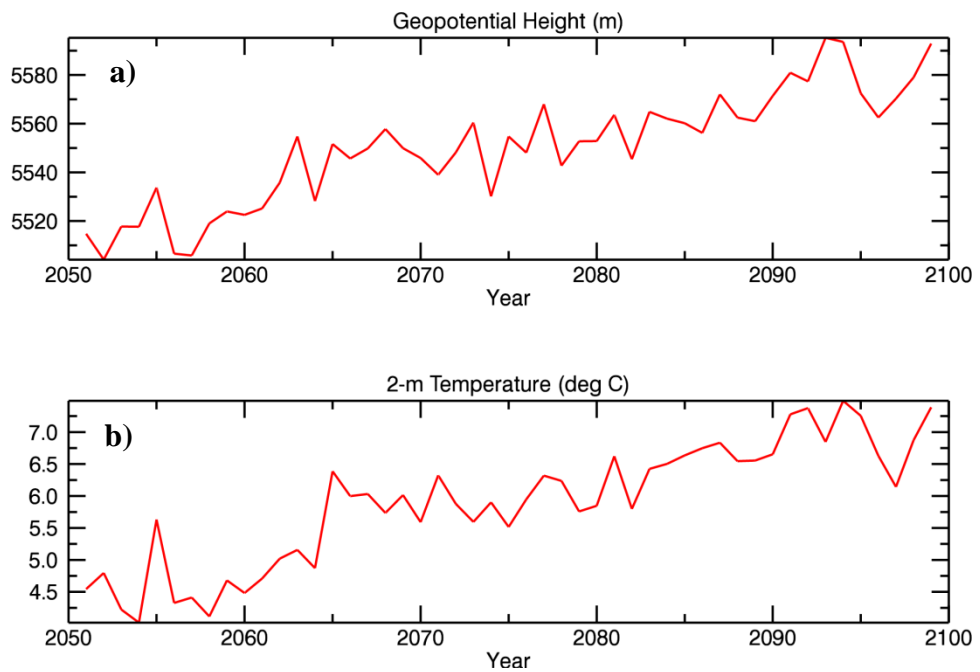


**Figure 2.16** Winter (DJF) a) 500-hPa geopotential heights and b) 2-m temperature averaged over the ECHAM5-RegCM3 domain for the years 2050-2100.

relationship to the changes in temperature throughout the domain and is consistent with changes in soil moisture: PNA+ (PNA-) events lead to widespread decreases (increases) in SWE (Fig. 2.13e and 2.14e). However, while the temperature-SWE relationship holds true in both the present and future climate simulations, the total SWE amounts still decrease under the future scenario, particularly along the coastlines of Alaska and the Pacific Northwest Cascade Mountain range where a lack of precipitation plays the key role (Fig. 2.15e).

## 2.8 Conclusions

The Pacific-North American teleconnection is expressed as a robust pattern in both the ECHAM5 global and RegCM3 regional climate models. We consider the coupling between the NCEP and ECHAM5 GCMs with RegCM3 very successful in that the PNA is resolved in both models with little loss of information between the GCM and RCM. The PNA index time series computed for both the global and regional ECHAM5 simulations are comparable and highly correlated, despite using a 3-point modified index in the RCM calculation. This allows for a high-resolution assessment of climate with an inherent skill comparable to that of the global model used as a forcing.

We find that the value of the PNA index is independent of the two methods used for computation. A three- and four-point modified linear pointwise calculation method revealed very comparable results for both the RegCM3 and ECHAM5 model simulations, suggesting that the PNA index value is influenced most greatly by the

strengths of the Aleutian low and Canadian high, both of which are represented similarly by the regional and global models.

The spatial pattern emerges in ECHAM5 as a leading mode in a rotated-EOF analysis, consistent with the NCEP Reanalysis results, although the strength of the teleconnection as a whole is weaker. The PNA teleconnection is persistent throughout the 21<sup>st</sup> century; however, the spatial orientation of the pressure centers shifts slightly in response to a strengthening of the Aleutian low. This behavior is consistent with the pattern of 500-hPa geopotential heights for these time periods.

The PNA index is highly correlated with North American climate, notably temperature and precipitation. While the strength of the correlations remains the same between the present and future simulations, the location of the maximum shifts in the future run, particularly with precipitation. These correlation patterns are directly related to the positioning of the Aleutian low and Canadian high, the two main drivers of upper-atmospheric circulation in the PNA sector in this study. Positive and negative PNA patterns lead to distinct changes in the anomalies of the five climate variables assessed here. Positive phase patterns show the largest changes, reflecting the deepening of the Aleutian low and the strengthening of the Canadian high leading to a more structured trough-ridge pattern in the future.

## 2.9 Acknowledgements

We acknowledge the IPCC and thank the Max Planck Institute for Meteorology for producing and making available the ECHAM5 20C and A2 model

output. We thank the Oregon State University College of Earth, Ocean, and Atmospheric Sciences Computing Center for assisting with and housing the infrastructure to run our regional model. Funding for this research was provided by the U.S. Geological Survey.

## 2.10 References

- Abatzoglou, J.T. (2010): Influence of the PNA on declining mountain snowpack in the Western United States. *Intl. J. Clim.*, 8 pp.
- Anthes, R., E. Hsie, and Y.-H. Kuo (1987). Description of the Penn State / NCAR Mesoscale Model version 4 (MM4), Technical Report NCAR/TN-282, National Center for Atmospheric Research.
- Barnston, A. G. and R. E. Livezey (1987). Classification, seasonality, and persistence of low-frequency atmospheric circulation patterns. *Mon. Wea. Rev.*, **115**, 1083-1126.
- Coleman, J. S. M. and J. C. Rogers (2003). Ohio River Valley winter moisture conditions associated with the Pacific-North American teleconnection pattern. *J. Climate*. **16**, 969-981.
- Dickinson, R., A. Henderson-Sellers, and P. Kennedy (1993): Biosphere-atmosphere transfer scheme (BATS) version 1e as coupled to the NCAR Community Climate Model, Technical report, National Center for Atmospheric Research.
- Fauria, M. M. and E. A. Johnson (2008). Climate and wildfires in the North American boreal forest. *Phil. Trans. R. Soc. B*, **363**(1501), 2315-2327.
- Feldstein, S. (2000): The timescale, power spectra, and climate noise properties of teleconnection patterns. *J. Climate*, **13**, 4430-4440.
- Giorgi, F. and L.O. Mearns (1999): Introduction to special section: Regional climate modeling revisited. *J. Geophys. Res.*, **104**, 6335–6352.
- Grell, G. (1993): Prognostic evaluation of assumptions used by cumulus parameterizations. *Mon. Wea. Rev.*, **121**, 764–787.

- Hostetler, S., G. Bates, and F. Giorgi (1993): Interactive nesting of a lake thermal model within a regional climate model for climate change studies, *Geophys. Res.* **98**, 5045–5057.
- IPCC (2007): Climate Change 2007: The Physical Science Basis. Contribution of Working Group I to the Fourth Assessment Report of the Intergovernmental Panel on Climate Change [Solomon, S., D. Qin, M. Manning, Z. Chen, M. Marquis, K.B. Averyt, M. Tignor and H.L. Miller (eds.)]. Cambridge University Press, Cambridge, United Kingdom and New York, NY, USA.
- Jungclaus, J.H., M. Botzet, H. Haak, N. Keenlyside, J.-J. Luo, M. Latif, J. Marotzke, U. Mikolajewicz, and E. Roeckner (2005): Ocean circulation and tropical variability in the AOGCM ECHAM5/MPI-OM. *J. Climate*, **19**, 3952-3972.
- Kaiser, H.F. (1958): The varimax criterion for analytic rotation in factor analysis. *Psychometrika*, **23**, 187-200.
- Kalnay, E., M. Kanamitsu, R. Kistler, W. Collins, D. Deaven, L. Gandin, M. Iredell, S. Saha, G. White, J. Woollen, Y. Zhu, A. Leetmaa, B. Reynolds, M. Chelliah, W. Ebisuzaki, W. Higgins, J. Janowiak, K.C. Mo, C. Ropelewski, J. Wang, R. Jenne, and D. Joseph (1996): The NCEP/NCAR 40-year reanalysis project. *Bull. Amer. Met. Soc.*, **77**, 437-471.
- Kawamura, R., M. Sugi, and N. Sato (1995). Interdecadal and interannual variability in the Northern extratropical circulation simulated with the JMA global model. Part I: Wintertime leading mode. *J. Climate*, **8**, 3006-3019.
- Kiehl, J., J. Hack, G. Bonan, B. Boville, B. Breigleb, D. Williamson, and P. Rasch, (1996): Description of the NCAR community climate model (CCSM), Technical Report NCAR/TN-420+STR, National Center for Atmospheric Research.
- Lau, N.-C. (1981). A diagnostic study of recurrent meteorological anomalies appearing in a 15-year simulation with a GFDL general circulation model. *Mon. Wea. Rev.*, **109**, 2287-2311.
- Leathers, D.J., B. Yarnal, M.A. Palecki (1991): The Pacific/North American teleconnection pattern and United States climate. Part I: Regional temperature and precipitation associations. *J. Climate*, **4**, 517-528.

- Leathers, D. J. and M.A. Palecki (1992). The Pacific/North American teleconnection pattern and United States climate. Part II: Temporal characteristics and index specification. *J. Climate*, **5**, 707-716.
- Marsland, S.J., H. Haak, J.H. Jungclaus, M. Latif, and F. Röske (2003): The Max Planck Institute global ocean/sea-ice model with orthogonal curvilinear coordinates. *Ocean. Modell.*, **5**, 91-127.
- Notaro, M., W-C. Wang, and W. Gong (2006). Model and observational analysis of the Northeast U.S. regional climate and its relationship to the PNA and NAO patterns during early winter. *Mon. Wea. Rev.*, **134**, 3479-3505.
- Pal, J., E. Small, and E. Eltahir (2000): Simulation of regional-scale water and energy budgets: Representation of subgrid cloud and precipitation processes within RegCM. *J. Geophys.Res.-Atmos.*, **105**(D24), 29579–29594.
- Rodionov, S. and R. Assel (2001). A new look at the Pacific/North American index. *Geophys. Res. Lett.*, **28**(8), 1519-1522.
- Roeckner, E., G. Bäuml, L. Bonaventura, R. Brokopf, M. Esch, M. Giorgetta, S. Hagemann, I. Kirchner, L. Kornblueh, E. Manzini, A. Rhodin, U. Schlese, U. Schulzweida, and A. Tompkins (2003): The atmospheric general circulation model ECHAM5. Part I: Model description. Max Planck Institute for Meteorology Rep. **349**, 127 pp.
- Wallace, J.M. and D.S. Gutzler (1981): Teleconnections in the geopotential height field during the Northern Hemisphere winter. *Mon. Wea. Rev.*, **109**, 784-812.
- Yu, B. and F.W. Zwiers (2007). The impact of combined ENSO and PDO on the PNA climate: a 1,000-year climate modeling study. *Clim. Dyn.*, **29**, 837-851.

Chapter 3: Analyzing the Pacific-North American teleconnection and its relationship to climate in the CMIP5 models, Part I: Historical simulation

Andrea M. Allan<sup>1</sup> and Steven W. Hostetler<sup>2</sup>

<sup>1</sup>College of Earth, Ocean, and Atmospheric Sciences, Oregon State University,  
Corvallis, Oregon, 97331

<sup>2</sup>U.S. Geological Survey, Oregon State University, Corvallis, Oregon, 97331

### 3.1 Abstract

We assess the presence of the Pacific-North American (PNA) teleconnection pattern in 27 atmosphere-ocean general circulation models (AOGCMs) and earth system models (ESMs) from the fifth phase of the Coupled Model Intercomparison Project (CMIP5). We use the National Centers for Environmental Prediction and Atmospheric Research (NCEP/NCAR) Reanalysis as a quasi-observational baseline in the evaluations of the CMIP5 climate models. We assess the PNA teleconnection both temporally and spatially, using a rotated principle component analysis (RPCA) to extract the PNA index time series and identify the spatial loading patterns. Each model's performance is assessed visually and by employing a series of calculations to quantify the model's spatial structure as compared to NCEP. We also analyze the relationship between the PNA and surface air temperature and precipitation .

The CMIP5 models vary significantly in their ability to simulate different features of the PNA teleconnection. Most models are unable to resolve the temporal variability of NCEP; however, most of the models capture the PNA as a low-frequency oscillation. Spatial discrepancies among the models are not as large as temporal discrepancies, yet nearly all models underestimate the strength of each “center of action”, which are the four centers of high- and low 500-hPa heights over the Northern Hemisphere used to define the PNA. It is also evident that many models lack the ability to simulate the barotropic instability that initiates wave energy propagation through the 500-hPa geopotential height field, leading to a phase-locking and thus indistinguishable positive and negative PNA modes.

### 3.2 Introduction

The Pacific-North American (PNA) teleconnection pattern has long been recognized as a robust feature of Northern Hemisphere atmospheric circulation and more specifically represents the structure of the quasi-stationary wave field over the North Pacific and North America. It is well known that the PNA has strong correlations with wintertime temperatures and precipitation in North America, and these patterns are robust and consistent throughout observations (Wallace and Gutzler, 1981; Leathers et al., 1991). Correlations with precipitation are not as strong as those with temperature, yet still exhibit consistent patterns from December through March (Leathers et al., 1991). While the PNA is robust in nature, few studies have explored its presence in global circulation models (GCMs), and more specifically the ability of these GCMs to capture both the strength and frequency of the PNA teleconnection.

The Pacific-North American pattern is quantified using an index value that typically ranges between  $\pm 3$ . Several methods have been developed to calculate this index, beginning with the linear pointwise method by Wallace and Gutzler (1981), which combines the strength of the 500-hPa geopotential height anomalies at four centers of action throughout the North Pacific and North America. Barnston and Livezey (1987) provide the first comprehensive empirical orthogonal function (EOF) analysis of the Northern Hemisphere teleconnections using interpolated and gridded observed geopotential height data. This method was further refined by rotating the leading EOFs to maximize the variance in the 500-hPa geopotential height fields and highlight the spatial patterns of the teleconnections.

The aim of this study is to analyze the presence, evolution, and climatic influence of the Pacific-North American teleconnection in the most state-of-the-art atmosphere-ocean general circulation models (AOGCMs) and Earth System Models (ESMs) available to date. Thus, the analysis is performed on 27 climate models used in the fifth phase of the Coupled Model Intercomparison Project (CMIP5).

The model output from CMIP5 hopes to provide the climate evaluations necessary to address outstanding questions from Intergovernmental Panel on Climate Change (IPCC) fourth Assessment Report (AR4) to then be included in the Fifth Assessment Report (AR5). The first CMIP5 model output was released to the public domain in February 2011, and the database continues to expand, with an effort to house a complete suite of model runs in time to support the IPCC fifth Assessment Report (AR5) that is scheduled for publication by the end of 2013 (Taylor et al., 2012). The IPCC AR5 report added four new scenarios, representative concentration pathways (RCPs) to the widely-used Special Report on Emissions Scenarios (SRES) that were used in both the third (2001) and fourth (2007) IPCC assessment reports (SRES publication available here: <http://www.ipcc.ch/pdf/special-reports/spm/sres-en.pdf>). The RCPs are intended to be a better representation of the response of the climate system to increasing concentrations of carbon dioxide. The CMIP5 database contains a comprehensive set of output from both AOGCMs and Earth System Models for a variety of past, present, and future modeling experiments, with the future experiments focusing on the new RCP scenarios (Moss et al., 2010).

Section 3.3 explains the models and data used in this study, as well as calculation methods. Section 3.4 presents the results of the temporal, spatial, and climate analyses with a concurrent discussion of these results. Section 3.5 will conclude the findings of the study. Please note that many of the results presented here are for climate “averages” and do not reflect the performance of the CMIP5 models for individual months or years. Additionally, unless otherwise noted, the PNA displayed in all figures and tables is for January, which encompasses variability from the December through February (DJF) winter season.

### 3.3 Model data and calculation methods

#### 3.3.1 AOGCMs and ESMs

Model output for CMIP5 is freely-available for download from the data portal run by the Program for Climate Model Diagnosis and Intercomparison (PCMDI, available at <http://pcmdi3.llnl.gov/esgcet/home.htm>). For this study, we collected output from 27 AOGCM and ESM simulations for two experiments and three atmospheric variables. The number of climate models used was limited by the data available in the portal as of June 1, 2012, as well as the ability to connect to the server and download the necessary datasets for both the “historical” and “RCP85” experiments. We compare these simulations with 50+ years of quasi-observational output from the NCEP/NCAR Reanalysis project (hereafter NCEP). Unless noted otherwise,; Kalnay *et al.*, 1996). NCEP years 1950-2000 are used as the baseline climatology throughout most of this study, unless otherwise noted.

For this study we use the historical experiment, which simulates the long-term past from the mid-19th century through the near-present, as forced by observed atmospheric composition changes. The historical runs include both anthropogenic and natural forcings, dynamic land cover changes, sea ice, and aerosols. The CMIP5 experiment design allows for the inclusion of both AOGCMs and ESMs. While both types of models are fully-coupled between ocean and atmosphere, the ESMs include a biogeochemical carbon cycle that computes carbon fluxes between the ocean, atmosphere, and terrestrial biosphere (Taylor et al., 2012). Information about the models is summarized in Table 3.1.

### 3.3.2 Teleconnection index and pattern calculation methods

The PNA index measures the amplification (positive index) or dampening (negative index) of the quasi-geostrophic upper-level wave field over North America and can be calculated several ways. Wallace and Gutzler (1981) first defined the index with a linear pointwise equation that sums the 500-hPa geopotential height anomalies at four centers of action. This approach was followed by Barnston and Livezey (1987) who used a rotated principle component analysis (RPCA) on these 500-hPa heights to capture the variability of the entire flow field in the Northern Hemisphere. Using the 1950-2000 NCEP 500-hPa output, the National Oceanic and Atmospheric Administration (NOAA) Climate Prediction Center (CPC) has identified correlation coefficients 0.9 and higher between the time series produced by each of these methods, as well as a “modified” pointwise method that attempts to capture the

**Table 3.1** List of descriptive characteristics for the CMIP5 climate models used in the study. Included for each model are its acronym, host institution, atmospheric resolution, vertical levels, the model years acquired from the CMIP5 database, and any applicable references for the model.

Model acronym	Host institution (Country)	Atm Res (lat × lon)	Vertical Levels	Model years	Reference(s)
NCEP	National Centers for Environmental Prediction (United States)	$2.46^\circ \times 2.5^\circ$	17	1948-2011	Kalnay <i>et al.</i> , 1996
ACCESS1-0	CSIRO (Commonwealth Scientific and Industrial Research Organisation), and BOM (Bureau of Meteorology) (Australia)	$1.875^\circ \times 1.25^\circ$	17	1850-2100	Bi <i>et al.</i> , 2012
BCC-CSM1.1	Beijing Climate Center, China Meteorological Administration (China)	$2.81^\circ \times 2.81^\circ$	17	1850-2099	Beijing Climate Center, <a href="http://bcc.cma.gov.cn/en/">http://bcc.cma.gov.cn/en/</a>
BNU-ESM	College of Global Change and Earth System Science, Beijing Normal University (China)	$2.81^\circ \times 2.81^\circ$	17	1850-2100	<a href="http://www.bnu.edu.cn/gces/index-english.html">http://www.bnu.edu.cn/gces/index-english.html</a>
CanESM2	Canadian Centre for Climate Modelling and Analysis (Canada)	$2.81^\circ \times 2.81^\circ$	22	1850-2100	Chylek <i>et al.</i> , 2011
CCSM4	National Center for Atmospheric Research (United States)	$0.9^\circ \times 1.25^\circ$	17	1850-2100	Gent <i>et al.</i> , 2011
CNRM-CM5	Centre National de Recherches Meteorologiques / Centre Europeen de Recherche et Formation Avancees en Calcul Scientifique (France)	$1.5^\circ \times 1.5^\circ$	17	1850-2100	Voldoire <i>et al.</i> , 2011
FGOALS-g2	LASG, Institute of Atmospheric Physics, Chinese Academy of Sciences; and CESS, Tsinghua University (China)	$3.0^\circ \times 2.81^\circ$	17	1900-2100	Yu <i>et al.</i> , 2008
FGOALS-s2	LASG, Institute of Atmospheric Physics, Chinese Academy of Sciences (China)	$1.67^\circ \times 2.81^\circ$	17	1850-2100	Bao <i>et al.</i> , 2010
FIO-ESM	First Institute of Oceanography, SOA (China)	$2.81^\circ \times 2.81^\circ$	17	1850-2100	<a href="http://www.fio.org.cn/english/research%20divisions-1.asp">http://www.fio.org.cn/english/research%20divisions-1.asp</a>
GFDL-CM3	NOAA/Geophysical Fluid Dynamics Laboratory (United States)	$2^\circ \times 2.5^\circ$	23	1860-2100	Donner <i>et al.</i> , 2011
GFDL-ESM2G		$2^\circ \times 2.5^\circ$	17	1861-2100	Dunne <i>et al.</i> , 2012
GFDL-ESM2M		$2^\circ \times 2.5^\circ$	17	1861-2100	
GISS-E2-R	NASA Goddard Institute for Space Studies (United States)	$2^\circ \times 2.5^\circ$	17	1850-2100	<a href="http://data.giss.nasa.gov/modelE/ar5/">http://data.giss.nasa.gov/modelE/ar5/</a>

HadGEM2-AO	National Institute of Meteorological Research/Korea Meteorological Administration (Korea)	$1.25^\circ \times 1.875^\circ$	17	1860-2099	Collins <i>et al.</i> , 2008
HadGEM2-CC	Met Office Hadley Centre (United Kingdom)	$1.2^\circ \times 1.875^\circ$	23	1860-2099	Martin <i>et al.</i> , 2011
HadGEM2-ES		$1.2^\circ \times 1.875^\circ$	17	1860-2100	
INM-CM4	Institute for Numerical Mathematics (Russia)	$1.5^\circ \times 2^\circ$	17	1850-2100	Volodin <i>et al.</i> , 2010
IPSL-CM5A-LR	Institut Pierre-Simon Laplace (France)	$1.875^\circ \times 3.75^\circ$	17	1850-2100	Dufresne <i>et al.</i> , 2012; Hourdin <i>et al.</i> , 2012
IPSL-CM5A-MR		$1.26^\circ \times 2.5^\circ$	17	1850-2100	
IPSL-CM5B-LR		$1.875^\circ \times 3.75^\circ$	17	1850-2100	
MIROC5	Atmosphere and Ocean Research Institute (The University of Tokyo), National Institute for Environmental Studies, and Japan Agency for Marine-Earth Science and Technology (Japan)	$1.4^\circ \times 1.4^\circ$	17	1850-2100	Watanabe <i>et al.</i> , 2010
MIROC-ESM	Atmosphere and Ocean Research Institute (The University of Tokyo), National Institute for Environmental Studies, and Japan Agency for Marine-Earth Science and Technology (Japan)	$2.81^\circ \times 2.81^\circ$	35	1850-2100	Watanabe <i>et al.</i> , 2011
MIROC-ESM-CHEM	$2.81^\circ \times 2.81^\circ$	35	1850-2100		
MPI-ESM-LR	Max Planck Institute for Meteorology (Germany)	$1.875^\circ \times 1.875^\circ$	25	1850-2100	Jungclaus <i>et al.</i> , 2010; Zanchettin <i>et al.</i> , 2011
MPI-ESM-MR		$1.875^\circ \times 1.875^\circ$	25	1850-2100	
MRI-CGCM3	Meteorological Research Institute (Japan)	$1.125^\circ \times 1.125^\circ$	23	1850-2100	Kitoh <i>et al.</i> , 2007
NorESM1-M	Norwegian Climate Centre (Norway)	$1.875^\circ \times 2.5^\circ$	17	1850-2100	Otterå <i>et al.</i> , 2011

spatial variability mentioned above without requiring a full RPCA (CPC, 2005). We were able to reproduce the time series of CPC's PNA index with the NCEP output to a high degree of agreement for both the modified linear pointwise method ( $r = 0.99$ ) and the RPCA method ( $r = 0.95$ ). Additionally, we also found a high correlation ( $r = 0.95$ ) between the time series calculated using the modified pointwise method and the RPCA. Both the pointwise and RPCA time series will be used in this study for different applications. The RPCA method will be used for the bulk of the analyses, as it is the preferred method by the CPC and we believe this method produces more realistic results because it accounts for height variability in the entire Northern Hemisphere. The modified linear pointwise method is a more straightforward calculation and is less ambiguous during the summer months when the PNA pattern is weaker and more obscure. Thus, the modified linear pointwise method will be used where a monthly index value is needed for the entire annual cycle.

Using the RPCA, the identification of the spatial pattern of the PNA is concurrent with the calculation of the time series, as described by the CPC (2008): the spatial pattern emerges as the rotated empirical orthogonal functions (rEOF) and the indices are the principle component time series associated with the rEOFs. The RPCA uses a 3-month standardized 500-hPa geopotential height anomaly field to calculate each monthly pattern. The PNA is most prominent in the winter; we therefore focus on the January spatial pattern, which encompasses the height field from the December through February (DJF) winter season. The PNA spatial patterns are displayed as “loading patterns” that quantify the temporal correlation between the original

standardized 500-hPa height anomaly field and the RPCA-based index time series at each grid point.

### 3.4 Results and Discussion

#### 3.4.1 Temporal variability

The association of the positive- and negative-phase PNA events with NCEP is not expected to coincide because the CMIP5 models attempt to simulate long-term climate averages, rather than replicate real-world events. The temporal variability of the PNA index for each model is therefore assessed based on the amplitude and frequency, rather than individual positive and negative events. The amplitudes of the PNA indices in the CMIP5 models is comparable to NCEP with positive and negative events ranging between  $\pm 3$ ; however, both the frequency and the duration of the positive and negative events varies substantially (Fig. 3.1). To quantify these differences, we computed the index means, standard deviations, and positive-to-negative ratios (Table 3.2). The ratio is simply the cumulative area above and below zero, multiplied the ratio by the fractional years in each total. This value quantifies the differences between the number of positive and negative events in each index time series. The mean and ratio for NCEP is  $-0.649 \pm 1.296$  and 0.162, respectively indicating that the PNA is in a negative phase  $\sim 6$  times as often as it is positive in a positive phase. The all-model mean is 0.005 and most of the models have ratios between 0.5 and 1.5 suggesting a more balanced oscillation between positive and negative modes. Zero CMIP5 models meet or exceed the 0.162 NCEP ratio suggests

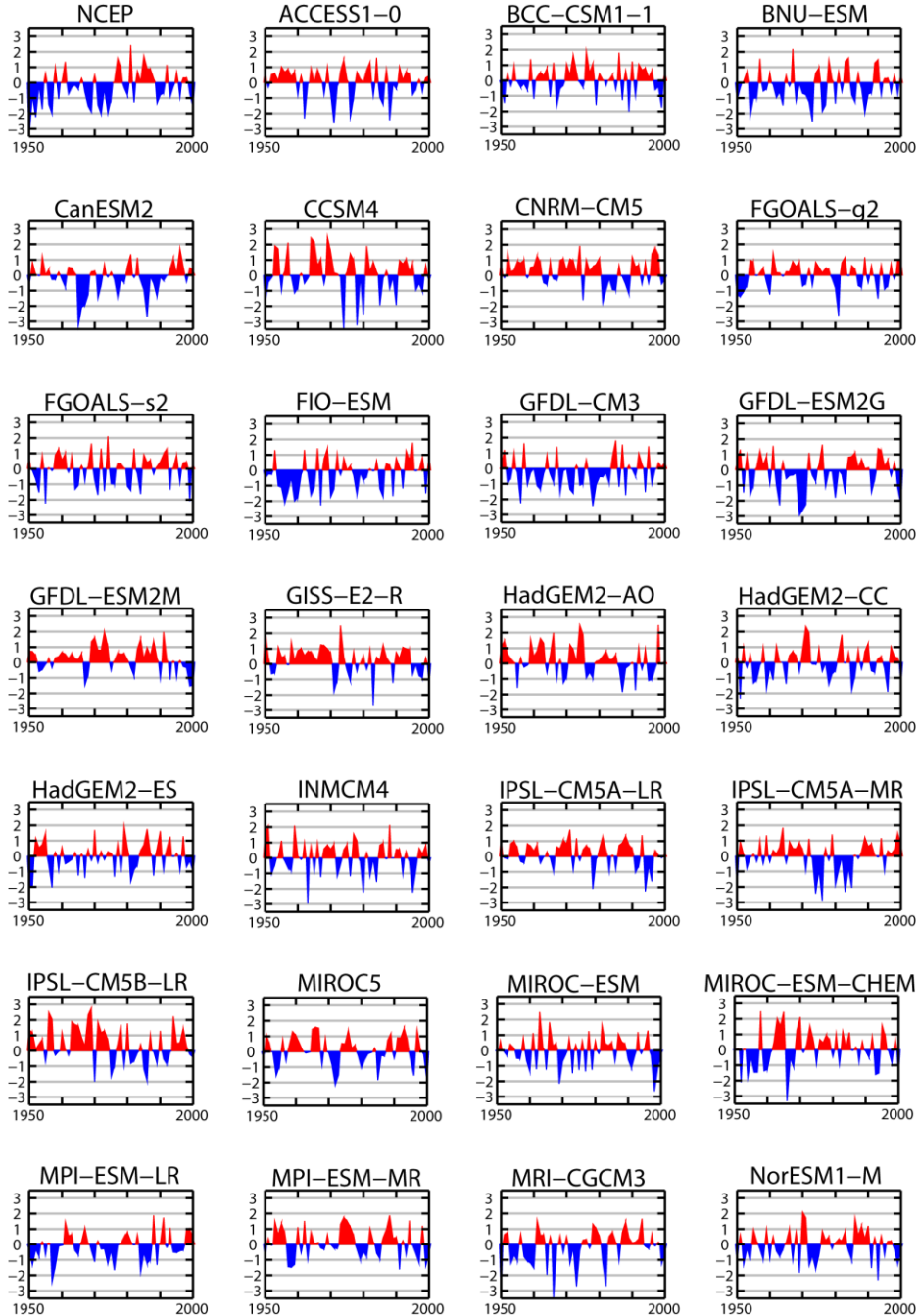


**Figure 3.1** Pacific-North American time series for January 1950-2000, calculated using the RPCA method. Shaded red regions indicate positive modes and shaded blue areas indicate negative modes.

**Table 3.2** The mean, standard deviation, and positive-to-negative index area ratio for NCEP and each CMIP5 model. The CMIP5 model means for each column are displayed in the last row.

MODEL	Mean	Std Dev	+/- Ratio
NCEP	-0.649	1.296	0.162
ACCESS1-0	0.028	0.993	1.813
BCC-CSM1.1	0.058	0.951	1.413
BNU-ESM	-0.241	1.077	0.379
CanESM2	-0.193	0.978	0.464
CCSM4	0.084	1.382	1.327
CNRM-CM5	0.322	0.870	3.990
FGOALS-g2	0.009	0.841	1.252
FGOALS-s2	-0.052	1.040	1.168
FIO-ESM	-0.274	1.078	0.374
GFDL-CM3	-0.275	1.022	0.280
GFDL-ESM2G	-0.224	1.163	0.545
GFDL-ESM2M	0.217	0.839	4.160
GISS-E2-R	0.263	0.967	4.284
HadGEM2-AO	0.219	1.030	2.678
HadGEM2-CC	-0.047	1.028	0.792
HadGEM2-ES	-0.065	1.018	0.889
INM-CM4	0.059	1.116	1.287
IPSL-CM5A-LR	0.167	0.868	2.495
IPSL-CM5A-MR	-0.028	1.073	1.230
IPSL-CM5B-LR	0.457	1.193	4.011
MIROC5	0.078	0.980	1.267
MIROC-ESM	-0.044	1.040	0.863
MIROC-ESM-CHEM	0.020	1.257	1.082
MPI-ESM-LR	-0.162	0.898	0.436
MPI-ESM-MR	0.109	0.963	1.365
MRI-CGCM3	-0.269	1.293	0.578
NorESM1-M	-0.082	0.982	0.849
<b>MODEL MEAN</b>	<b>0.005</b>	<b>1.035</b>	<b>1.529</b>

that the models fail to produce a strong enough low over the North Pacific. The Aleutian low is the dominant PNA center of action; thus, if this pressure center is too weak the model fails to produce the atmospheric circulation necessary for strong positive PNA events. The ratios for GFDL-CM3, FIO-ESM, and BNU-ESM are closest to NCEP with values of 0.280, 0.374, and 0.379 respectively. Whereas NCEP is dominated by negative PNA events, several models are dominated by positive events, as evidenced by positive index phase-locking for up to a decade or more and ratios well above 3.5 (CNRM-CM5, GFDL-ESM2M, and GISS-E2-R).

The 12-month smoothed power spectra for all models using the unsmoothed monthly PNA index time series for the years 1950-2000 are shown in Figure 3.2. The time series are calculated using the modified linear pointwise method, because monthly index values are necessary to resolve frequencies shorter than one year. The spectra produced by all models display generally similar “red” patterns. Red noise spectra are typical of atmospheric index time series, as the spectra measures the amount of relative variance (or power) of the time series at varying frequencies and these time series tend to exhibit more variance at low frequencies and less variance at high frequencies (Gilman et al., 1962). Gilman also states that time series with the removal of pre-determined periodicities are considered “pre-whitened”; seasonal or diurnal cycles, such as those in temperature data, are considered periodic and contribute to white noise in a spectral analysis. Thus, removing these cycles allows for

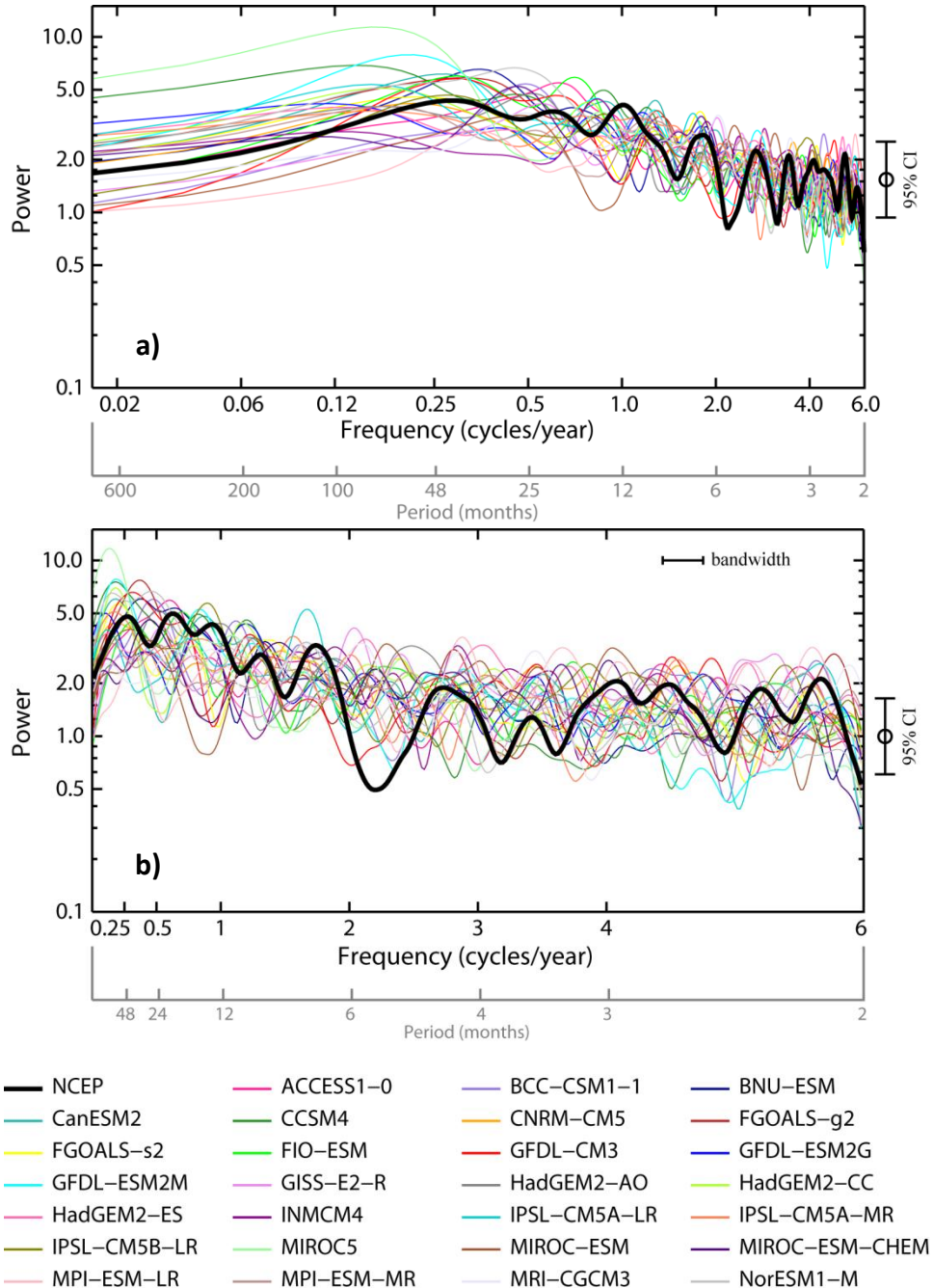


**Figure 3.2** The 12-month smoothed power spectra for all models using the unsmoothed monthly PNA index time series for the years 1950-2000. The power spectra are shown in a) log-power/log-frequency space and b) log-power space. The 95% confidence interval is shown on both plots and the bandwidth is shown on (b). Time scales are displayed in both frequency and period.

any non-periodic spectral peaks to emerge more clearly. The NCEP spectrum shows relative peaks at 3, 4, 7, 12- 24, and 36-48 months, indicating both a seasonal fluctuation in the PNA structure and a longer 3-4 year cycle that may be related to forcing by ENSO. The CPC states that positive (negative) phase PNA events are often associated with warm (cold) phase ENSO events.

The CMIP5 models appear to have very little coherence with NCEP; however, a cross-correlation analysis reveals that 22 models have cross-correlation coefficients  $>0.5$  with the NCEP spectrum at lag zero, with four of the models having correlations  $>0.7$  (Fig. 3.3a; ACCESS1-0, CCSM4, GFDL-ESM2M, and NorESM1-M). Additionally, the spectra of these four models show a seasonal power at 3-4 months with most of the power concentrated at low frequencies of 3-4 years, which is in agreement with NCEP (Fig. 3.3b).

### 3.4.2 Spatial variability

The Pacific-North American teleconnection is characterized by a distinct arrangement of four “centers” situated over the North Pacific Ocean and North America. The CPC defines the PNA as the second leading mode of variability in a rotated empirical orthogonal function (rEOF) analysis of the monthly mean 500-hPa geopotential height anomaly field (Fig. 3.4). In the positive phase shown in the map, positive height anomalies are located over both the subtropics and Western Canada, and negative height anomalies are located over the region of Aleutian low in the North Pacific and the far southeast United States. The negative phase is characterized by

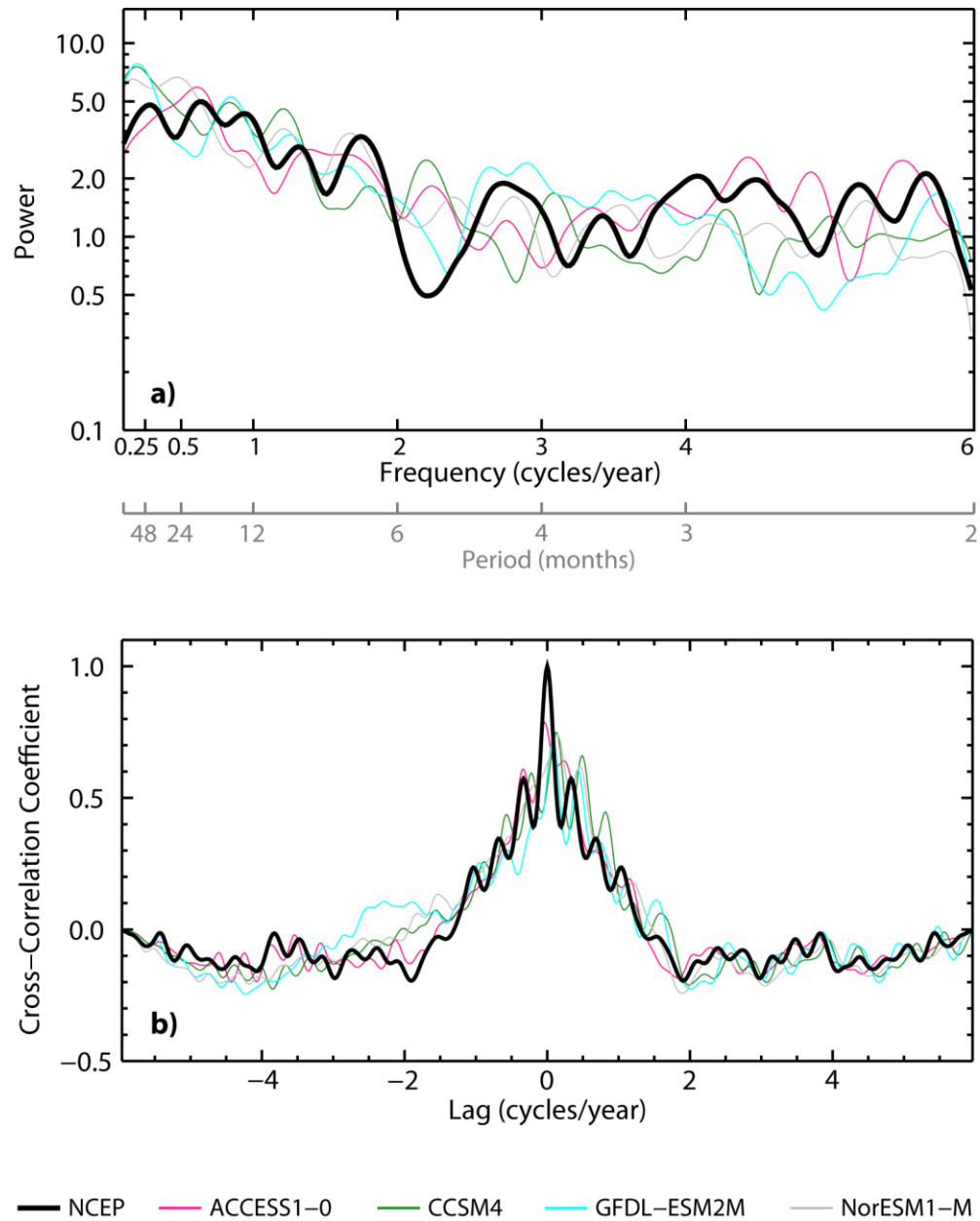


**Figure 3.3** a) The 12-month smoothed power spectra for 1950–2000, as in Fig. 2, and b) the cross-correlation analysis between NCEP and the four CMIP5 models with zero-lag cross-correlation coefficients  $>0.7$ .

opposite signs of the anomalies at each center. Here we focus on three of these four points, omitting the center over the subtropics. Previous studies have shown that analyzing the three remaining centers provides more explanatory power with regard to wave energy propagation over North America, and that including the subtropical center when calculating a pointwise index can actually lead to biases if variability of the PNA is a result of anomalies in the East Asian jet (Leathers et al., 1991). Additionally, the CPC notes that the shift from positive to negative PNA phases is directly related to the eastward or westward shift of the exit region of the East Asian jet, further supporting our choice to exclude the subtropical center. The three centers, hereafter referred to as P1, P2, and P3 as indicated in Figure 3.5, will be used to assess the spatial patterns of PNA in the CMIP5 models.

Although the PNA pattern does not appear as the second leading mode for all CMIP5 models, it is present as one of the ten leading modes that are used in the RPCA described in Section 3.3.2 (exact mode varies for each model, see Table 3.3). A substantial amount of variability exists in the loading patterns associated with the PNA for all CMIP5 models both compared to NCEP to each other (Fig. 3.5). The spatial distribution of the centers in the CMIP5 models around the NCEP centers displays substantial spread (Fig. 3.6). The distribution around P1 exhibits the an east-west extent of  $\sim 35^\circ$  in longitude, whereas around P2 and P3 the models span  $\sim 45^\circ$  and  $\sim 50^\circ$  degrees, respectively. The  $\sim 20^\circ$  north-south spread of the models around P3 is the smallest latitudinal extent, followed by  $\sim 25^\circ$  in P1 and over  $40^\circ$  in P2. The location of each center relative to NCEP varies for each model; however, a poor performance for

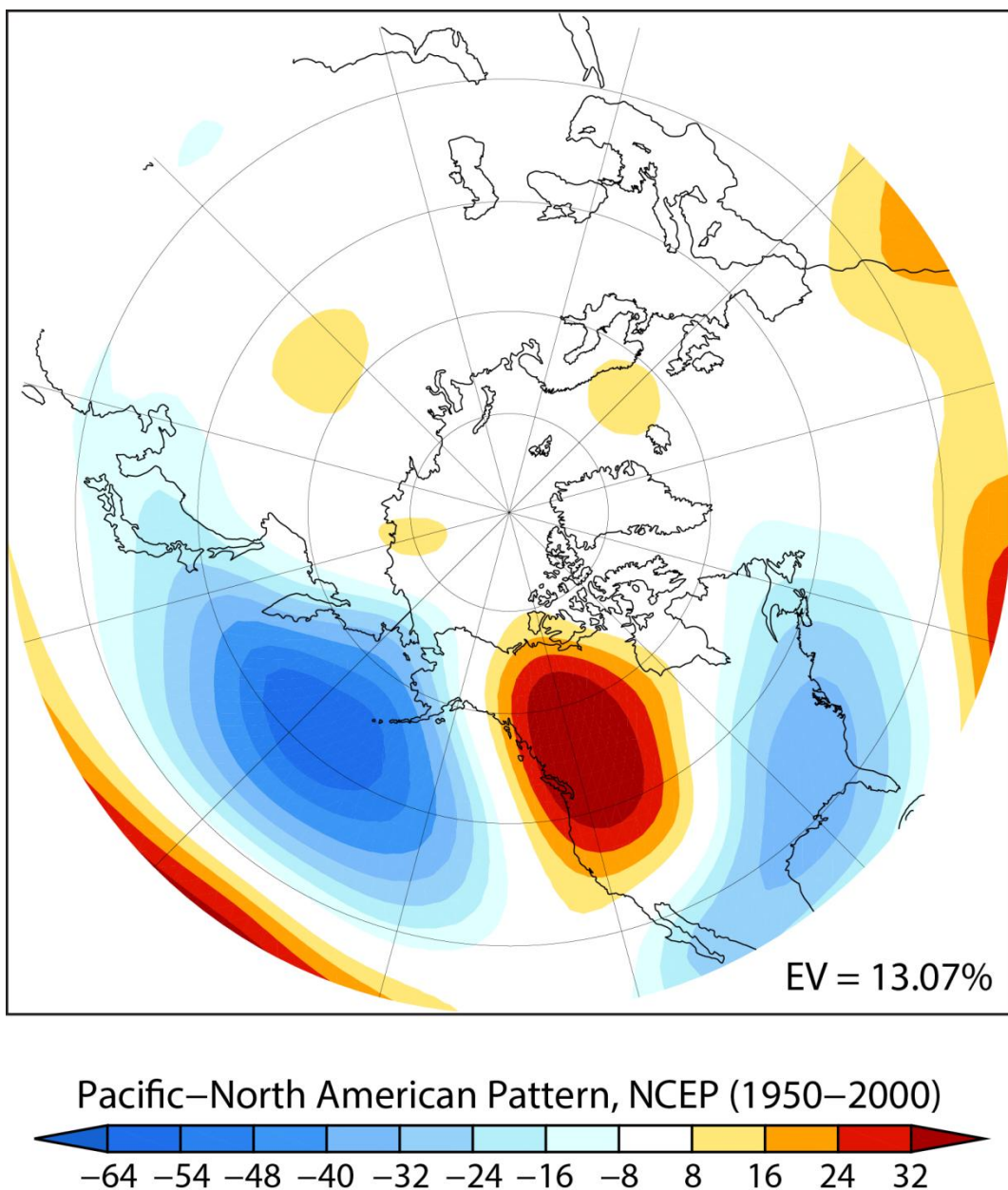


**Figure 3.4** The January Pacific–North American pattern as shown by the second leading mode of a rotated-EOF analysis on monthly standardized 500-hPa geopotential height anomalies. The amount of explained variance is displayed in the lower right corner.

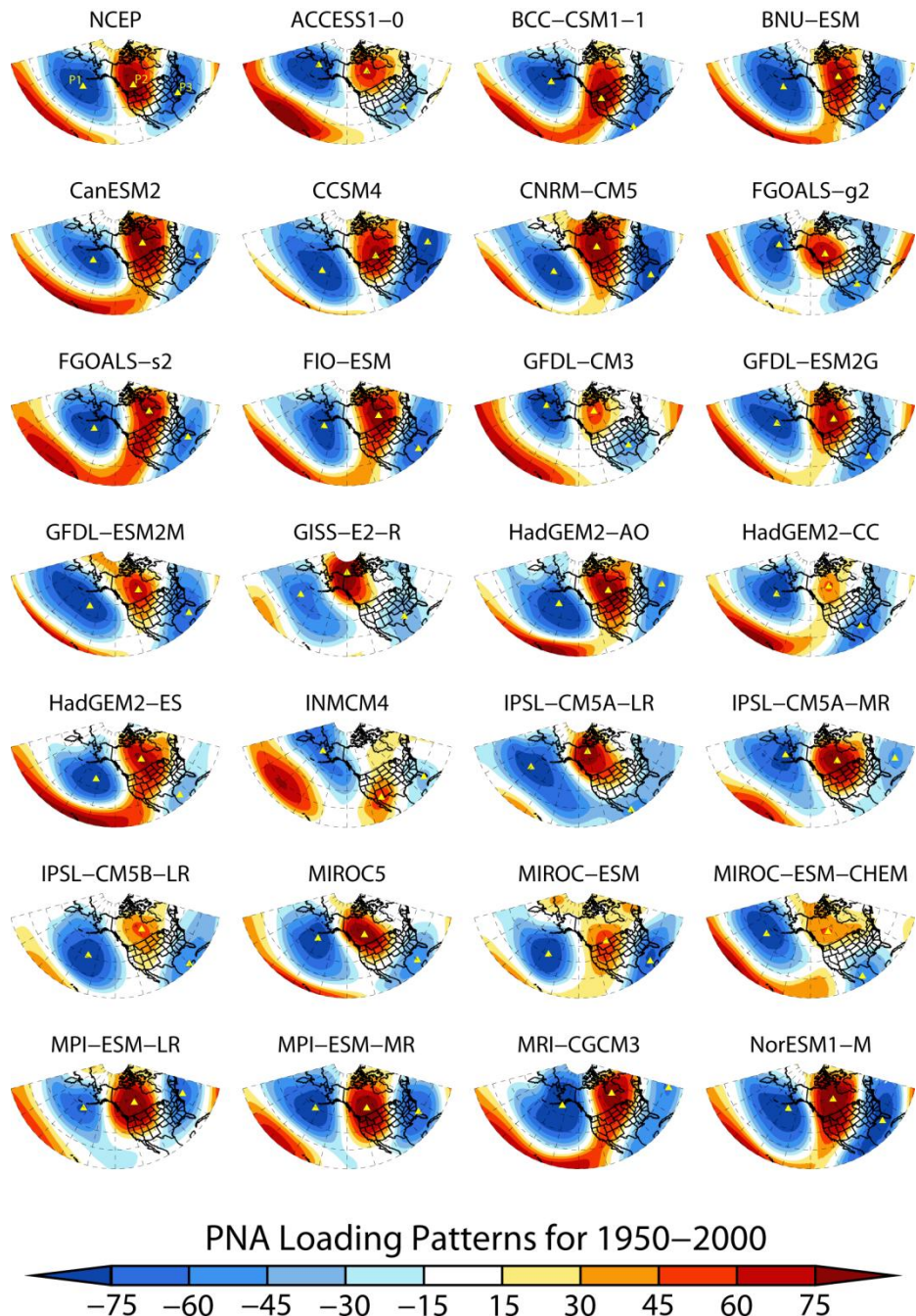


**Figure 3.5** The loading patterns associated with the PNA for NCEP and all CMIP5 models for the years 1950–2000. The values represent the temporal correlation ( $R^2 \times 100$ ) between the 500-hPa standardized geopotential height anomalies and the PNA index for the month of January relative to the DJF winter season. The centers P1, P2, and P3 labeled on the NCEP map are indicated by yellow triangles on the rest of the maps.

**Table 3.3** The rotated-EOF mode and explained variance associated with the PNA teleconnection pattern for each model.

MODEL	Mode	EV (%)
NCEP	2	13.07
ACCESS1-0	2	13.08
BCC-CSM1.1	3	9.34
BNU-ESM	2	10.68
CanESM2	2	12.64
CCSM4	3	9.92
CNRM-CM5	2	12.35
FGOALS-g2	4	7.53
FGOALS-s2	3	10.38
FIO-ESM	2	10.66
GFDL-CM3	6	4.69
GFDL-ESM2G	10	2.87
GFDL-ESM2M	4	8.23
GISS-E2-R	7	4.12
HadGEM2-AO	8	3.73
HadGEM2-CC	4	7.54
HadGEM2-ES	10	3.05
INM-CM4	10	3.07
IPSL-CM5A-LR	3	9.43
IPSL-CM5A-MR	2	10.63
IPSL-CM5B-LR	9	3.78
MIROC5	6	5.82
MIROC-ESM	3	9.51
MIROC-ESM-CHEM	6	5.55
MPI-ESM-LR	2	9.66
MPI-ESM-MR	2	11.80
MRI-CGCM3	2	11.79
NorESM1-M	2	11.69

one center does not necessarily mean a poor performance at the other two centers (e.g., GISS-E2-R, INMCM4, and BCC-CM1-1). MPI-ESM-MR appears to be the most accurate at all three centers, falling within a few degrees of each NCEP center.

In order to quantify the spread of the models relative to NCEP we computed the coordinate distance from each NCEP center to each model's respective center. We then used the model's  $\Delta\text{lon}$  and  $\Delta\text{lat}$  values for P1, P2 and P3 and averaged the three vector magnitudes to arrive at an "average distance" from NCEP (Table 3.4). Smaller average distance values imply that the model is more accurate at reproducing the spatial PNA pattern relative to NCEP. We then ranked the models from lowest to highest average distance. Based on these calculations 10 models fall within a 10-degree average distance from NCEP, with MPI-ESM-MR and MIROC5 both averaging less than 5 degrees different. MRI-CGCM3 is the least accurate with an average distance of about 22 degrees. Using these average distances is just one way of assessing PNA reproducibility in the models; a model with a large average distance can still produce an accurate PNA pattern if the juxtaposition of the three centers is accurate. We explore this possibility in a later section.

The strength of the centers relative to NCEP is assessed by projecting the PNA index time series for each model back onto the 500-hPa geopotential height anomaly field used to calculate the index (Fig. 3.7). A majority of the models underestimate the strength of the centers, particularly P3 in the southeast United States (Table 3.5). With the exception of CCSM4 and MRI-CGCM3, the average anomaly differences are negative implying that most of the CMIP5 models generally underestimate the

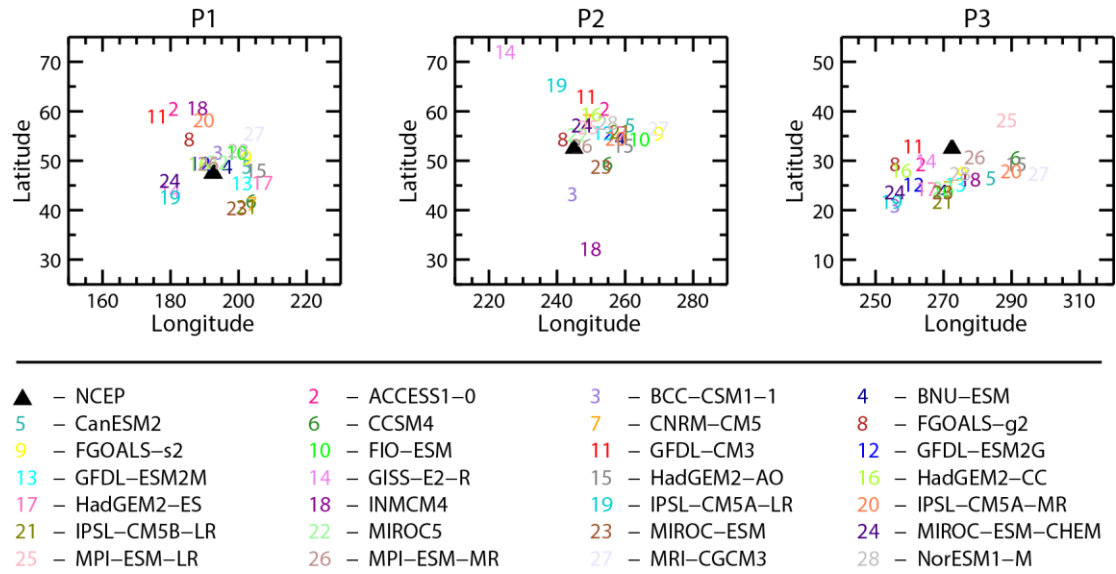


**Figure 3.6** The spatial distribution of each center P1, P2, and P3 for each model (color-coded numbers) with respect to NCEP (black triangle).

**Table 3.4** The longitudinal ( $\Delta\text{lon}$ ) and latitudinal ( $\Delta\text{lat}$ ) distance from NCEP for P1, P2, and P3 in degrees for each CMIP5 model (differences calculated as (model – NCEP)). The values displayed for NCEP are the actual longitude and latitude coordinates for each center. The vector distances for each center were calculated and used to compute an “average distance” from NCEP. The ranking is based on the average distance.

Model	P1		P2		P3		Average Distance	Rank
	$\Delta\text{lon}$	$\Delta\text{lat}$	$\Delta\text{lon}$	$\Delta\text{lat}$	$\Delta\text{lon}$	$\Delta\text{lat}$		
NCEP	<b>192.50</b>	<b>47.50</b>	<b>245.00</b>	<b>52.50</b>	<b>272.50</b>	<b>32.50</b>		--
ACCESS1-0	-11.56	13.13	9.06	8.13	-9.06	-3.13	13.08	17
BCC-CSM1.1	1.56	4.13	-0.31	-9.25	-16.56	-11.57	11.29	12
BNU-ESM	4.38	1.34	13.75	1.92	-2.50	-8.78	9.20	7
CanESM2	10.00	1.34	16.56	4.71	11.56	-5.99	13.44	18
CCSM4	11.25	-5.56	10.00	-3.02	18.75	-1.87	13.95	20
CNRM-CM5	11.41	-6.18	3.91	5.63	-1.09	-7.99	9.30	8
FGOALS-g2	-6.88	6.92	-3.13	1.92	-16.56	-3.20	10.10	11
FGOALS-s2	10.00	3.10	25.00	3.08	3.13	-5.13	13.89	19
FIO-ESM	7.19	4.13	19.38	1.92	-2.50	-8.78	12.30	14
GFDL-CM3	-16.25	11.50	3.75	10.50	-11.25	0.50	14.11	22
GFDL-ESM2G	-3.75	2.05	8.75	3.12	-11.25	-7.22	8.98	6
GFDL-ESM2M	8.75	-1.99	8.75	3.12	1.25	-7.22	8.53	3
GISS-E2-R	-12.50	-3.50	-20.00	19.50	-7.50	-2.50	16.27	26
HadGEM2-AO	12.81	0.63	14.69	0.63	19.06	-3.13	15.62	24
HadGEM2-CC	-4.06	1.88	5.31	6.88	-14.69	-4.38	9.50	10
HadGEM2-ES	14.69	-1.88	12.81	3.13	-7.19	-8.13	12.95	16
INM-CM4 *	-4.50	13.25	5.00	-20.25	5.50	-6.25	14.39	23
IPSL-CM5A-LR	-12.50	-4.87	-5.00	12.87	-17.50	-10.71	15.91	25
IPSL-CM5A-MR	-2.50	10.81	12.50	2.01	17.50	-4.61	13.95	21
IPSL-CM5B-LR	10.00	-6.76	13.75	3.39	-2.50	-10.71	12.41	15
MIROC5	1.56	2.23	1.09	2.83	-2.50	-7.99	4.71	2
MIROC-ESM	7.19	-7.04	8.13	-3.66	-2.50	-8.78	9.37	9
MIROC-ESM-CHEM	-12.50	-1.46	2.50	4.71	-16.56	-8.78	12.22	13
MPI-ESM-LR	-1.25	1.93	4.38	4.39	16.25	5.74	8.58	5
MPI-ESM-MR	-1.25	1.93	2.50	0.66	6.88	-1.72	3.99	1
MRI-CGCM3	12.25	8.01	25.00	4.14	25.63	-5.02	22.03	27
NorESM1-M	7.50	4.61	10.00	5.29	2.50	-5.03	8.58	4
All-model mean	<b>1.75</b>	<b>1.55</b>	<b>7.81</b>	<b>3.79</b>	<b>-0.74</b>	<b>-5.62</b>	<b>11.70</b>	--

\* INM-CM4 is not included in the all-model means.

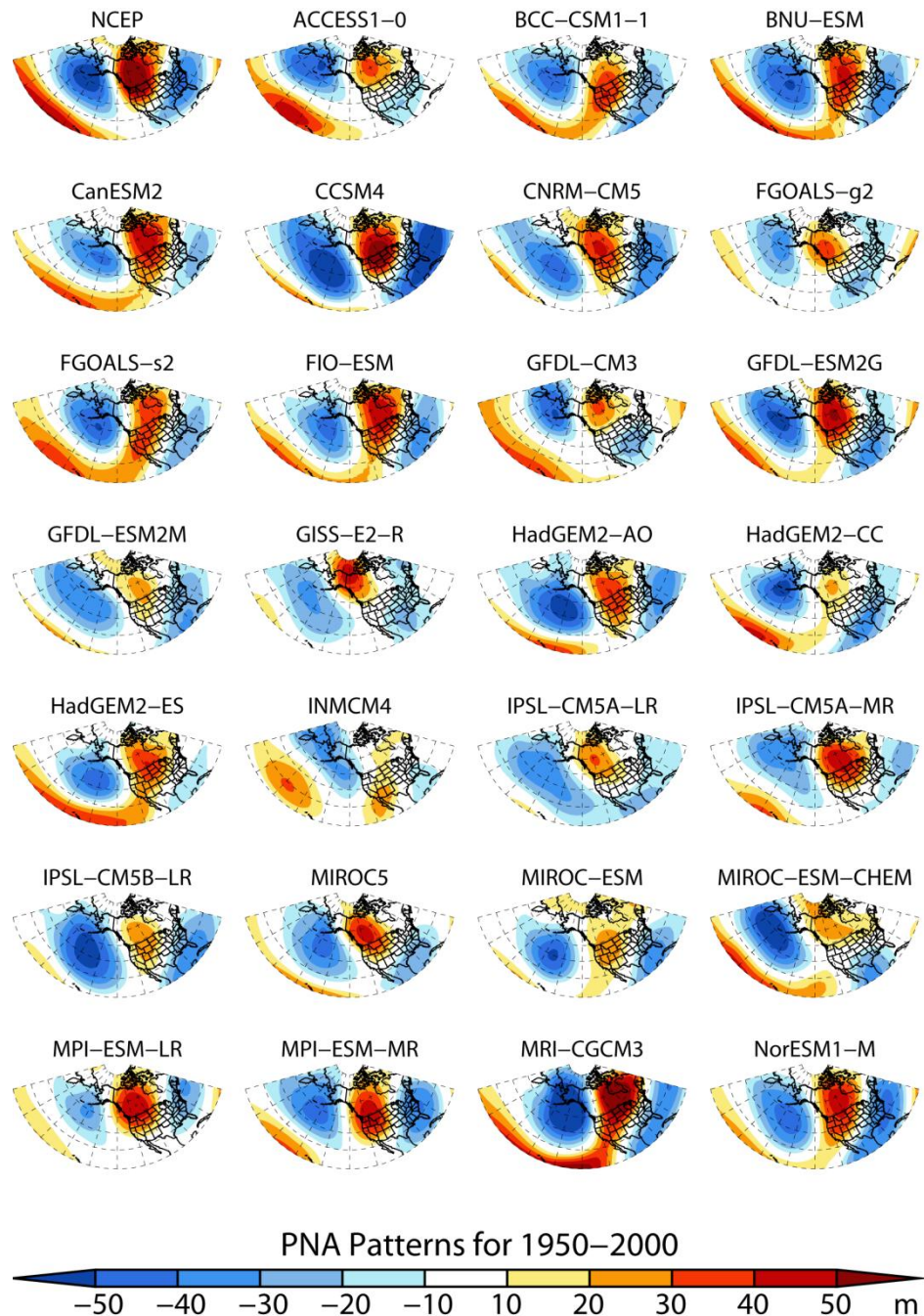


**Figure 3.7** The PNA teleconnection loading pattern as defined by projecting the time series of the PNA index for each model back onto the 500-hPa geopotential height anomaly field used to calculate the index for all Januaries from 1950-2000. The January anomalies are relative to the DJF winter season. The values displayed are in meters and represent the magnitude of the anomalies associated with the PNA pattern at each grid point.

**Table 3.5** The P1, P2, and P3 center anomaly differences, in meters, between the CMIP5 models and NCEP for the Historical time period (calculated as (CMIP5 minus NCEP)). The values are calculated using the absolute values of the center anomalies so that the magnitude of the differences are respective to zero; a negative (positive) difference corresponds to a weaker (stronger) absolute anomaly (i.e., at P1, a difference of -8.81 m for ACCESS1-0 with respect to the NCEP anomaly of -60.29 m indicates that the magnitude of the ACCESS1-0 anomaly center, -51.48 m, is weaker than NCEP's). The ranking displayed is based on the absolute value of the average difference.

MODEL	P1	P2	P3	Average Difference	Rank
NCEP	<b>-60.29</b>	<b>65.34</b>	<b>-41.78</b>	--	--
ACCESS1-0	-8.81	-30.86	-21.17	-20.28	20
BCC-CSM1.1	-13.80	-24.61	-8.89	-15.77	13
BNU-ESM	-9.36	-21.60	-6.60	-12.52	7
CanESM2	-17.26	-16.00	-16.95	-16.74	15
CCSM4	3.33	-4.13	22.69	7.30	1
CNRM-CM5	-15.71	-22.92	-2.26	-13.63	9
FGOALS-g2	-24.07	-31.29	-19.33	-24.90	26
FGOALS-s2	-9.57	-26.15	-11.97	-15.90	14
FIO-ESM	-14.56	-15.82	-8.14	-12.84	8
GFDL-CM3	-8.76	-31.02	-12.17	-17.32	17
GFDL-ESM2G	-6.70	-13.63	-4.52	-8.29	3
GFDL-ESM2M	-20.11	-39.26	-9.83	-23.07	24
GISS-E2-R	-27.82	-18.47	-18.01	-21.43	23
HadGEM2-AO	-4.25	-25.16	-3.76	-11.06	4
HadGEM2-CC	-5.21	-42.31	-5.53	-17.68	18
HadGEM2-ES	-14.16	-24.68	-23.52	-20.79	22
INM-CM4	-25.09	-39.32	-25.19	-29.86	27
IPSL-CM5A-LR	-22.76	-34.26	-16.85	-24.62	25
IPSL-CM5A-MR	-24.11	-19.35	-18.02	-20.49	21
IPSL-CM5B-LR	-4.53	-36.72	-2.75	-14.67	11
MIROC5	-13.51	-20.17	-12.16	-15.28	12
MIROC-ESM	-8.59	-37.78	-5.24	-17.20	16
MIROC-ESM-CHEM	3.94	-40.36	-6.09	-14.17	10
MPI-ESM-LR	-27.97	-15.16	-10.14	-17.76	19
MPI-ESM-MR	-14.45	-18.30	-0.74	-11.16	6
MRI-CGCM3	20.41	2.86	-0.85	7.47	2
NorESM1-M	-15.08	-19.26	0.92	-11.14	5
All-model mean	<b>-11.67</b>	<b>-24.09</b>	<b>-8.53</b>	<b>-14.77</b>	--

magnitude of the geopotential height anomalies associated with the PNA teleconnection. P2 is the most misrepresented with half of the models underestimating the anomaly more than 25 meters, which, on average is 40% lower than NCEP. Positive PNA patterns are associated with barotropic instability, and are characterized by a trough over the North Pacific (Aleutian low) and a ridge over Canada (Wallace and Gutzler, 1981). Thus, weak anomalies in the P2 region can be attributed to either or both: (a) the inability of a model to adequately simulate the oscillation, or “see-saw”, between meridional (blocking) and zonal flows, resulting in the flow being locked into one mode; (b) the simulated ridge is either too weak or the model is unable to simulate a blocking ridge altogether.

To illustrate the flow associated with the PNA for each model we made composite spaghetti plots of three different geopotential height levels, or “isohypsuses”, on the 500-hPa pressure surface during both positive and negative PNA years (indices greater/less than  $+/-0.5$ ) (Figure 3.8). The convergence of the isohypsuses at the far western edge of the PNA sector represent the flow associated with the exit East Asian jet. As the air makes its way toward the west coast of North America, discrepancies between models arise around the Aleutian low and continue across North America. The shift between meridional (positive PNA) and zonal (negative PNA) flows is clearly evident in NCEP (thick black line), especially for the 5280-m isohypse. Most models demonstrate the ability to reproduce a ridge-like feature in the 500-hPa flow during the positive mode; however, few shift to a zonal flow during negative phases. Isohypses for individual model illustrate more clearly the ability of each model to

capture the shift in flow patterns between positive and negative modes (Fig. 3.9). As NCEP illustrates, the structure of the wave pattern translates throughout all three contours, most noticeably in the 5280-m isohypse. As in Figure 3.8, several models appear locked in a blocking pattern during both positive and negative modes (e.g., GFDL-CM3 and all three IPSL models). On the other hand, ACCESS1-0 and FGOALS-g2 display a flow shift on one surface, but not on another, evident of a P1 center that is too weak and/or too far north. About one-third of the produce the shift in flow on some level and therefore simulate distinct positive and negative PNA patterns.

### 3.4.3 Model performance

The flow patterns and spatial structures associated with the PNA pattern varies widely among the CMIP5 models. While a visible assessment of model performance is easily achievable, quantifying the differences among the models and comparing their performance to NCEP are more difficult due to the competing influences of both center location and height anomaly strength.

The successful representation of the PNA within a climate model largely depends on its ability to reproduce the see-saw between meridional and zonal flows. The spatial variability in the western half of the PNA sector is attributed both to the latitudinal separation between P1 and P2 and the difference in magnitude of P1 and P2. In NCEP P1 and P2 are located within  $5^{\circ}$  latitude of each other and relatively close in magnitude (refer to Tables 3.4 and 3.5). If the latitudinal difference between P1 and P2 that is too large, the blocking wave structure will be over amplified during

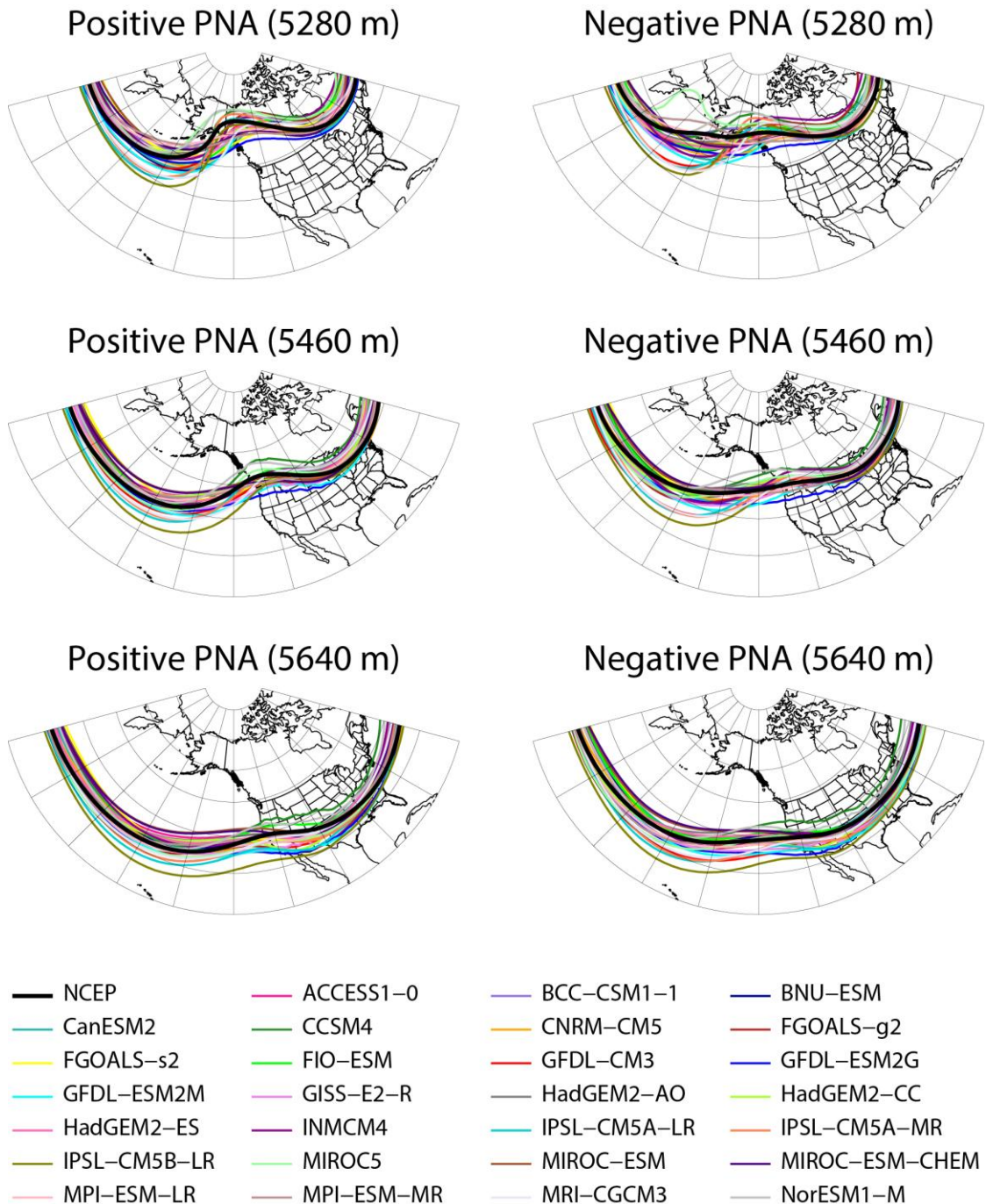


**Figure 3.8** Composite spaghetti plots of three different isohypes – 5280 m, 5460 m, and 5640 m – on the 500-hPa pressure surface during both positive (indices greater than 0.5) and negative (indices less than -0.5) PNA years. Each model is represented with a different color and NCEP is the thick black contour.

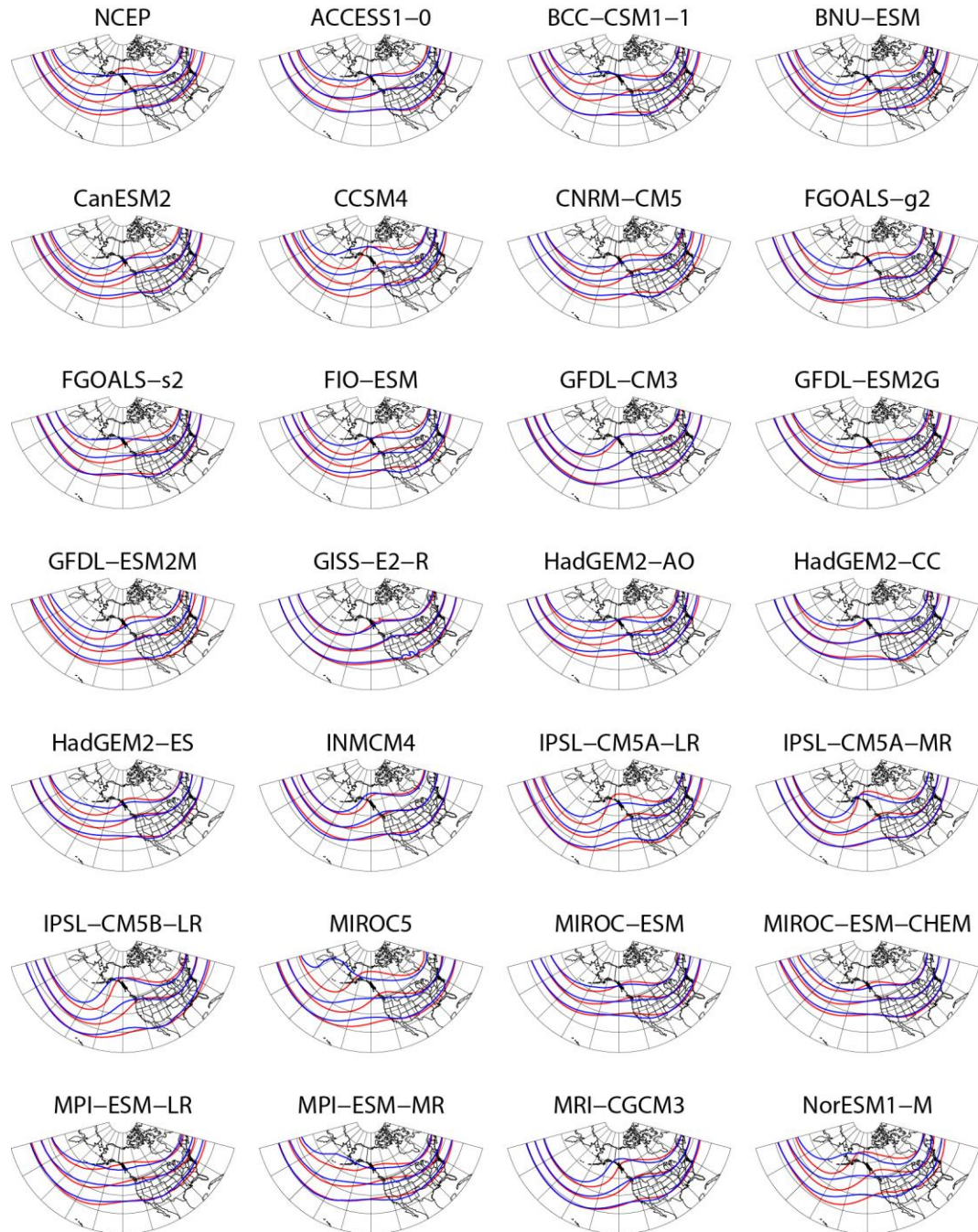


**Figure 3.9** 500-hPa isohypes for positive (greater than 0.5; red lines) and negative (less than -0.5; blue lines) PNA indices. The northernmost contours are for the 5280-m isohypse, the middle contours are for the 5460 m isohypse, and the southernmost contours are for the 5640 m isohypse.

positive phases and the flow will be too meridional during negative phases. On the other hand, a discrepancy between the strengths of P1 and P2, which usually is associated with  $P1 > P2$ , leads to a dampening of the wave structure and decreased meridional flow. We compute a simple “see-saw index” (SSI) to combine and quantify these P1-P2 differences:

$$\begin{aligned} SSI &= D_{model} - D_{NCEP}, \text{ where} \\ D &= (P2_{lat} - P1_{lat}) - (P2_{mag} - P1_{mag}). \end{aligned}$$

The “lat” and “mag” subscripts refer to the latitude coordinate and magnitude of the anomaly, respectively, for P1 and P2 (refer to Tables 3.4 and 3.5). The SSI is intended to quantify a model’s ability to reproduce the flow see-saw and should not be used as an overall indicator of model performance. Some uncertainties exist regarding how influential the latitude and magnitude differences are on the final calculation, and whether or not P3 is strong enough to play a role. Additionally, the SSI accounts for the differences in P1 and P2 relative to each other and does not compare the absolute locations to those of NCEP. Nevertheless, we make a general assumption that values of the SSI that are closer to zero provide more realistic representations of the PNA spatial structure over the North Pacific and western North America.

The calculated SSIs (Table 3.6) indicate that models with index values between 0 and 10 accurately reproduce the shift in flow patterns models, with index values between 10 and 20 partially reproduce the shift in flow patterns, and models with index values  $\geq 20$  do not reproduce the shift in flow patterns. For example, FIO-ESM, CanESM2, and FGOALS-g2 have low SSIs and are (visibly) more accurate

**Table 3.6** The see-saw index (SSI), difference factor (DF), and ranking value (SSI+DF) for each model. The overall model ranking in the last column is based on the ranking value.

Model	SSI	Difference Factor	Ranking Value	Ranking
<b>ACCESS1-0</b>	17.06	33.36	50.42	18
<b>BCC-CSM1.1</b>	2.56	27.05	29.61	6
<b>BNU-ESM</b>	12.81	21.71	34.53	9
<b>CanESM2</b>	2.11	30.18	32.29	8
<b>CCSM4</b>	10.01	21.24	31.25	7
<b>CNRM-CM5</b>	19.02	22.93	41.95	12
<b>FGOALS-g2</b>	2.22	34.99	37.22	11
<b>FGOALS-s2</b>	16.55	29.79	46.34	14
<b>FIO-ESM</b>	0.95	25.14	26.09	4
<b>GFDL-CM3</b>	21.26	31.43	52.68	20
<b>GFDL-ESM2G</b>	8.00	17.26	25.26	3
<b>GFDL-ESM2M</b>	24.26	31.60	55.86	21
<b>GISS-E2-R</b>	13.65	37.71	51.35	19
<b>HadGEM2-AO</b>	20.91	26.67	47.58	15
<b>HadGEM2-CC</b>	42.10	27.18	69.28	24
<b>HadGEM2-ES</b>	15.52	33.73	49.26	17
<b>INM-CM4</b>	19.27	44.26	63.53	23
<b>IPSL-CM5A-LR</b>	29.24	40.54	69.78	26
<b>IPSL-CM5A-MR</b>	13.57	34.44	48.01	16
<b>IPSL-CM5B-LR</b>	42.35	27.08	69.43	25
<b>MIROC5</b>	7.26	19.99	27.25	5
<b>MIROC-ESM</b>	32.57	26.57	59.13	22
<b>MIROC-ESM-CHEM</b>	50.46	26.39	76.85	27
<b>MPI-ESM-LR</b>	10.34	26.33	36.68	10
<b>MPI-ESM-MR</b>	2.58	15.15	17.73	1
<b>MRI-CGCM3</b>	13.67	29.50	43.18	13
<b>NorESM1-M</b>	4.86	19.71	24.58	2

(Figs. 3.5 and 3.9), whereas GFDL-CM3, INMCM4, and MIROC-ESM-CHEM have SSIs well above 20 and are either locked into a meridional or zonal flow for both positive and negative modes (Figs. 3.5 and 3.9).

A “Difference Factor” (DF) is simply the sum of the average location differences and the average magnitude differences listed in Tables 3.4 and 3.5. The DF provides a more general assessment of overall model performance compared to NCEP with respect to spatial variability, and includes the influence of all three centers (Table 3.6). Similar to the SSI, DF values closer to zero indicate better overall model performance (e.g., MPI-ESM-MR, GFDL-ESM2G, and NorESM1-M), as these models produce the smallest differences from NCEP in both the locations and magnitudes of P1, P2, and P3. The DF and the SSI can be summed to produce a ranking value that combines measures of center location, anomaly strength, and the ability to reproduce distinct positive and negative flow patterns (Table 3.6). Lower ranking values signify the smallest differences in the locations and magnitudes of all three centers between the model and NCEP. Consistent with visual comparisons and the previous quantitative assessments, MPI-ESM-MR, NorESM1-M, and GFDL-ESM2G are among the best models for simulating the PNA pattern.

### 3.4.4 Relationship to surface climate

#### *3.4.4.1 Correlation analysis*

While analysis of the atmospheric characteristics of the PNA is important, it is also important to assess the surface responses to PNA as expressed by air temperature

and precipitation that, in turn, drive other fields such as snowpack and soil moisture. The PNA is a strong control of both temperature and precipitation in North America (Figures 3.10 and 3.11, respectively; Wallace and Gutzler, 1981; Leathers et al., 1991). The temperature correlation pattern for NCEP vaguely resembles the PNA loading pattern seen in Figure 3.5. The general flow pattern associated with positive PNA modes is described by barotropic instability, which is characterized by cold troughs and warm ridges. As a result, negative correlation values are found over the North Pacific and southeast United States, while positive correlations cover the near-shore eastern Pacific and the western half of North America. That is, negative height anomalies (P1 and P3) are associated with cooler-than-normal temperatures, while positive height anomalies (P2) are associated with warmer-than-normal temperatures.

Most of the CMIP5 models reproduce this general pattern, albeit with some relatively large differences in magnitude and structure. The models that perform better based on the results summarized in Table 3.6 reproduce the temperature correlations most accurately. About half of the CMIP5 models underestimate the strength of the correlations, especially over Canada, which is in agreement with the inability of these models to accurately simulate the ridge associated with positive PNA modes (e.g., ACCESS1-0, HadGEM2-CC, and IPSL-CM5A-LR in Fig. 3.9). Although the negative-positive-negative pattern is apparent in FGOALS-s2 and MRI-CGCM3, the pattern is shifted such that the sign of the correlation over Alaska is flipped and positive correlations over Canada are too strong and too widespread. The region of transition between the negative and positive correlations varies widely among the

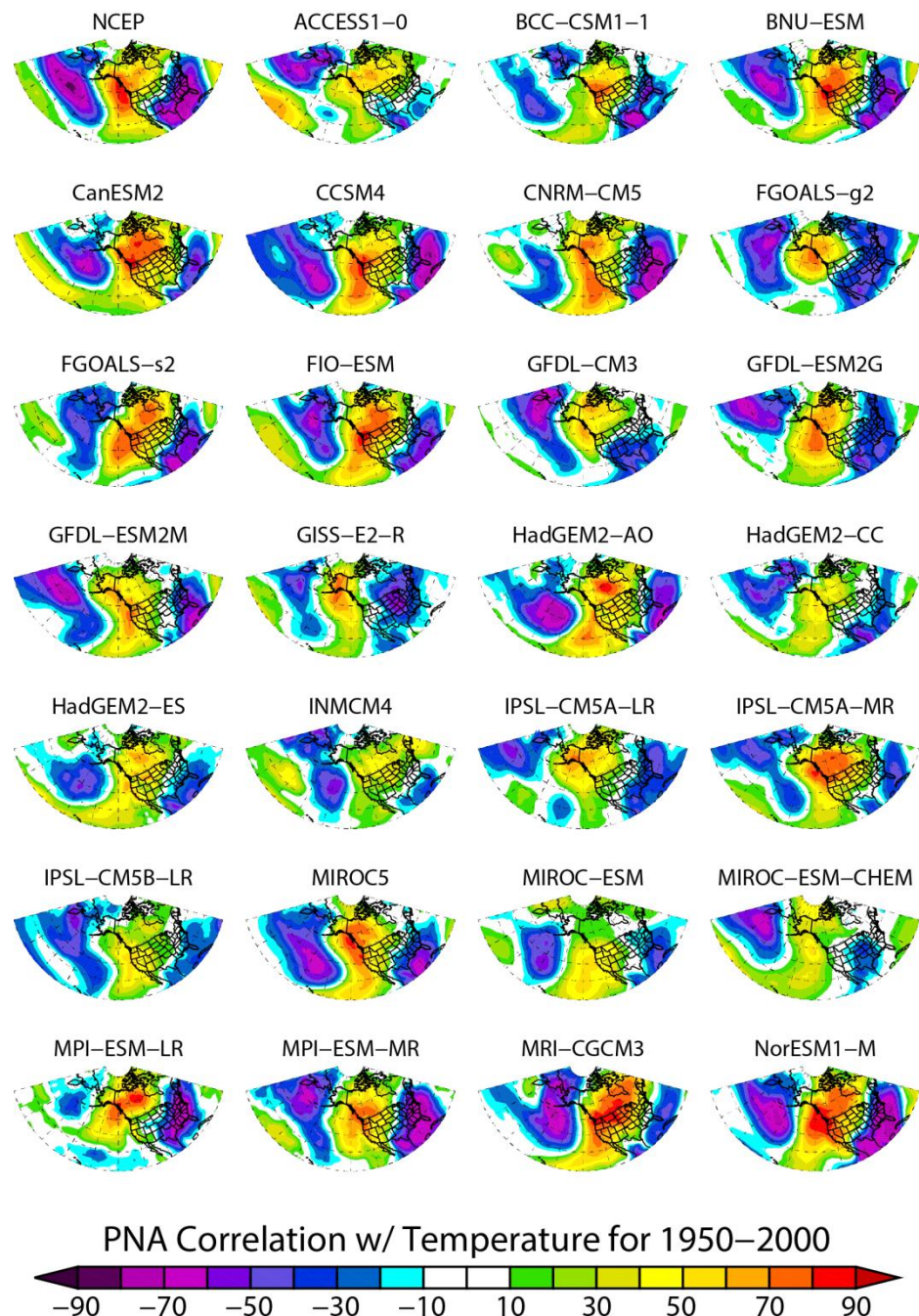


**Figure 3.10** The temporal correlation between the 2-m surface temperature anomalies and the PNA index for the month of January relative to the DJF winter season for the years 1950-2000.

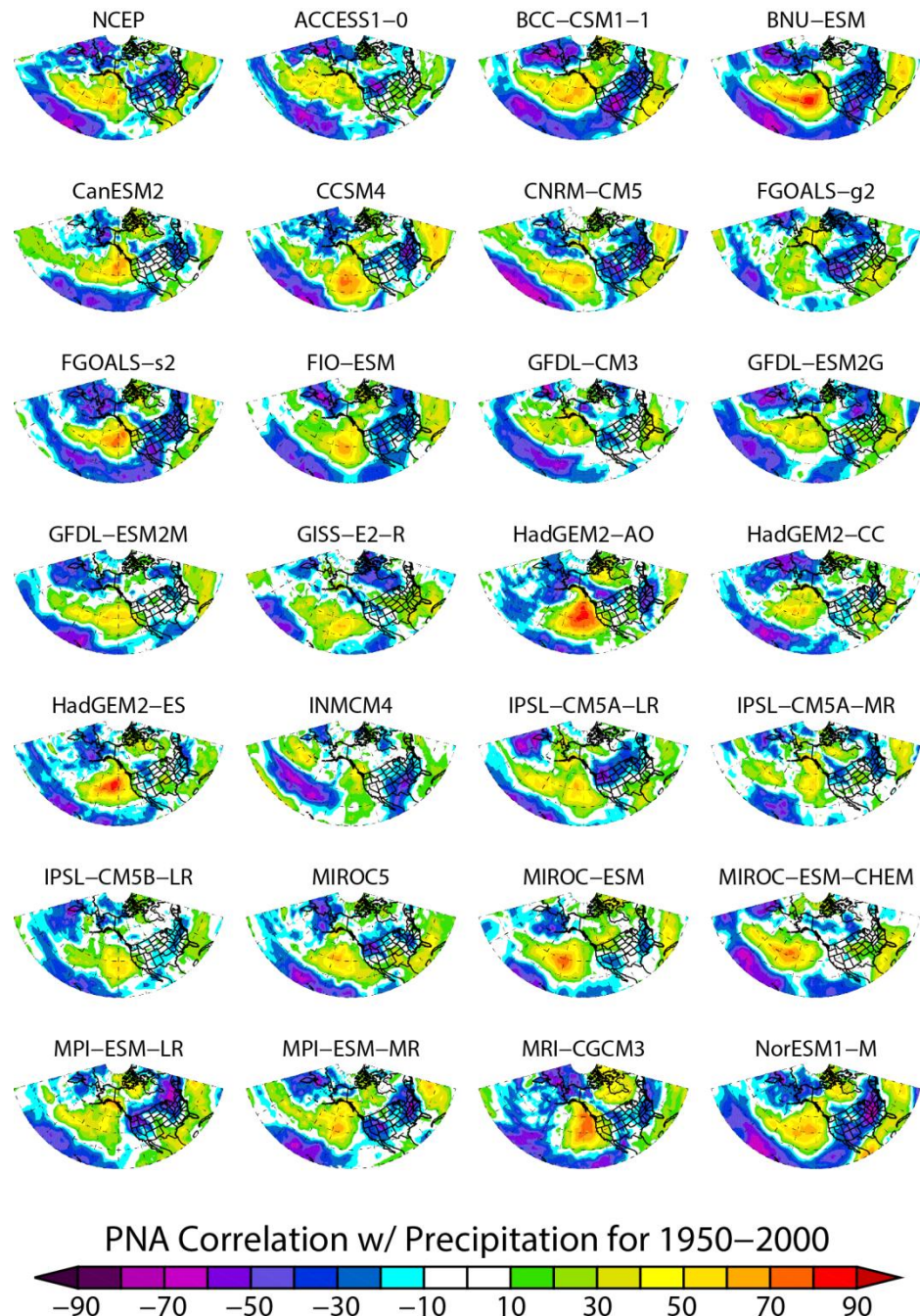


**Figure 3.11** As in Fig. 3.10, for the precipitation rate.

models. In NCEP, the path of neutral correlation across the United States runs just east of California, across the Midwest, and then north through the Great Lakes. . Small deviations from this path may appear to be inconsequential on a global scale; however, for regional climates the shift imparts large climatic consequences for the locations on either side of the neutral zone. Because positive correlations exist to the north/west of the neutral zone and negative correlations exist to the south/east, small shifts in this pattern could mean the difference between anomalously warm and anomalously cold conditions. Furthermore, for individual PNA events the exact location of the troughs and ridges may not be consistent. Rodionov and Assel (2001) analyzed the winters of 1976/77 and 1997/98 and found that, despite the high value of the PNA index in both seasons, the flow was much more zonal in 1997/98 and thus produced unseasonably warm temperatures throughout most of North America. They attribute this difference to the influence of the strong El Niño event in the winter of 1997/98, which they find flattens the polar jet stream and pulls the subtropical jet stream southward.

The precipitation correlation patterns are slightly weaker and less well-defined (Figure 3.11). NCEP shows a clear dipole in the North Pacific with a moderately strong positive correlation extending off of the west coast of North America, accompanied by regions of negative correlation to the north and south. During positive PNA modes, negative correlations across the continental United States are related to the ridge at P2 associated with positive modes, while the weak positive correlations in the southeast and through Mexico are related to the trough at P3. The

influence of the PNA on precipitation patterns is much stronger over the ocean than over land, especially in the North Pacific, which is a side effect of the Aleutian low. Strong positive PNA phases, when the negative height anomaly at P1 deepens, are associated with “Pineapple Express” events, which pull warm, moist storms from the subtropics and create an atmospheric river of moisture from Hawaii and northeast to the west coast of the U.S. These events are primarily responsible for the large positive precipitation correlation in the North Pacific, and in extreme cases can also shift the precipitation influence over land in the Pacific Northwest (Abatzoglou 2010).

Similar to the temperature correlations (Fig. 3.10), the CMIP5 models generally simulate the NCEP precipitation pattern, but with some obvious differences. The accuracy of the precipitation patterns is particularly sensitive to the strength and location of P1 and P2 in each of the models. For example, a P1 center that is shifted too far east results in positive precipitation correlations that are too strong and lack the “tongue” that extends westward from the continental U.S. (e.g., HadGEM2-AO, HadGEM2-ES, and MRI-CGCM3). Over Canada, most commonly the P2 center is too weak compared to NCEP, which reduces the chances for ridge formation and thus the negative correlation over land is weakened or completely eliminated (e.g., GFDL-CM3, IPSL-CM5B-LR, and MIROC-ESM-CHEM). Other models grossly overestimate the negative correlation over land, a consequence of a strong P2 anomaly extending south through California, off the west coast, and connecting with the subtropical center of action (e.g., BCC-CSM1-1, BNU-ESM, and FGOALS-s2).

The interaction between the temperature and precipitation correlation patterns influences the type of climate a region experiences for an average winter season. In most models, locations where the PNA expresses a positive correlation over both temperature and precipitation typically experience warm and wet or cold and dry winters (e.g., the extreme Pacific Northwest and southeast North America). The mountainous West experiences a positive temperature and negative precipitation correlation, which suggests cooler- and wetter-than-normal conditions under a negative PNA and likely contributes to the accumulation of winter snowpack. On the other hand, in many models temperature/precipitation patterns in the central Midwest are variable. The neutral zone between positive and negative temperature correlations runs through this region, making climate conditions dependent the exact positioning of this zone, as well as on the value of the precipitation correlation.

#### *3.4.4.2 Extremes analysis*

We compute surface climate anomalies for extreme positive and negative PNA index years. Extreme years are defined as the top and bottom 33% of PNA index values greater and less than  $\pm 0.5$ , respectively, for each model's index time series. This produces maps that depict the surface climate changes associated with most extreme positive ("PNA+") and negative ("PNA-") events. The temperature and precipitation anomalies for these extremes should generally resemble the correlation maps in the previous section, as regions of positive (negative) correlations relate to regions of positive (negative) anomalies.

PNA+ events in NCEP generally produce positive temperature anomalies over Canada and Alaska of up to +4°C or more in the higher latitudes, with weaker positive anomalies ranging from +0.25-1°C extending down the west coast of North America (Fig. 3.12). Due to a cold northerly and northwesterly flow out of Canada during PNA+ events, negative anomalies up to -2°C dominate the majority of the United States east of the Rocky Mountains, with the largest anomalies occurring in the central Appalachian Mountains. PNA- events produce almost completely opposite temperature anomaly patterns compared to the positive extremes (Fig. 3.13). Weak negative anomalies up to -1°C cover northwestern Canada, Alaska, and the Gulf of Alaska, with near-zero changes throughout the rest of Canada and the extreme northwest of the United States. Positive anomalies up to +2°C dominate the majority of the U.S. and much of Mexico. The temperature changes over the ocean for both PNA+ and PNA- are minimal due to the slow response time of ocean temperatures to changing atmospheric conditions.

Most CMIP5 models are able to produce the general temperature anomaly patterns associated with positive and negative events (Figs. 3.12 and 3.13). The magnitude of the warming over northwestern North America is related to the P1-P2 relationship, and thus the value of the SSI; models that more accurately reproduce the flow see-saw also better represent the temperature anomaly patterns for both PNA+ and PNA- (e.g., GFDL-ESM2G and MPI-ESM-MR). Several models produce warming that is too widespread during PNA+ events, a discrepancy that we attribute to a relatively weak P3 height anomaly compared to that of P2. The low geopotential

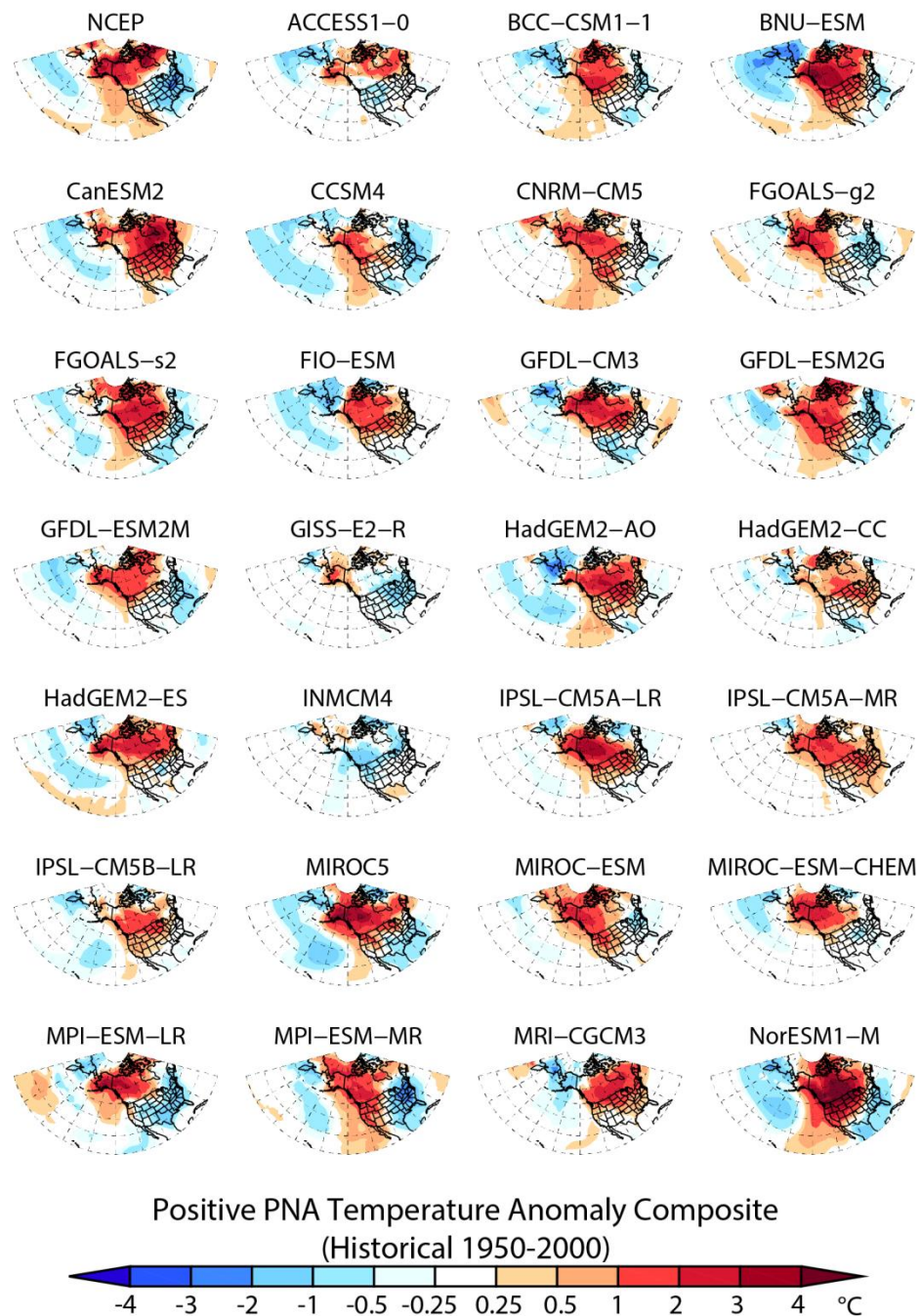


**Figure 3.12** Composite maps for the temperature anomalies for the top 33% of positive PNA years for the Historical simulation. Anomalies are taken from the 1950–2000 climatology.

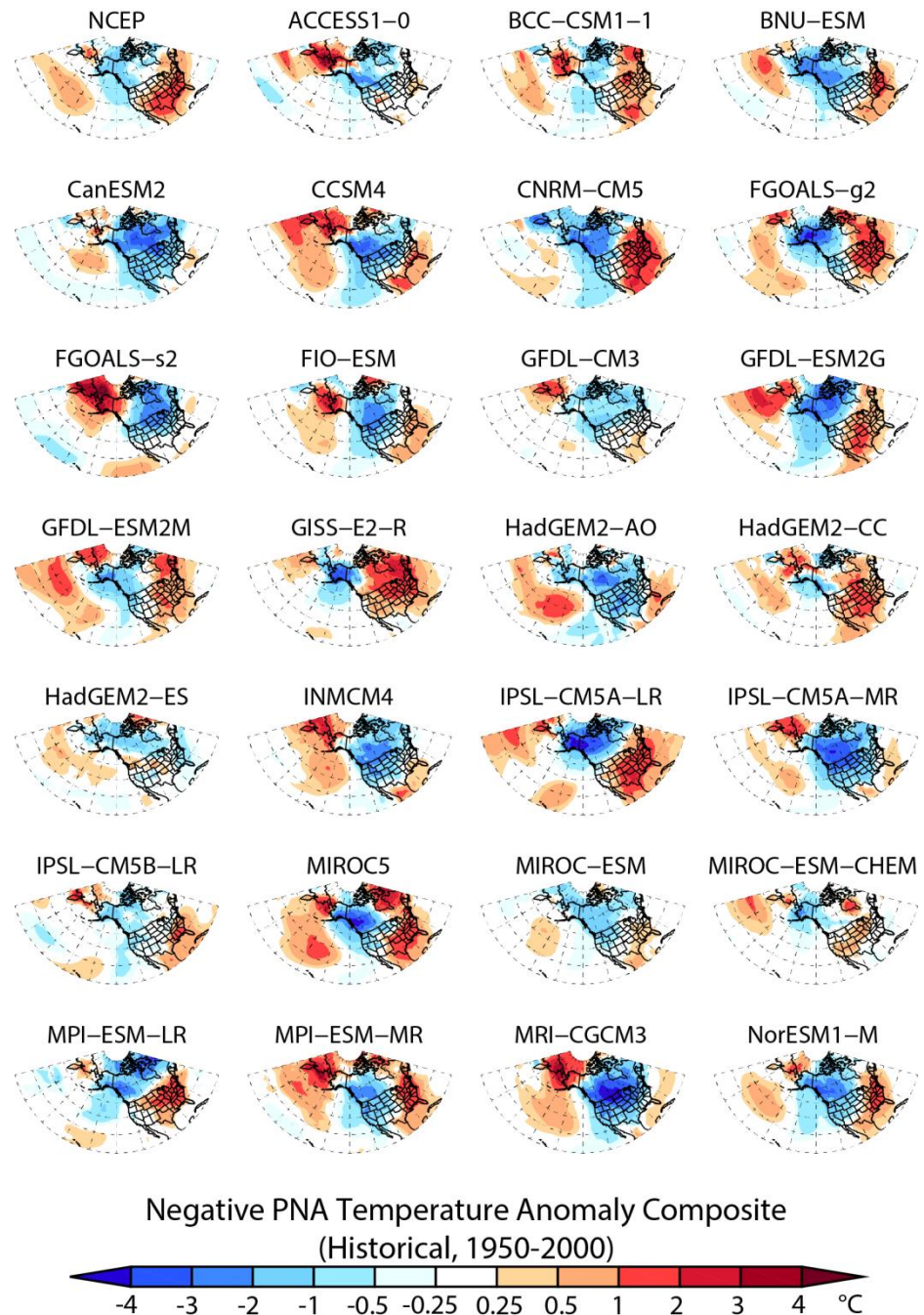


**Figure 3.13** As in Fig. 3.12, for the bottom 33% of negative PNA index years.

heights at P3 during PNA+ create cooler-than-normal temperatures in the southeastern U.S., and thus a dominant P2 center overwhelms the influence of P3 and increases temperatures across most of North America, in some models up to 1°C more than NCEP (e.g., CanESM2 and MRI-CGCM3). Nearly half of the CMIP5 models overestimate the negative anomalies over North America by several degrees relative to those seen in NCEP for PNA- events (Fig. 3.13). These discrepancies are again related to the difference in magnitudes of the P1 and P2 height anomalies. For PNA- events the P1 height anomaly is positive and the P2 height anomaly is negative; if the P2 anomaly is comparatively stronger in magnitude than the P1 anomaly then this center will pull too much Arctic air from the northern latitudes, which results in a cold bias over North America (e.g., CanESM2, IPSL-CM5A-MR, and MPI-ESM-LR).

Precipitation changes due to PNA+ and PNA- events are much more spatially variable than those for surface temperature (Figs. 3.14 and 3.15). As in the correlation analysis between the PNA and precipitation, the most prominent PNA+ feature in NCEP is the dipole between positive and negative precipitation anomalies over the Pacific Ocean (Fig. 3.14). The positive anomalies in this region reach ~2 mm/day in the positive area and 1 mm/day in the negative area surrounding Hawaii. During PNA+, the atmospheric circulation around the Aleutian low at P1 creates increased storminess as warm, moist air travels from the subtropics and north into the Gulf of Alaska. Observations reveal that especially strong PNA+ events can pull the region of positive precipitation anomalies over land; however, on average this region remains over the Pacific Ocean (Abotzoglou, 2010). Strong subsidence and ridging associated

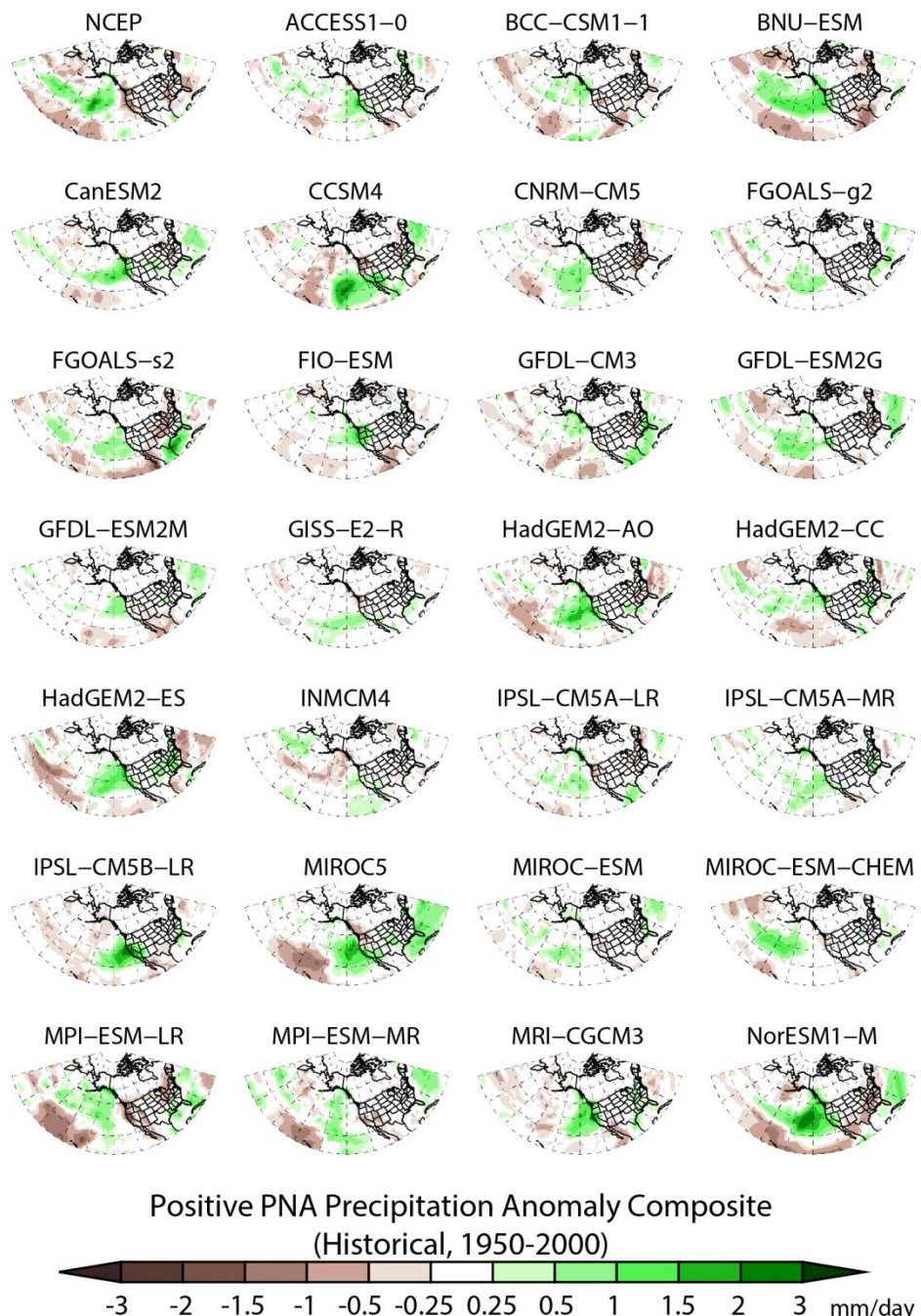


**Figure 3.14** Composite maps for the precipitation anomalies for the top 33% of positive PNA years for the Historical simulation. Anomalies are taken from the 1950–2000 climatology.

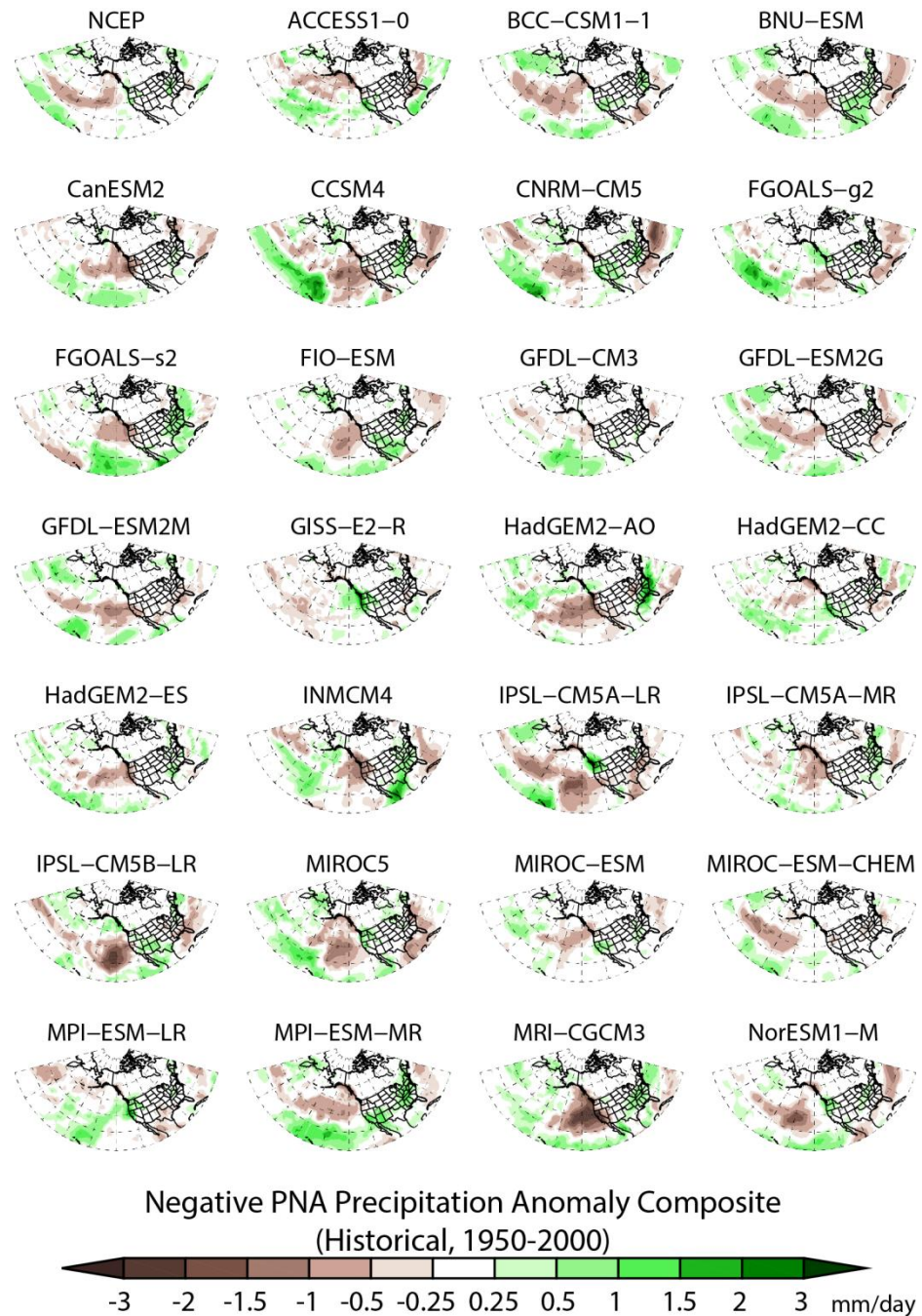


**Figure 3.15** As in Fig. 3.14, for the bottom 33% of negative PNA index years.

with the high pressure at P2 inhibits precipitation formation, resulting in negative precipitation anomalies along the west coast of the U.S. Precipitation throughout most of Canada, the central U.S., and much of Mexico appears unaffected by both PNA+ and PNA- events, as evidenced by neither positive nor negative anomalies for either case. Despite the low pressure associated with P3, the eastern seaboard experiences negative precipitation anomalies during PNA+, as the source of air to this region is land-based and lacks the moisture needed for widespread precipitation. Additionally, precipitation in this area is often convective, of which many global climate models are unable to capture due to low resolutions. The NCEP patterns associated with PNA- are comparably weaker than those with PNA+ (Fig. 3.15). A region of negative anomalies up to -1.5 mm/day appear over the North Pacific, a response to the high pressure associated with P1 during PNA-, with scattered areas of 0.5-1 mm/day positive anomalies to the north and south. The remainder of the PNA sector is largely unaffected, except for a few scattered regions of ~0.5 mm/day positive anomalies across the U.S.

Only about one-third of the CMIP5 models reproduce the precipitation dipole over the North Pacific associated with PNA+ (Fig. 3.14). The positioning of the P1 center relative to the subtropical high over Hawaii largely influences the structure of the dipole. While many models appear to produce an adequate subtropical high, the location and strength of P1 varies substantially, resulting in a disorganized precipitation pattern over the North Pacific (e.g., CCSM4, GFDL-CM3 and MRI-CGCM3). Furthermore, several models feature a P1 center of action that is too

widespread (refer to Fig. 3.7), which pushes the positive precipitation anomalies over land (e.g., FIO-ESM and NorESM1-M). In NCEP this region is under a negative anomaly, identifying the west coast of North America as an area of large discrepancy in the CMIP5 models. Most models exhibit the drying seen in NCEP during PNA+ events; however, southwest North America is a persistent region of disagreement, as many models indicate wetter, rather than drier conditions (e.g., FGOALS-s2 and NorESM1-M). We attribute this discrepancy to an overactive P3 center; in these models this center is too widespread and often shifted southeast (refer to Fig. 3.7), which pulls moisture from the Gulf of Mexico allowing for increased precipitation in the region.

Nearly half of the CMIP5 models exhibit excessive drying up to -3 mm/day over the North Pacific during PNA- events, which is in large disagreement with NCEP (Fig. 3.15; e.g., HadGEM2-AO and IPSL-CM5B-LR). Zonal flow associated with PNA- events cuts off the moisture supply from the tropics thereby creating a drying effect in the North Pacific. However, too much drying in these models is likely associated with the creation of too much precipitation in general. The SSI values for these models are relatively high, consistent with the flow patterns in Figure 3.9, indicating meridional flow during both positive and negative events. Extreme negative events, as shown in the composite maps, can still produce zonal flow in the models, yet relative to the mean state the drying effect is exaggerated.

### 3.5 Conclusions

The Pacific-North American teleconnection pattern is simulated and recognizable in each of the CMIP5 models we analyzed, with the exception of INMCM4. Individual differences in grid resolution, model dynamics, and parameterization schemes likely influence a model's ability to resolve the teleconnection pattern and as a result, different models simulate different aspects of the PNA with more or less accuracy. For example, a model that is able to better simulate ENSO might also better simulate the PNA. The PNA exhibits highest spectral power at low frequencies of 3-7 years, which is consistent with the period of ENSO, and literature suggests a relationship between warm-phase ENSO events (El Niño) and positive phase PNA events (Rodionov and Assel, 2001). Thus, if a model is unable to accurately simulate ENSO, then these discrepancies will transfer to the model's simulation of the PNA.

Each of the CMIP5 models produce a realistic time series of the PNA based on the RPCA analysis from which PNA-like patterns are identified. The periodicity associated with these indices varies widely; however, each model displayed a “red” spectral shape, indicating accurate portrayal of the PNA as a predominantly low-frequency teleconnection. The disparities associated with an individual model's representation of the pattern inevitably have implications for the ability of these models to simulate long-term, future climate trends over North America.

It is evident that relationships between the PNA and temperature and precipitation are well defined and the sign of the PNA index plays a role in influencing

surface climate. The temperature and precipitation extreme anomaly maps are consistent with the patterns seen in the correlation analysis. The influence of the relationship between P2 and P3 is most influential over the temperature anomalies, as temperature changes between positive and negative PNA events are strongest over land, while the P1-P2 relationship is more important for the precipitation anomalies over the North Pacific. Chen and van den Dool (2003) show that the teleconnections associated with strong positive PNA modes, as defined by the P1 anomaly, extend much farther into the Western Atlantic than do comparatively strong negative events, whose influences tend to remain focused over North America. The difference in the strength and extent of the teleconnection can be attributed to the propagation of wave energy associated with the barotropic instability that initiates a positive PNA mode (Simmons et al., 1983). Thus, the relationships defined here describe the climatological average and do not necessarily represent the behavior of individual PNA events.

The ability of the CMIP5 models to simulate the PNA teleconnection pattern is promising for analyzing the performance of the models in future climate scenarios. The PNA represents a robust feature of mid-latitude atmospheric dynamics and its presence in a climate model is imperative to accurately simulating the climate in North America. Although an observational baseline is impossible for the future, the results presented in this study can be used to assess changes throughout the next century.

### 3.6 Acknowledgements

We acknowledge the World Climate Research Programme's Working Group on Coupled Modelling, which is responsible for CMIP, and we thank the climate modeling groups (listed in Table 3.1 of this paper) for producing and making available their model output. For CMIP the U.S. Department of Energy's Program for Climate Model Diagnosis and Intercomparison provides coordinating support and led development of software infrastructure in partnership with the Global Organization for Earth System Science Portals. Funding for this research was provided by the U.S. Geological Survey.

### 3.7 References

- Abatzoglou, J.T. (2010): Influence of the PNA on declining mountain snowpack in the Western United States. *Intl. J. Clim.*, 8 pp.
- Bao, Q., G. Wu, Y. Liu, J. Yang, Z. Wang, T. Zhou (2010): An introduction to the coupled model FGOALS1.1-s and its performance in East Asia. *Adv. Atmos. Sci.*, **27**(5), 1131-1142.
- Barnston, A.G. and R.E. Livezey (1987): Classification, seasonality and persistence of low-frequency atmospheric circulation patterns. *Mon. Wea. Rev.*, **115**, 1083-1126.
- Bi, D. (2012): ACCESS: The Australian coupled climate model for IPCC AR5 and CMIP5. 2012 Australian Meteorological and Oceanographic Society (AMOS) Conference; Sydney, Australia: <https://wiki.csiro.au/confluence/display/ACCESS/ACCESS+Publications>.
- Chen, W.Y. and H. van den Dool (2003): Sensitivity of teleconnection patterns to the sign of their primary action center. *Mon. Wea. Rev.*, **131**, 2885-2899.
- Chylek, P., J. Li, M.K. Dubey, M. Wang, and G. Lesins (2011): Observed and model simulated 20th century Arctic temperature variability Canadian Earth System Model CanESM2. *Atmos. Chem. Phys. Discuss.*, **11**, 22893-22907.

Collins, N. Bellouin, M. Doutriaux-Boucher, N. Gedney, Hinton, C.D. Jones, S. Liddicoat, G. Martin, F. O'Connor, Rae, C. Senior, I. Totterdell, S. Woodward. Reichler, and J. Kim (2008): Evaluation of the HadGEM2 model. Hadley Centre technical note 74, 47 pp.

Donner, L.J., B.L. Wyman, R.S. Helmer, L.W. Horowitz, Y. Ming, M. Zhao, J.-C. Golaz, P. Ginoux, S.-J. Lin, M.D. Schwarzkopf, J. Austin, G. Alaka, W.F. Cooke, T.L. Delworth, S.M. Freidenreich, C.T. Gordon, S.M. Griffies, I.M. Held, W.J. Hurlin, S.A. Klein, T.R. Knutson, A.R. Langenhorst, H.-C. Lee, Y. Lin, B.I. Magi, S.L. Malyshev, P.C.D. Milly, V. Naik, M.J. Nath, R. Pincus, J.J. Ploshay, V. Ramaswamy, C.J. Seman, E. Shevliakova, J.J. Sirutis, W.F. Stern, R.J. Stouffer, R.J. Wilson, M. Winton, A.T. Wittenberg, and F. Zeng (2011): The dynamical core, physical parameterizations, and basic simulation characteristics of the atmospheric component AM3 of the GFDL global coupled model CM3. *J. Climate*, **24**, 3484-3519.

Dufresne, J.-L., M.-A. Foujols, S. Denvil, A. Caubel, O. Marti, O. Aumont, Y. Balkanski, S. Bekki, H. Bellenger, R. Benshila, S. Bony, L. Bopp, P. Braconnot, P. Brockmann, P. Cadule, F. Cheruy, F. Codron, A. Cozic, D. Cugnet, N. de Noblet, J.-P. Duvel, C. Ethé, L. Fairhead, T. Fichefet, S. Flavoni, P. Friedlingstein, J.-Y. Grandpeix, L. Guez, E. Guilyardi, D. Hauglustaine, F. Hourdin, A. Idelkadi, J. Ghattas, S. Joussaume, M. Kageyama, G. Krinner, S. Labetoulle, A. Lahellec, M.-P. Lefebvre, F. Lefevre, C. Levy, Z.X. Li, J. Lloyd, F. Lott, G. Madec, M. Mancip, M. Marchand, S. Masson, Y. Meurdesoif, J. Mignot, I. Musat, S. Parouty, J. Polcher, C. Rio, M. Schulz, D. Swingedouw, S. Szopa, C. Talandier, P. Terray, and N. Viovy (2012): Climate change projections using the IPSL-CM5 Earth System Model: From CMIP3 to CMIP5. *Clim. Dyn.*, submitted, 53 pp.

Dunne, J.P., J.G. John, A.J. Adcroft, S.M. Griffies, R.W. Hallberg, E. Shevliakova, R.J. Stouffer, W. Cooke, K.A. Dunne, M.J. Harrison, J.P. Krasting, S.L. Malyshev, P.C.D. Milly, P.J. Phillipps, L.A. Sentman, B.L. Samuels, M.J. Spelman, M. Winton, A.T. Wittenberg, N. Zadeh (2012): GFDL's ESM2 global coupled climate-carbon Earth System Models Part I: Physical formulation and baseline simulation characteristics. *J. Climate* [Early online release: <http://journals.ametsoc.org/doi/pdf/10.1175/JCLI-D-11-00560.1>], 64 pp.

Ganguly, A.R., K. Steinhaeuser, D.J. Erikson III, M. Branstetter, E.S. Parish, N. Singh, J.B. Drake, and L. Buja (2009): Higher trends but larger uncertainty and geographic variability in 21st century temperature and heat waves. *PNAS*, **106**(37), 15555-15559.

Gent, P.R., G. Danabasoglu, L.J. Donner, M.M. Holland, E.C. Hunke, S.R. Jayne, D.M. Lawrence, R.B. Neale, P.J. Rasch, M. Vertenstein, P.H. Worley, Z-L. Yang,

- M. Zhang (2011): The Community Climate System Model Version 4. *J. Climate*, **24**, 4973-4991.
- Gilman, D.L., F.J. Fuglister, and J.M. Mitchell Jr. (1963): On the power spectrum of “red noise”. *J. Atmos. Sci.*, **20**, 182-184.
- Hourdin, F., M.-A. Foujols, F. Codron, V. Guemas, J.-L. Dufresne, S. Bony, S. Denvil, L. Guez, F. Lott, J. Ghattas, P. Braconnot, O. Marti, Y. Meurdesoif, L. Bopp (2012): Impact of the LMDZ atmospheric grid configuration on the climate and sensitivity of the IPSL-CM5A coupled model. *Clim. Dyn.*, submitted, 39 pp.
- Jungclaus J.H., S.J. Lorenz, C. Timmreck, C.H. Reick, V. Brovkin, K. Six, J. Segschneider, M.A. Giorgetta, T.J. Crowley, J. Pongratz, N.A. Krivova, L.E. Vieira, S.K. Solanki, D. Klocke, M. Botzet, M. Esch, V. Gayler, H. Haak, T.J. Raddatz, E. Roeckner, R. Schnur, H. Widmann, M. Claussen, B. Stevens, and J. Marotzke (2010): Climate and carbon-cycle variability over the last millennium. *Clim. Past*, **6**, 723-737.
- Kalnay, E., M. Kanamitsu, R. Kistler, W. Collins, D. Deaven, L. Gandin, M. Iredell, S. Saha, G. White, J. Woollen, Y. Zhu, A. Leetmaa, B. Reynolds, M. Chelliah, W. Ebisuzaki, W. Higgins, J. Janowiak, K.C. Mo, C. Ropelewski, J. Wang, R. Jenne, and D. Joseph (1996): The NCEP/NCAR 40-year reanalysis project. *Bull. Amer. Met. Soc.*, **77**, 437-471.
- Kitoh, A., et al. (2007): Model development at MRI. 3rd China-Korea-Japan Joint Conference on Meteorology; Beijing, China.
- Le Quéré, C., M.R. Raupach, J.G. Canadell, G. Marland, L. Bopp, P. Ciais, T.J. Conway, S.C. Doney, R.A. Feely, P. Foster, P. Friedlingstein, K. Gurney, R.A. Houghton, J.I. House, C. Huntingford, P.E. Levy, M.R. Lomas, J. Majkut, N. Metzl, J.P. Ometto, G.P. Peters, I.C. Prentice, J.T. Randerson, S.W. Running, J.L. Sarmiento, U. Schuster, S. Sitch, T. Takahashi, N. Viovy, G.R. van der Werf, and F.I. Woodward (2009): Trends in the sources and sinks of carbon dioxide. *Nat. Geo.*, **2**, 831-836.
- Leathers, D.J., B. Yarnal, M.A. Palecki (1991): The Pacific/North American teleconnection pattern and United States climate. Part I: Regional temperature and precipitation associations. *J. Climate*, **4**, 517-528.
- Martin, G.M., N. Bellouin<sup>1</sup>, W.J. Collins, I.D. Culverwell, P.R. Halloran, S.C. Hardiman, T. J. Hinton, C.D. Jones, R.E. McDonald, A.J. McLaren, F.M. O’Connor, M.J. Roberts, J.M. Rodriguez, S. Woodward, M.J. Best, M.E. Brooks, A.R. Brown, N. Butchart, C. Dearden, S.H. Derbyshire, I. Dharssi, M. Doutriaux-Boucher, J.M. Edwards, P.D. Falloon, N. Gedney, L.J. Gray, H.T. Hewitt, M.

Hobson, M.R. Huddleston, J. Hughes, S. Ineson, W.J. Ingram, P.M. James, T.C. Johns, C.E. Johnson, A. Jones, C.P. Jones, M.M. Joshi, A.B. Keen, S. Liddicoat, A.P. Lock, A.V. Maidens, J.C. Manners, S.F. Milton, J.G.L. Rae, J.K. Ridley, A. Sellar, C.A. Senior, I.J. Totterdell, A. Verhoef, P.L. Vidale, and A. Wiltshire (2011): The HadGEM2 family of Met Office Unified Model Climate configurations. *Geosci. Mod. Dev. Discuss.*, **4**, 765-841.

Moss, R.H., J.A. Edmonds, K.A. Hibbard, M.R. Manning, S.K. Rose, D.P. van Vuuren, T.R. Carter, S. Emori, M. Kainuma, T. Kram, G.A. Meehl, J.F.B. Mitchell, N. Nakicenovic, K. Riahi, S.J. Smith, R.J. Stouffer, A.M. Thomson, J.P. Weyant, and T.J. Wilbanks (2010): The next generation of scenarios for climate change research and assessment. *Nature*, **463**, 747-756.

Otterå, O.H. (2011): Simulating the climate from Paleocene to present-day and beyond: Challenges in climate modeling. 10th Annual Meeting on High Performance Computing and Infrastructure in Norway; Oslo, Norway.

Rodionov, S. and R. Assel (2001). A new look at the Pacific/North American index. *Geophys. Res. Lett.*, **28**(8), 1519-1522.

Rogelj, J., M. Meinshausen, and R. Knutti (2012): Global warming under old and new scenarios using IPCC climate sensitivity range estimates. *Nat. Clim. Change*, 6 pp.

Simmons, A.J., J.M. Wallace, and G.W. Branstator (1983): Barotropic wave propagation and instability, and atmospheric teleconnection patterns. *J. Atmos. Sci.*, **40**(6), 1363-1392.

Straus, D.M. and J. Shukla (2002): Does ENSO force the PNA? *J. Climate*, **15**, 2340-2358.

Taylor, K.E., R.J. Stouffer, and G.A. Meehl (2012): An overview of CMIP5 and the experiment design. *Bull. Amer. Met. Soc.*, 485-498.

Voldoire, A., E. Sanchez-Gomez, D. Salas y Melia, B. Decharme, C. Cassou, S. Se'ne'si, S. Valcke, I. Beau, A. Alias, M. Chevallier, M. De'que', J. Deshayes, H. Douville, E. Fernandez, G. Madec, E. Maisonnave, M.-P. Moine, S. Planton, D. Saint-Martin, S. Szopa, S. Tyteca, R. Alkama, S. Belamari, A. Braun, L. Coquart, and F. Chauvin (2012): The CNRM-CM5.1 global climate model: description and basic evaluation. *Clim. Dyn.*, 31 pp.

Volodin, E.M., N.A. Dianskii, and A.V. Gusev (2010): Simulating present-day climate with the INMCM4.0 coupled model of the atmospheric and oceanic general circulations. *Atm. Oc. Phys.*, **46**(4), 414-431.

- Wallace, J.M. and D.S. Gutzler (1981): Teleconnections in the geopotential height field during the Northern Hemisphere winter. *Mon. Wea. Rev.*, **109**, 784-812.
- Watanabe, M., T. Suzuki, R. O'Ishi, Y. Komuro, S. Watanabe, S. Emori, T. Takemura, M. Chikira, T. Ogura, M. Sekiguchi, K. Takata, D. Yamazaki, T. Yokohata, T. Nozawa, H. Hasumi, H. Tatebe, M. Kimoto (2010): Improved climate simulation by MIROC5: Mean states, variability, and climate sensitivity. *J. Climate*, **23**, 6312-6335.
- Watanabe, S., T. Hajima, K. Sudo, T. Nagashima, T. Takemura, H. Okajima, T. Nozawa, H. Kawase, M. Abe, T. Yokohata, T. Ise, H. Sato, E. Kato, K. Takata, S. Emori, and M. Kawamiya (2011): MIROC-ESM: Model description and basic results of CMIP5-20c3m experiments. *Geosci. Model Dev. Discuss.*, **4**, 1063-1128.
- Yu, Y., H. Zhi, B. Wang, H. Wan, C. Li, H. Liu, W. Li, W. Zheng, and T. Zhou (2008): Coupled model simulations of climate changes in the 20th century and beyond. *Adv. Atmos. Sci.*, **25**(4), 641-654.
- Zanchettin, D., A. Rubino, and J.H. Jungclaus (2010): Intermittent multidecadal-to-centennial fluctuations dominate global temperature evolution over the last millennium. *Geo. Res. Lett.*, **37**(L14702), 6 pp.

Chapter 4: Analyzing the Pacific-North American teleconnection and its relationship to climate in the CMIP5 models, Part II: Future simulation

Andrea M. Allan<sup>1</sup> and Steven W. Hostetler<sup>2</sup>

<sup>1</sup>College of Earth, Ocean, and Atmospheric Sciences, Oregon State University,  
Corvallis, Oregon, 97331

<sup>2</sup>U.S. Geological Survey, Oregon State University, Corvallis, Oregon, 97331

#### 4.1 Abstract

We assess the presence of the Pacific-North American (PNA) teleconnection pattern in 27 atmosphere-ocean general circulation models (AOGCMs) and earth system models (ESMs) from the fifth phase of the Coupled Model Intercomparison Project (CMIP5) under the RCP8.5 future climate projection. We compare results from the future simulations to the historical results presented in Part I of this study. In addition, we use the National Centers for Environmental Prediction and Atmospheric Research (NCEP/NCAR) Reanalysis as a quasi-observational baseline in the evaluations of the CMIP5 climate models. We assess the PNA teleconnection both temporally and spatially, using a rotated principle component analysis (RPCA) to extract the PNA index time series and identify the spatial loading patterns. Each model's performance is assessed visually and by employing a series of calculations to quantify the model's simulation of the PNA under the future climate projection. We compare these results to the historical simulation for each model and to NCEP in order to understand how the PNA evolves throughout the 21<sup>st</sup> century. We also analyze the relationship between the PNA and surface air temperature and precipitation.

The CMIP5 models vary substantially in their ability to simulate different features of the PNA teleconnection. Most models are unable to resolve the temporal variability of NCEP for the 2050-2100 future time period; however, most of the models capture the PNA as a low-frequency oscillation, albeit with slightly varying periods. Spatial variability among the models is present as well, with few models agreeing on the nominal appearance of the PNA pattern in the future. It is also evident

that many models lack the ability to simulate the barotropic instability that initiates wave energy propagation through the 500-hPa geopotential height field, leading to a phase-locking and thus indistinguishable positive and negative modes of the PNA. The behavior of the models relative to NCEP is more conclusive than the trends within the models. The large majority of the CMIP5 models consistently underestimate the strength of the anomalies associated with the three “centers of action” that define the PNA pattern. Both the spatial and temporal discrepancies that arise among the models result in inconsistent relationships among the PNA and surface climate variables. Based on a comprehensive analysis, only a few models stand out in their ability to consistently represent all aspects of the PNA teleconnection.

## 4.2 Introduction

The role of the Pacific-North American (PNA) teleconnection pattern in observations is a topic that has been widely addressed (e.g., Wallace and Gutzler, 1981; Barnston and Livezey, 1987; Leathers et al., 1991); however, few studies have analyzed its presence and behavior under future climate change scenarios. The strong influence of the PNA on the climate in North America is motivation to understand the role of the teleconnection in climate models, as this will lead to better assessments of future climate.

Of the studies that have analyzed the historical PNA in AOGCMs, Stoner *et al.*, (2009) provides the most comprehensive evaluation while also investigating five other teleconnections. The analyses were performed over a 40-year time period and

provided only a qualitative view of the teleconnection patterns with no linkage to surface climate. Yu and Zwiers (2007) examined the response of climate in the PNA sector to ENSO and the PDO using 1,000 years of modeled output from the Canadian Centre for Climate Modelling and Analysis (CCCma) coupled global climate model. They found that all three teleconnections were represented in the GCM and compared well to observations. The study, however, focused on the strength of teleconnections and neither investigated the behavior of the PNA index, nor its influence over North American climates.

In Part I of this study, we assessed the ability of 27 climate models included in the fifth phase of the Coupled Model Intercomparison Project (CMIP5) to reproduce the “historical” (1950-2000) PNA both temporally and spatially under the premise that the better-performing models are likely to better simulate the future PNA. Here we present the second part in which we evaluate the PNA in the same 27 AOGCMs and ESMs under the RCP8.5 future climate scenario. Section 4.3 outlines the acquired model data and methods used for analysis. Section 4.4 presents the results of the temporal and spatial analyses with a concurrent discussion of these results. Section 4.5 links the simulated PNA to climate changes in North America, and Section 4.6 concludes the results. We note that many of the results presented here are for climate “averages” and do not reflect the performance of the CMIP5 models for individual months or years. Additionally, unless otherwise noted, the PNA displayed in all figures and tables is for January, which encompasses variability from the December

through February (DJF) winter season and these calculation methods are described in the following section.

### 4.3 Model data and methods

#### 4.3.1 AOGCMs and ESMs

The model output from CMIP5 hopes to provide the climate evaluations necessary to address outstanding questions from Intergovernmental Panel on Climate Change (IPCC) fourth Assessment Report (AR4) to then be included in the Fifth Assessment Report (AR5). The first CMIP5 model output was released to the public domain in February 2011, and the database continues to expand, with an effort to house a complete suite of model runs in time to support the IPCC fifth Assessment Report (AR5) that is scheduled for publication by the end of 2013 (Taylor et al., 2012). The IPCC AR5 report added four new greenhouse gas (GHG) scenarios, representative concentration pathways (RCPs), to the widely used Special Report on Emissions Scenarios (SRES) that were used in both the third (2001) and fourth (2007) IPCC assessment reports (SRES publication available here: <http://www.ipcc.ch/pdf/special-reports/spm/sres-en.pdf>). The RCPs are intended to be a better representation of the response of the climate system to increasing concentrations of GHGs through prescribing the same amount of radiative forcing in the models. The CMIP5 database contains a comprehensive set of output from both AOGCMs and Earth System Models (ESMs) for a variety of past, present, and future

modeling experiments, with the future experiments focusing on the new RCP scenarios (Moss et al., 2010).

Model output for CMIP5 is freely available for download from the data portal administered by the Program for Climate Model Diagnosis and Intercomparison (PCMDI, available at <http://pcmdi3.llnl.gov/esgcet/home.htm>). For our study, simulations from 27 AOGCMs and ESMs were collected for eight atmospheric variables and two experiments. The number of climate models used was limited by the data available in the portal as of June 1, 2012. Model institutions, horizontal and vertical resolution information, years, and references can be found in Table 3.1.

The “historical” and “RCP85” datasets were chosen from the suite of experiments available on the CMIP5 portal for their ability to simulate realistic global climate conditions. The historical experiment simulations cover from the mid-19th century through the near-present, and are forced by observed GHG changes. The historical runs also include other anthropogenic and natural forcings such as volcanic activity and land-cover changes (Taylor et al., 2012). The RCP85 experiment is referred to as the “high emissions” scenario with the total amount of radiative forcing exceeding  $8.5 \text{ W m}^{-2}$  by the year 2100 in response to continuous greenhouse gas emissions from double the number of emitters (world population increases from 6 billion in the year 2000 to 12 billion in the year 2100). This radiative forcing scenario is associated with an atmospheric carbon dioxide ( $\text{CO}_2$ ) concentration  $>1,370 \text{ ppm}$  (presently  $\sim 385 \text{ ppm}$ ), methane ( $\text{CH}_4$ ) concentration  $\sim 3500 \text{ ppb}$  (presently  $\sim 1075 \text{ ppb}$ ), and nitrous oxide  $\text{N}_2\text{O}$  concentration approaching 450 ppb (presently  $\sim 325 \text{ ppb}$ ) by the

end of the 21<sup>st</sup> century. Tropospheric ozone increases by an additional 0.2 W m<sup>-2</sup> due to changes in mono-nitrogen oxides and nitrogen dioxide (NO<sub>x</sub>), volatile organic compounds (VOCs), organic carbon, and CH<sub>4</sub> concentrations. Aerosol concentrations such as anthropogenic sulfates, however, decrease in concentration due to large decreases in emissions in response to instilled policies (van Vuuren et al., 2011; Moss et al., 2010). We chose the RCP8.5 based on evidence that the current trajectory of carbon dioxide emissions continues to follow the most aggressive IPCC projections and surpasses all but the most aggressive emissions scenario (Le Quéré et al., 2009; Ganguly et al., 2009). Projected temperature increases in RCP85 are similar to those predicted by SRES A2 and A1F1, however the rate of the warming in RCP85 is more rapid at the beginning and end of the 21st century, and slower in the years 2035-2080. Between 1950 and 2000, the global average surface temperature increased by ~0.4°C; the RCP85 scenario projects an additional warming of ~1.5°C by 2050 and ~4°C by 2100 (Rogelj et al., 2012).

#### 4.3.2 Teleconnection index and pattern calculation methods

The PNA index is calculated as described in Part I using both the modified linear pointwise method (CPC, 2005) and a rotated principle component analysis (RPCA; Barnston and Livezey, 1987). We utilize the two methods for different aspects of our analyses. The RPCA method is used for the bulk of the analyses, as it is the preferred method by the CPC and we believe this method produces more realistic results, as it accounts for geopotential height variability in the entire Northern

Hemisphere. The modified linear pointwise method is a more straightforward calculation and is less ambiguous during the summer months when the PNA pattern is weaker and more obscure. Thus, the modified linear pointwise method is used when a monthly index value is needed for the entire year.

The time period over which the indices are standardized plays a strong role in the resulting index values. For the historical time period, the CPC defines a climatological base period of 1950-2000 or 1981-2010, depending on the application. In Part I of this study we used 1950-2000 for all historical analyses. In the RCP85 simulation, the effects of global warming increase geopotential heights, which ultimately present biases in the PNA indices when using the 1950-2000 climatology. We therefore standardize the 2050-2100 RCP85 indices using the 2050-2100 climatology. This approach effectively removes the influence and trend of global warming thereby allowing us to focus on any absolute changes that would otherwise be overwhelmed by global warming.

#### 4.3.3 Surface climate analysis methods

We evaluate the relationship between the PNA and surface climate variables using both a correlation analysis and an “extreme event” composite analysis. The correlation analysis is performed similarly to the calculation of the loading pattern maps; however, instead of regressing the index time series on 500-hPa geopotential height anomalies, we use the 2-m surface temperature and precipitation anomalies. This produces a correlation coefficient for each grid cell that defines how well the

fluctuations climate anomalies compare to fluctuations in the PNA index time series. The “extreme event” analysis computes the surface climate composite anomalies for the top and bottom 33% of index values, which produces maps that depict the surface climate changes associated most extreme positive and negative PNA events. These two analysis methods allow us to understand the general relationship between the PNA and climate, and the extent to which this relationship can affect climate changes.

## 4.4 Results and Discussion

### 4.4.1 Temporal variability

The PNA index time series for RCP85 exhibit much more variability than the historical time series (Fig. 4.1). For many models, the quasi-periodicity of the PNA is not captured and the models are locked into either a positive or negative mode for up to decades. The historical NCEP index time series has a mean of  $-0.65 \pm 1.3$  and a positive-to-negative event ratio of 0.162, which indicates that the observed PNA index is more often negative than positive. In Part I of this study we found that, during the 1950-2000 time period, few models produce sufficient negative events and yield ratios of around 1.0, implying a more quasi-periodic index and the inability of some models to capture the naturally occurring noise in the climate system. Index statistics indicate that while most model’s means remain close to zero for all time periods analyzed, the ratio of positive-to-negative events becomes increasingly larger, ranging from 1.529 in Historical and 2.811 in RCP85 (Table 4.1). An increase in the positive-to-negative

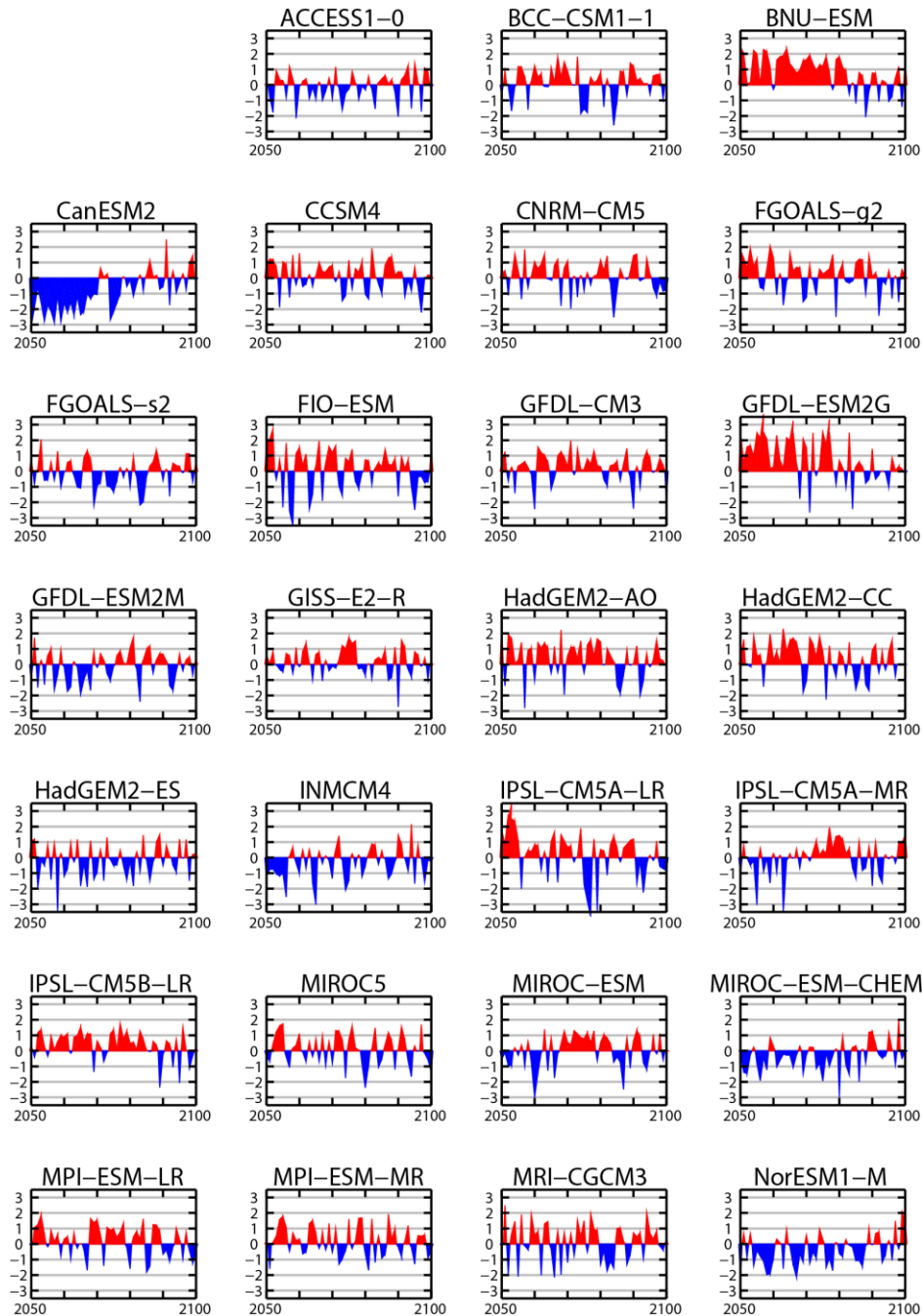


**Figure 4.1** Pacific-North American time series for January 2050-2100, calculated using the RPCA method with respect to the 2050-2100 base period. Shaded red regions indicate positive modes and shaded blue areas indicate negative modes.

**Table 4.1** The mean, standard deviation, and positive-to-negative index area ratio for both future time periods. The CMIP5 model means for each column are displayed.

MODEL	Historical (1950-2000) <sup>1</sup>			RCP85 (2050-2100) <sup>2</sup>		
	Mean	Std Dev	+/- Ratio	Mean	Std Dev	+/- Ratio
NCEP	-0.649	1.296	0.162	--	--	--
ACCESS1-0	0.028	0.993	1.813	-0.139	0.891	0.695
BCC-CSM1.1	0.058	0.951	1.413	0.132	1.012	2.473
BNU-ESM	-0.241	1.077	0.379	0.816	1.087	22.836
CanESM2	-0.193	0.978	0.464	-0.888	1.226	0.060
CCSM4	0.084	1.382	1.327	0.132	0.956	2.159
CNRM-CM5	0.322	0.870	3.990	0.104	0.978	1.879
FGOALS-g2	0.009	0.841	1.252	0.179	1.088	2.521
FGOALS-s2	-0.052	1.040	1.168	-0.108	0.958	0.730
FIO-ESM	-0.274	1.078	0.374	0.098	1.398	1.837
GFDL-CM3	-0.275	1.022	0.280	0.232	0.963	4.383
GFDL-ESM2G	-0.224	1.163	0.545	0.771	1.454	12.267
GFDL-ESM2M	0.217	0.839	4.160	-0.142	0.989	0.729
GISS-E2-R	0.263	0.967	4.284	0.185	0.864	2.453
HadGEM2-AO	0.219	1.030	2.678	0.406	1.181	5.294
HadGEM2-CC	-0.047	1.028	0.792	0.341	1.106	3.750
HadGEM2-ES	-0.065	1.018	0.889	-0.226	1.146	0.425
INM-CM4	0.059	1.116	1.287	-0.363	1.024	0.217
IPSL-CM5A-LR	0.167	0.868	2.495	0.139	1.511	2.129
IPSL-CM5A-MR	-0.028	1.073	1.230	-0.043	1.085	1.094
IPSL-CM5B-LR	0.457	1.193	4.011	0.364	0.878	8.197
MIROC5	0.078	0.980	1.267	0.086	1.004	1.495
MIROC-ESM	-0.044	1.040	0.863	0.013	1.020	1.161
MIROC-ESM-CHEM	0.020	1.257	1.082	-0.375	0.94	0.172
MPI-ESM-LR	-0.162	0.898	0.436	0.215	0.971	2.599
MPI-ESM-MR	0.109	0.963	1.365	0.202	0.981	2.151
MRI-CGCM3	-0.269	1.293	0.578	0.142	1.238	1.729
NorESM1-M	-0.082	0.982	0.849	-0.417	1.009	0.186
<b>MODEL MEAN</b>	<b>0.005</b>	<b>1.035</b>	<b>1.529</b>	<b>0.025</b>	<b>1.037</b>	<b>2.811</b>

<sup>1</sup> All-model mean excludes INM-CM4.

<sup>2</sup> All-model mean excludes GFDL-ESM2G, HadESM2-CC, and IPSL-CM5A-LR.

ratio implies a general increase in the number of positive events, which by the end of the 21<sup>st</sup> century over all the models outnumber the negative events almost 3-to-1 suggesting more persistent meridional flow across North America.

This result is further supported through a two-tailed Student's t-test to examine whether the means of the index time series between time periods are statistically different, and if the means of the CMIP5 model indices are statistically different from that of NCEP (Table 4.2). The null hypothesis of a Student's t-test states that the means of two sample populations (in this case, the two PNA index time series) are the same, or the difference between the means is zero. A low probability value, or "p-value", rejects the null hypothesis and suggests a low probability that the means of the two populations are the same. P-values less than 0.05 or 0.01 indicate that the two sample means are *significantly different* from each other at the 95% or 99% confidence level, respectively. The resulting p-values in Table 4.2 indicate that approximately one-third of the CMIP5 models produce PNA index time series means that are statistically different from NCEP for both the Historical and RCP85 time periods. High p-values that approach 1.0 indicate statistical equivalence and suggest the time series means remain relatively consistent between the two analyzed time periods. Half of the CMIP5 models show no significant differences from NCEP for either time period, ten of which are the same models that display no significant differences between the Historical and RCP85 time periods. We can therefore assume that these ten models have a higher likelihood of producing a consistent PNA pattern through the future simulations.

**Table 4.2** The p-values from a Student's t-test to verify whether the means of the PNA index time series are significantly different from each other. Statistically significant values less than 0.05 (95% confidence interval) are in bold italics.

MODEL	Historical / NCEP	RCP85 / NCEP	Historical / RCP85
ACCESS1-0	0.0598	<b>0.0138</b>	0.5558
BCC-CSM1.1	0.1278	0.2499	0.7052
BNU-ESM	0.5167	0.0629	<b>0.0085</b>
CanESM2	<b>0.0088</b>	<b>6.95E-07</b>	<b>0.0021</b>
CCSM4	0.2399	0.2377	0.8398
CNRM-CM5	<b>0.0010</b>	0.1949	<b>0.0219</b>
FGOALS-g2	0.0692	<b>0.0143</b>	0.3306
FGOALS-s2	0.0513	0.1976	0.4205
FIO-ESM	0.6170	0.0629	0.1349
GFDL-CM3	<b>0.0035</b>	0.4712	<b>0.0114</b>
GFDL-ESM2G	0.4863	0.1512	<b>0.0386</b>
GFDL-ESM2M	0.4081	0.2624	0.6794
GISS-E2-R	<b>0.0034</b>	0.3312	<b>0.0153</b>
HadGEM2-AO	<b>0.0074</b>	<b>0.0012</b>	0.3983
HadGEM2-CC	0.0525	0.8391	<b>0.0704</b>
HadGEM2-ES	<b>0.0429</b>	<b>0.0098</b>	0.4569
INM-CM4	0.0545	<b>0.0010</b>	0.1557
IPSL-CM5A-LR	0.2912	0.3590	0.9068
IPSL-CM5A-MR	0.0686	0.1314	0.7413
IPSL-CM5B-LR	<b>0.0006</b>	0.9067	<b>0.0001</b>
MIROC5	<b>0.0347</b>	<b>0.0335</b>	0.9681
MIROC-ESM	0.0552	0.0931	0.7784
MIROC-ESM-CHEM	0.1339	<b>0.0006</b>	0.0759
MPI-ESM-LR	0.2860	0.4253	0.7783
MPI-ESM-MR	0.1998	0.3947	0.6304
MRI-CGCM3	<b>0.0093</b>	<b>0.0308</b>	0.6140
NorESM1-M	0.1631	<b>0.0004</b>	<b>0.0129</b>

To gain a better understanding of how each model's index time series changes through the 21<sup>st</sup> century, we computed relative frequency distributions for both time periods using the 12-month modified linear pointwise indices and their associated skewness statistics (Fig. 4.2 and Table 4.3). Skewness measures the location of the “mass” of the distribution; positive (negative) skewness indicates that the distribution contains more small (large) values and a longer tail to the right (left) of the peak. For Gaussian distributions, the skewness is zero; the NCEP time series exhibits a skewness of -0.18 indicating that the distribution is close to Gaussian, but slightly negatively skewed. The all-model mean skewness for the Historical and RCP85 periods is -0.3 and -0.43, respectively, indicating that the CMIP5 model distributions generally have a negative skewness. This statistic further supports the notion that most of the models are unable to reproduce enough strong negative PNA events, which persists into RCP85.

Power spectra plots reveal a more specific analysis of periodicity within the index time series (Fig. 4.3). Here the spectra are calculated using the monthly time series produced by the modified linear pointwise method, and therefore direct comparisons with the DJF index time series plots in Figure 4.2 can be misleading. The spectral pattern for NCEP exhibits a seasonal and annual signal with peaks at 2, 3, 7, and 12-24 months. A strong low-frequency signal is present between 3-4 years, a likely connection to ENSO. The CPC states that positive (negative) phase PNA events are often associated with warm (cold) phase ENSO events, which supports the 3-4 year period seen in the NCEP power spectra. The CMIP5 models generally

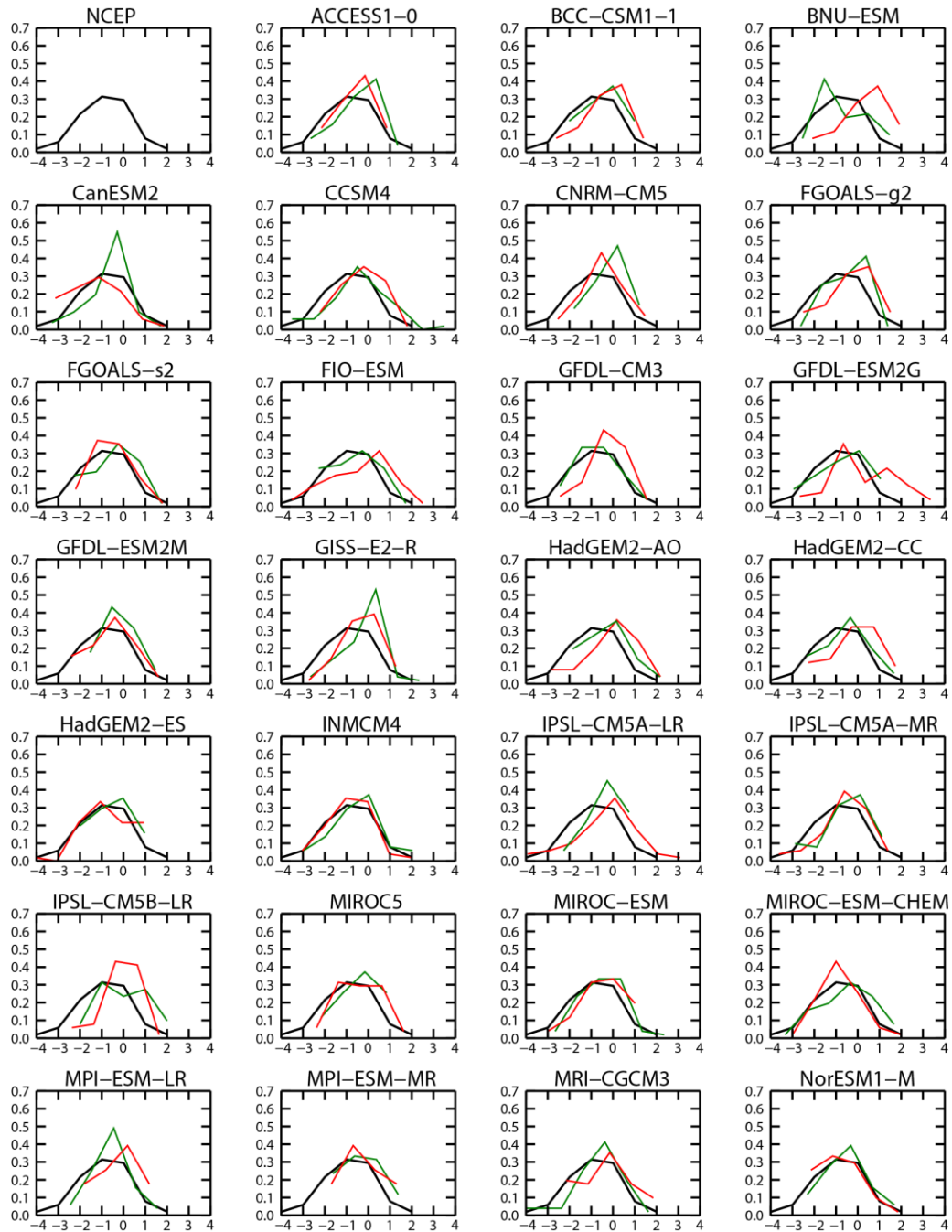


**Figure 4.2** Relative frequency distributions of the DJF PNA index time series for NCEP (1950-2000; black), and CMIP5 historical (1950-2000; green) and RCP85 (2050-2100; red) time periods. The x-axis displays the PNA index value and the y-axis displays relative frequency. Associated skewness values are listed in Table 4.3.

**Table 4.3** Skewness of the NCEP and CMIP5 DJF PNA index time series distributions for the Historical and RCP85 time periods.

MODEL	Historical <sup>1</sup>	RCP85 <sup>2</sup>	RCP85 minus Historical <sup>1,2</sup>
<b>NCEP</b>	<b>-0.18</b>	--	--
ACCESS1-0	-0.99	-0.46	0.52
BCC-CSM1.1	-0.21	-0.70	-0.49
BNU-ESM	0.18	-0.64	-0.82
CanESM2	-0.90	0.32	1.22
CCSM4	-0.26	-0.41	-0.15
CNRM-CM5	-0.43	-0.43	0.00
FGOALS-g2	-0.68	-0.55	0.13
FGOALS-s2	-0.23	-0.16	0.07
FIO-ESM	-0.04	-0.55	-0.51
GFDL-CM3	0.16	-0.91	-1.07
GFDL-ESM2G	-0.45	-0.04	0.41
GFDL-ESM2M	-0.14	-0.30	-0.16
GISS-E2-R	-0.51	-0.60	-0.09
HadGEM2-AO	0.16	-0.74	-0.90
HadGEM2-CC	-0.08	-0.42	-0.34
HadGEM2-ES	-0.01	-0.65	-0.65
INM-CM4	-0.41	-0.14	0.28
IPSL-CM5A-LR	-0.78	-0.63	0.15
IPSL-CM5A-MR	-0.79	-1.01	-0.22
IPSL-CM5B-LR	-0.03	-1.06	-1.03
MIROC5	-0.41	-0.19	0.22
MIROC-ESM	-0.01	-0.73	-0.72
MIROC-ESM-CHEM	-0.14	-0.11	0.03
MPI-ESM-LR	0.00	-0.40	-0.40
MPI-ESM-MR	0.04	0.02	-0.03
MRI-CGCM3	-1.27	-0.25	1.03
NorESM1-M	-0.02	0.33	0.35
<b>All-model mean</b>	<b>-0.30</b>	<b>-0.43</b>	<b>-0.16</b>

<sup>1</sup> All-model mean excludes INM-CM4.

<sup>2</sup> All-model mean excludes GFDL-ESM2G, HadESM2-CC, and IPSL-CM5A-LR.

demonstrate low-frequency dominance, but with some obvious differences from NCEP and between time periods. High and narrow peaks between 1-2 years, as seen with ACCESS1-0 for both time periods, indicate very periodic time series and suggest the model produces too frequent oscillations between positive and negative modes. On the other hand, BNU-ESM and CanESM2 exhibit too much power at longer periods, particularly for RCP85; this is evident by the mode-locking seen in Figure 4.1. While most models demonstrate higher power at lower frequencies, only about a third of the models consistently produce spectral peaks between 3-4 years (e.g., CCSM4, GFDL-ESM2M, and MPI-ESM-MR). Six models show low-frequency peaks that are consistently at frequencies too high, usually around 2-3 years, and about half of the models exhibit frequencies either too high or too low depending on the time period. Stoner et al. (2009) found similar results, stating that biases in model simulations of the PNA related to time series fluctuations may be linked to the inability of these models to reproduce long-term variability in upper-level jet streams. Additionally, due to the relationship between the PNA and ENSO, biases in the periodicity of the PNA pattern imply similar biases in the simulated ENSO patterns, which therefore leads to biases in global climate variability.

#### 4.4.2 Spatial variability

We refer to the three centers of action that characterize the Pacific-North American teleconnection, from west to east, as P1, P2, and P3, and we use these locations to assess the differences in spatial patterns among the CMIP5 models

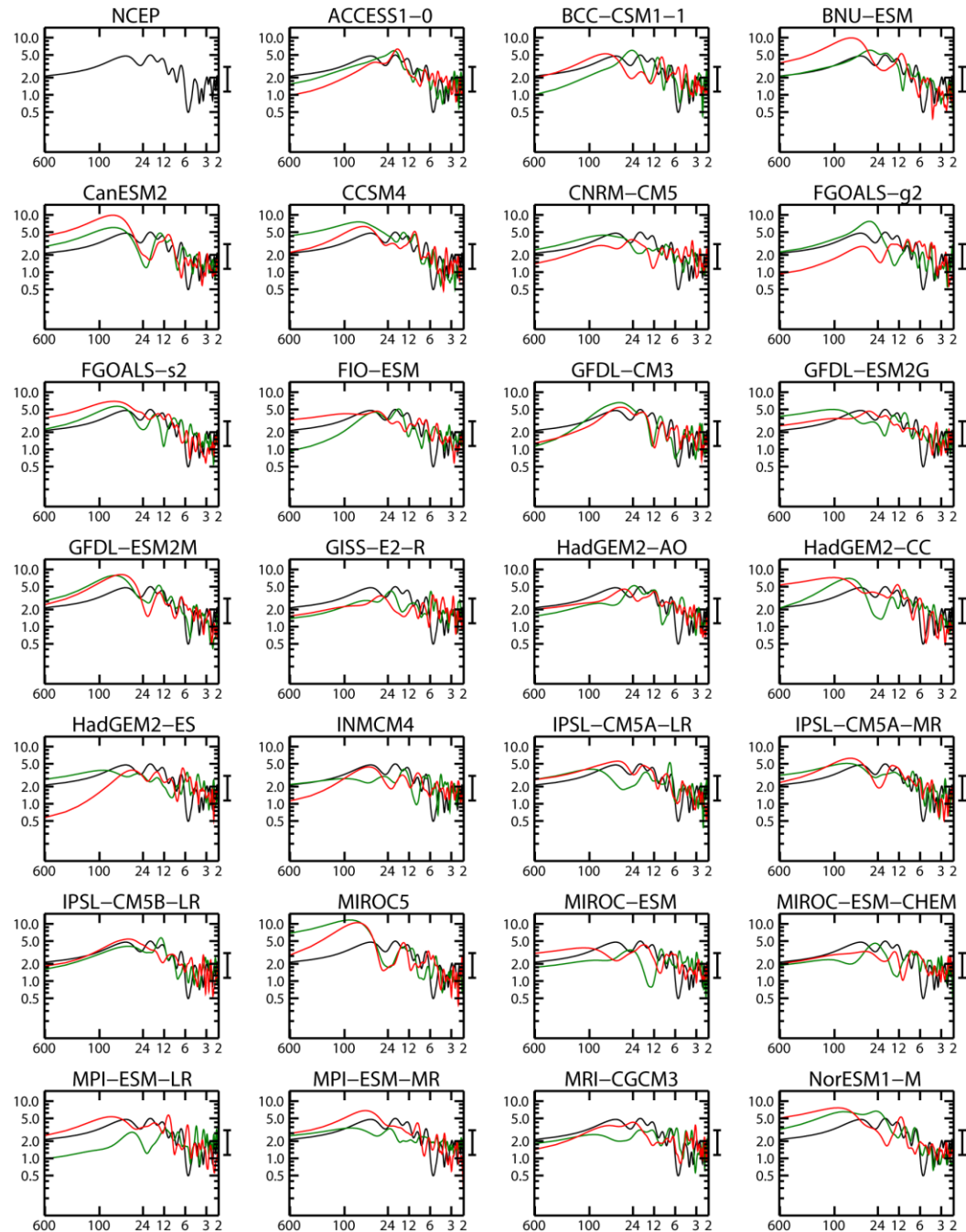


**Figure 4.3** The 12-month smoothed power spectra for NCEP years 1950-2000 (black), and CMIP5 model Historical years 1950-2000 (green) and RCP85 years 2050-2100 (red). The x-axis displays period (months) and the y-axis displays the power of the spectra. The 95% confidence interval is displayed to the right of each plot.

throughout the 21<sup>st</sup> century. Due to the nonlinearity of the Earth's climate system, increasing greenhouse gas concentrations in the RCP scenarios used in the CMIP5 model runs affect future temperatures differently in different parts of the world, with the largest increases in the high northern latitudes. Non-uniform changes in surface and atmospheric temperatures thereby instigate changes in, among other things, large-scale atmospheric dynamics that can ultimately affect the location and strength of the upper-level jets that contribute to variability in the PNA pattern (IPCC, 2007). Thus, understanding how the PNA teleconnection might develop in the future is important for accurately assessing any associated climate changes.

The changes within each model between time periods do not necessarily determine its ability to accurately resolve the PNA pattern, as a model that changes little into the future, but performs poorly based on its historical comparison to NCEP will still inadequately represent the PNA. This statement, however, assumes an unchanging future PNA pattern. Thus, we examine both the future changes within the models, as well as how these changes compare to NCEP. Isolating the changes within the model allows us to understand how individual models evolve into the future, while looking at these changes with respect to the historical NCEP simulation provides a bigger picture regarding the modeled response of the PNA pattern to future climate projections.

Considerable variability exists among the PNA loading patterns for the CMIP5 models between the Historical and RCP85 time periods (Fig. 4.4). For RCP85,

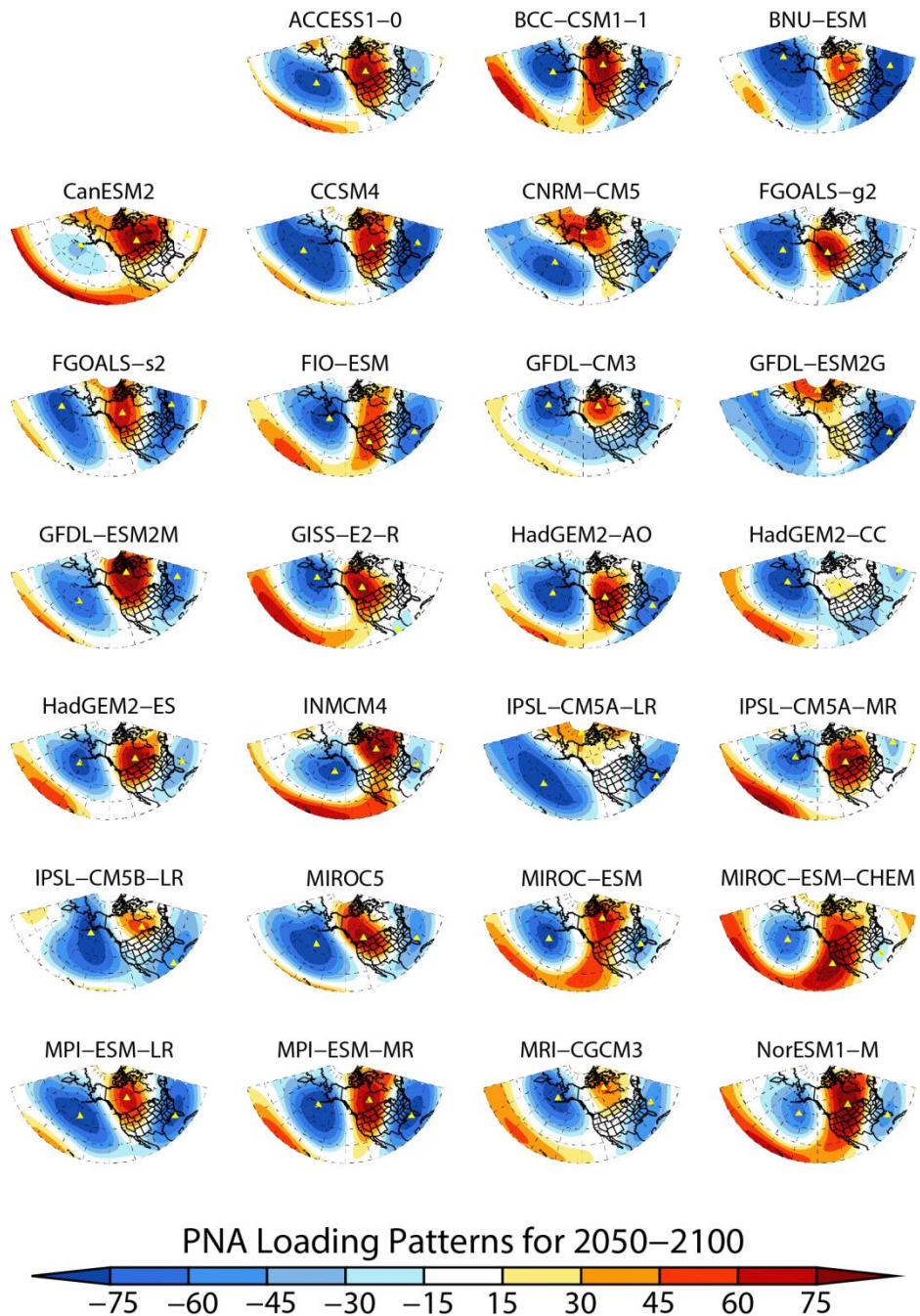


**Figure 4.4** The loading patterns associated with the PNA for each CMIP5 model for RCP85 years 2050–2100. The values represent the temporal correlation ( $R^2 \times 100$ ) between the 500-hPa standardized geopotential height anomalies and the PNA index for the month of January relative to the DJF winter season. The centers P1, P2, and P3 are indicated with yellow triangles on each plot.

**Table 4.4** The rotated-EOF mode and explained variance associated with the PNA teleconnection pattern for each model for the RCP85 future simulation.

<b>MODEL</b>	<b>RCP85</b>	
	Mode	EV (%)
ACCESS1-0	5	5.28
BCC-CSM1.1	4	7.46
BNU-ESM	2	17.48
CanESM2	8	2.79
CCSM4	3	13.12
CNRM-CM5	2	12.93
FGOALS-g2	7	4.21
FGOALS-s2	8	2.86
FIO-ESM	5	6.20
GFDL-CM3	4	7.14
GFDL-ESM2G	2	15.87
GFDL-ESM2M	3	10.59
GISS-E2-R	6	5.59
HadGEM2-AO	8	3.01
HadGEM2-CC	6	4.16
HadGEM2-ES	3	7.37
INM-CM4	8	3.18
IPSL-CM5A-LR	6	3.92
IPSL-CM5A-MR	5	5.11
IPSL-CM5B-LR	9	2.97
MIROC5	9	3.03
MIROC-ESM	8	3.28
MIROC-ESM-CHEM	3	7.94
MPI-ESM-LR	5	7.12
MPI-ESM-MR	3	13.46
MRI-CGCM3	10	2.69
NorESM1-M	3	10.61

GFDL-ESM2G, HadESM2-CC, and IPSL-CM5A-LR fail to produce a recognizable PNA pattern as one of the ten leading rotated EOF modes (rEOF modes and explained variance are listed in Table 4.4); for these models the P2 center is nearly nonexistent and inconsistencies are present at both P1 and P3. While we include these models in the individual analyses, we consider them outliers and consequently do not include them in the all-model means to avoid biasing these values.

#### *4.4.2.1 Center locations*

Compared to the historical simulations analyzed in Part I, the majority of the CMIP5 models reveal shifts in the locations of all three PNA centers for the future time periods (Table 4.5). MPI-ESM-MR shows the smallest changes in the locations of the centers with an average shift of 5.46, while FGOALS-s2 shifted an average of 25.89 degrees including a 33.75-degree westward shift of P1. Longitudinal changes are generally much larger than those for latitude; the models exhibit a 4-degree westward shift of P1 accompanied by a 2.5-degree westward shift of P2, and a nearly 9-degree eastward shift of P3. These changes in location imply a widening of the wave field over the North Pacific and North America, which is indicative weaker energy propagation and increasing eddy length scales under global warming (Kidston et al., 2010).

The locations of the RCP85 centers relative to NCEP follow a similar pattern as seen in the Historical analysis; the modeled P1 and P2 centers are located to the east

**Table 4.5** The longitudinal ( $\Delta\text{lon}$ ) and latitudinal ( $\Delta\text{lat}$ ) shift in location of P1, P2, and P3 in degrees for each CMIP5 model between the Historical and RCP85 time periods (calculated as (RCP85 minus Historical)). The vector distances for each center were calculated and used to compute an “average shift”. The ranking is based on the average distance and indicates the models that shifted the least (Rank=1) and the most (Rank=27).

Model	P1		P2		P3		Average Shift	Rank
	$\Delta\text{lon}$	$\Delta\text{lat}$	$\Delta\text{lon}$	$\Delta\text{lat}$	$\Delta\text{lon}$	$\Delta\text{lat}$		
<b>ACCESS1-0</b>	15.00	-15.00	-1.88	-5.00	22.50	3.75	16.45	19
<b>BCC-CSM1.1</b>	-5.63	0.00	11.25	16.74	16.88	11.16	15.34	18
<b>BNU-ESM</b>	-25.31	8.37	0.00	2.79	19.69	8.37	16.95	20
<b>CanESM2</b>	-11.25	2.79	0.00	-2.79	8.44	2.79	7.76	6
<b>CCSM4</b>	-20.00	0.94	1.25	0.94	-5.00	0.00	8.86	8
<b>CNRM-CM5</b>	-1.41	-5.60	-22.50	9.81	0.00	-1.40	10.57	10
<b>FGOALS-g2</b>	2.81	-8.37	-5.63	-2.79	-2.81	-5.58	7.12	4
<b>FGOALS-s2</b>	-33.75	-3.32	-25.31	3.32	14.06	11.61	25.89	27
<b>FIO-ESM</b>	5.63	2.79	-19.69	-16.74	5.63	2.79	12.80	16
<b>GFDL-CM3</b>	0.00	-4.00	2.50	0.00	30.00	6.00	12.36	14
<b>GFDL-ESM2G *</b>	12.50	-14.16	-27.50	22.25	15.00	0.00	23.09	26
<b>GFDL-ESM2M</b>	-5.00	-2.02	5.00	10.11	17.50	10.11	12.30	13
<b>GISS-E2-R</b>	2.50	14.00	22.50	-16.00	-7.50	-8.00	17.60	22
<b>HadGEM2-AO</b>	-13.13	0.00	-11.25	-5.00	-16.88	-3.75	14.24	17
<b>HadGEM2-CC *</b>	-3.75	5.00	1.88	-3.75	41.25	1.25	17.24	21
<b>HadGEM2-ES</b>	-15.00	3.75	0.00	-2.50	18.75	5.00	12.46	15
<b>INM-CM4</b>	26.00	-12.00	20.00	24.00	4.00	3.00	21.63	25
<b>IPSL-CM5A-LR *</b>	15.00	-7.58	-15.00	13.26	22.50	1.89	19.80	24
<b>IPSL-CM5A-MR</b>	5.00	-2.54	0.00	-3.80	7.50	5.07	6.15	3
<b>IPSL-CM5B-LR</b>	0.00	13.26	7.50	-3.79	-3.75	0.00	8.47	7
<b>MIROC5</b>	2.81	-5.60	0.00	-4.20	11.25	4.20	7.49	5
<b>MIROC-ESM</b>	-8.44	5.58	8.44	13.95	2.81	8.37	11.75	12
<b>MIROC-ESM-CHEM</b>	14.06	0.00	-11.25	-22.32	14.06	2.79	17.80	23
<b>MPI-ESM-LR</b>	5.63	-5.60	1.88	1.87	-13.13	-9.33	8.89	9
<b>MPI-ESM-MR</b>	1.88	1.87	9.38	1.87	-3.75	-1.87	5.46	1
<b>MRI-CGCM3 *</b>	-12.38	1.12	-4.50	6.73	-13.50	4.49	11.58	11
<b>NorESM1-M</b>	5.00	-3.79	5.00	-7.58	2.50	0.00	5.95	2
<b>All-model mean</b>	<b>-3.96</b>	<b>-0.06</b>	<b>-2.54</b>	<b>0.03</b>	<b>8.70</b>	<b>2.21</b>	<b>11.92</b>	--

\* Models excluded from the all-model means.

**Table 4.6** As in Table 4.5, for the difference between NCEP and RCP85 (calculated as (RCP85 minus NCEP)).

<b>Model</b>	<b>P1</b>		<b>P2</b>		<b>P3</b>		<b>Average Distance</b>	<b>Rank</b>
	$\Delta\text{lon}$	$\Delta\text{lat}$	$\Delta\text{lon}$	$\Delta\text{lat}$	$\Delta\text{lon}$	$\Delta\text{lat}$		
<b>NCEP</b>	<b>192.50</b>	<b>47.50</b>	<b>245.00</b>	<b>52.50</b>	<b>272.50</b>	<b>32.50</b>	--	--
<b>ACCESS1-0</b>	3.44	-1.88	7.19	3.13	13.44	0.63	8.40	7
<b>BCC-CSM1.1</b>	-4.06	4.13	10.94	7.50	0.31	-0.41	6.52	4
<b>BNU-ESM</b>	-20.94	9.71	13.75	4.71	17.19	-0.41	18.27	25
<b>CanESM2</b>	-1.25	4.13	16.56	1.92	20.00	-3.20	13.75	15
<b>CCSM4</b>	-8.75	-4.62	11.25	-2.08	13.75	-1.87	11.74	12
<b>CNRM-CM5</b>	10.00	-11.78	-18.59	15.44	-1.09	-9.39	16.36	22
<b>FGOALS-g2</b>	-4.06	-1.46	-8.75	-0.87	-19.38	-8.78	11.46	10
<b>FGOALS-s2</b>	-23.75	-0.22	-0.31	6.39	17.19	6.49	16.17	21
<b>FIO-ESM</b>	12.81	6.92	-0.31	-14.83	3.13	-5.99	12.05	13
<b>GFDL-CM3</b>	-16.25	7.50	6.25	10.50	18.75	6.50	16.65	23
<b>GFDL-ESM2G *</b>	8.75	-12.11	-18.75	25.37	3.75	-7.22	18.21	24
<b>GFDL-ESM2M</b>	3.75	-4.02	13.75	13.23	18.75	2.89	14.52	16
<b>GISS-E2-R</b>	-10.00	10.50	2.50	3.50	-15.00	-10.50	12.37	14
<b>HadGEM2-AO</b>	-0.31	0.63	3.44	-4.38	2.19	-6.88	4.49	1
<b>HadGEM2-CC *</b>	-7.81	6.88	7.19	3.13	26.56	-3.13	15.00	18
<b>HadGEM2-ES</b>	-0.31	1.88	12.81	0.63	11.56	-3.13	8.90	8
<b>INM-CM4</b>	21.50	1.25	25.00	3.75	9.50	-3.25	18.95	27
<b>IPSL-CM5A-LR *</b>	2.50	-12.45	-20.00	26.13	5.00	-8.82	18.58	26
<b>IPSL-CM5A-MR</b>	2.50	8.27	12.50	-1.80	25.00	0.46	15.43	20
<b>IPSL-CM5B-LR</b>	10.00	6.50	21.25	-0.39	-6.25	-10.71	15.19	19
<b>MIROC5</b>	4.38	-3.38	1.09	-1.37	8.75	-3.78	5.60	2
<b>MIROC-ESM</b>	-1.25	-1.46	16.56	10.29	0.31	-0.41	7.31	6
<b>MIROC-ESM-CHEM</b>	1.56	-1.46	-8.75	-17.62	-2.50	-5.99	9.43	9
<b>MPI-ESM-LR</b>	4.38	-3.67	6.25	6.26	3.13	-3.59	6.44	3
<b>MPI-ESM-MR</b>	0.63	3.79	11.88	2.52	3.13	-3.59	6.91	5
<b>MRI-CGCM3</b>	-0.13	9.14	20.50	10.86	12.13	-0.54	14.82	17
<b>NorESM1-M</b>	12.50	0.82	15.00	-2.29	5.00	-5.03	11.60	11
<b>All-model mean</b>	<b>-0.15</b>	<b>1.72</b>	<b>7.99</b>	<b>2.29</b>	<b>6.62</b>	<b>-2.94</b>	<b>13.74</b>	--

\* Models excluded from the all-model means.

and north of the locations determined by NCEP, while the average locations of P3 are generally east and south of NCEP (Table 4.6). The overall differences in latitude are smaller than those in longitude, yet the differences between NCEP and the Historical simulations are generally larger than those between NCEP and RCP85. This suggests that the average model spatial representation of the PNA pattern remains relatively consistent throughout the future simulations. This finding is further supported by plots of the P1, P2, and P3 center coordinates (Fig. 4.5). P2 exhibits the largest amount of variability between time periods, yet also contains the highest number of outliers, which cause the large spreads in both the Historical and RCP85 plots. P1 exhibits most amount of longitudinal variability (33-45 degrees), while P3 displays the least amount of latitudinal variability (15-20 degrees). P3 also exhibits the most consistent orientation, with the points aligning to a distinct southwest-northeast arrangement.

More than half of the models demonstrate a northward shift in at least one of the centers by the end of the 21<sup>st</sup> century in addition to a widening of the overall P1-to-P3 spread (Fig. 4.6 and Table 4.5). Chase et al. (2000) found that anthropogenic land cover changes, such as those consistent with current climate changes, contribute to a poleward shift in the mid-latitude jet streams as a result of reduced outflow from the Hadley Cell. An overall decrease in the strength of the jet core was also observed, particularly over the North Pacific. Kidston et al. (2011) found a poleward shift of the mid-latitude jets under a warming climate as a result of increases in the eddy length scale. Using a simplified GCM, they found that large eddy length scales lead to a

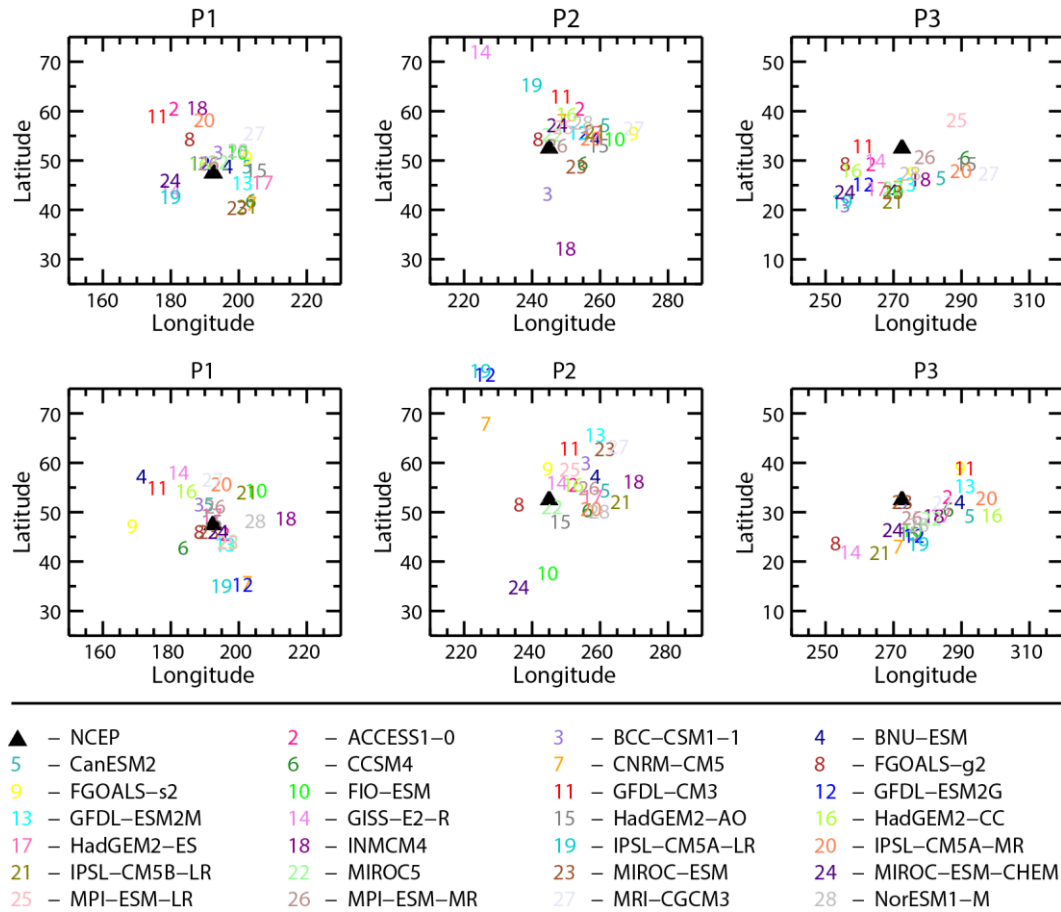


**Figure 4.5** The spatial distribution of each center P1, P2, and P3, for each model (color-coded numbers) for the Historical (top) and RCP85 (bottom) time periods. Black lines show the best-fit linear trend associated with the model center coordinates, indicating the orientation of the distribution. The Historical NCEP centers are indicated with black triangles on each plot.

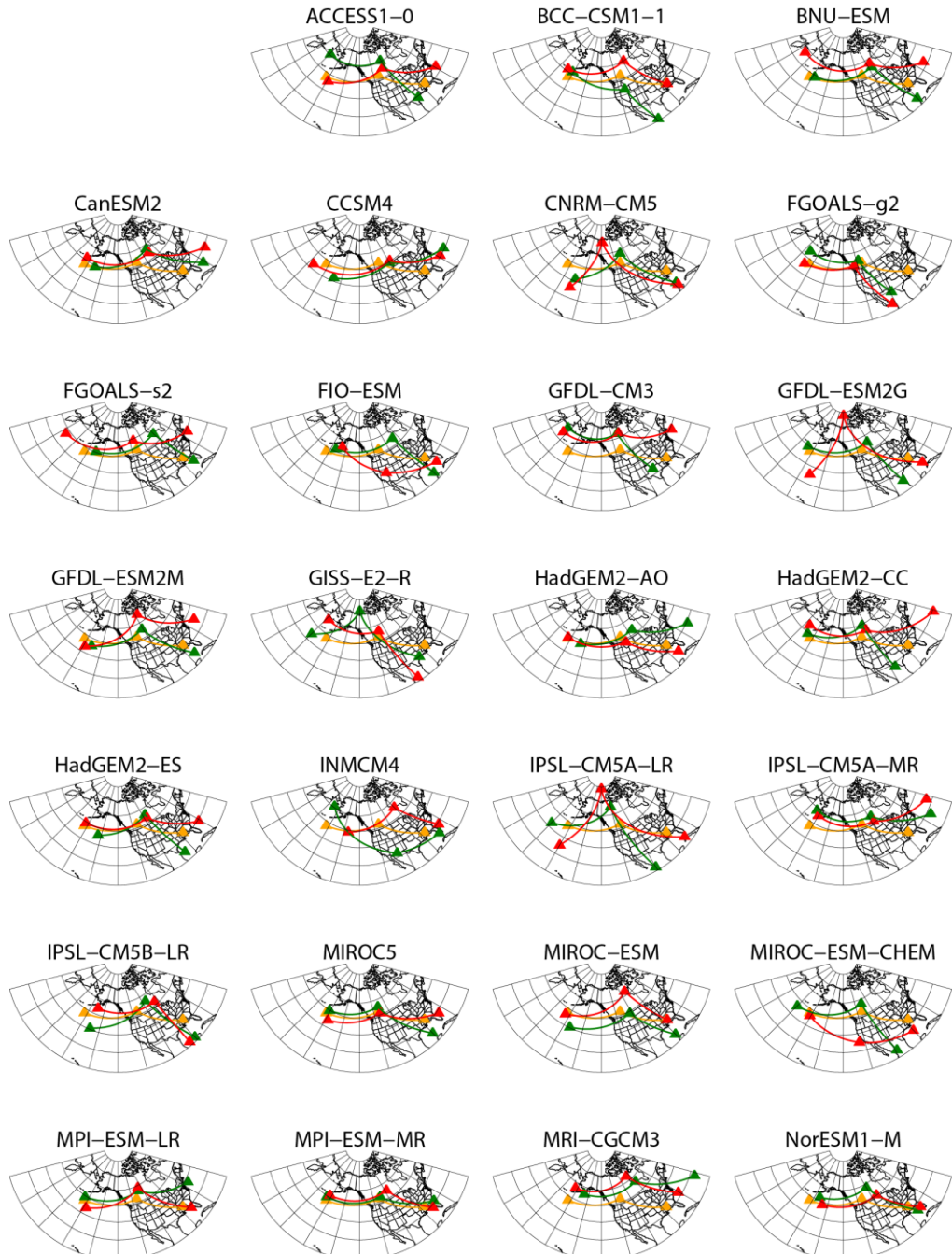


**Figure 4.6** The mapped spatial distribution of each center P1, P2, and P3, for the historical (green) and RCP85 (red). Lines connect each center for better visual interpretation, but have no physical meaning. For reference, the NCEP historical centers are plotted on each map in orange.

dampening of the upper-atmosphere wave field, and can cause a poleward shift in the location of the eddy-driven jet stream on the order of 2-2.5° in the Southern Hemisphere and slightly smaller in the Northern Hemisphere. As such, due to the relationship between the structure of the PNA and fluctuations in the mid-latitude jet stream, a northward shift of the pattern is plausible under future climate projections.

#### *4.4.2.2 Center magnitudes*

By definition, the PNA loading pattern depends on the 500-hPa geopotential height anomalies. For a positive phase PNA loading pattern (as displayed in Fig. 4.4), the P1 and P3 centers associate with negative anomalies and the P2 center associates with positive anomalies. The “strength” of an anomaly refers to its magnitude, thus an increase in the strength of a negative (positive) anomaly refers to a more negative (more positive) value. We refer to the “center strength” as the magnitude of the anomaly at each of the P1, P2, and P3 centers.

On average, the strength of the three pattern centers weakens by the end of the century (Fig. 4.7 and Table 4.7). Excluding those models that do not resolve a PNA pattern, by the end of the 21<sup>st</sup> century the average net changes for P1, P2, and P3 are -4.5 m, -2.51 m, and -4.46 m, respectively, and exhibit no statistical significance. Based on the absolute value of the average differences listed in Table 4.7, IPSL-CM5A-MR shows the least amount of change in the average strength of the centers of only 0.11 m, whereas MRI-CGCM3 exhibits the largest change with a decrease in strength of -25.92 m. Eleven models exhibit an increase in average center anomaly

strength, yet only four models show an average increase of >10 m (e.g., FGOALS-g2 and FIO-ESM). The remaining 16 models display an average decrease in strength; however, only five models decrease by >10 m (CCSM4 and MIROC-ESM-CHEM).

In Part I of this study we found that most of the models underestimated the strength of the anomalies for all three centers relative to NCEP. The largest discrepancies are at P2 with the average anomaly 24 m weaker than NCEP. The average anomaly strengths remain substantially weaker than NCEP at the end of the 21<sup>st</sup> century (Table 4.8). Only four models display average differences <10 m (GFDL-ESM2G and IPSL-CM5A-LR are excluded), while 10 models show differences >20 m (HadGEM2-CC is excluded).

#### 4.5 Model performance

We developed an index (SSI) in Part I to diagnose a model's ability to reproduce the shift in flow patterns, or "see-saw", between meridional and zonal flows. We found that the spatial variability in the western half of the PNA sector is attributed both to the latitudinal separation and difference in magnitude of P1 and P2. The NCEP Historical analysis indicates that P1 and P2 are located within 5 degrees latitude of each other and are relatively close in magnitude. If the latitudinal difference between P1 and P2 is too large, the blocking wave structure is over-amplified during positive PNA phases and the flow is too meridional during negative

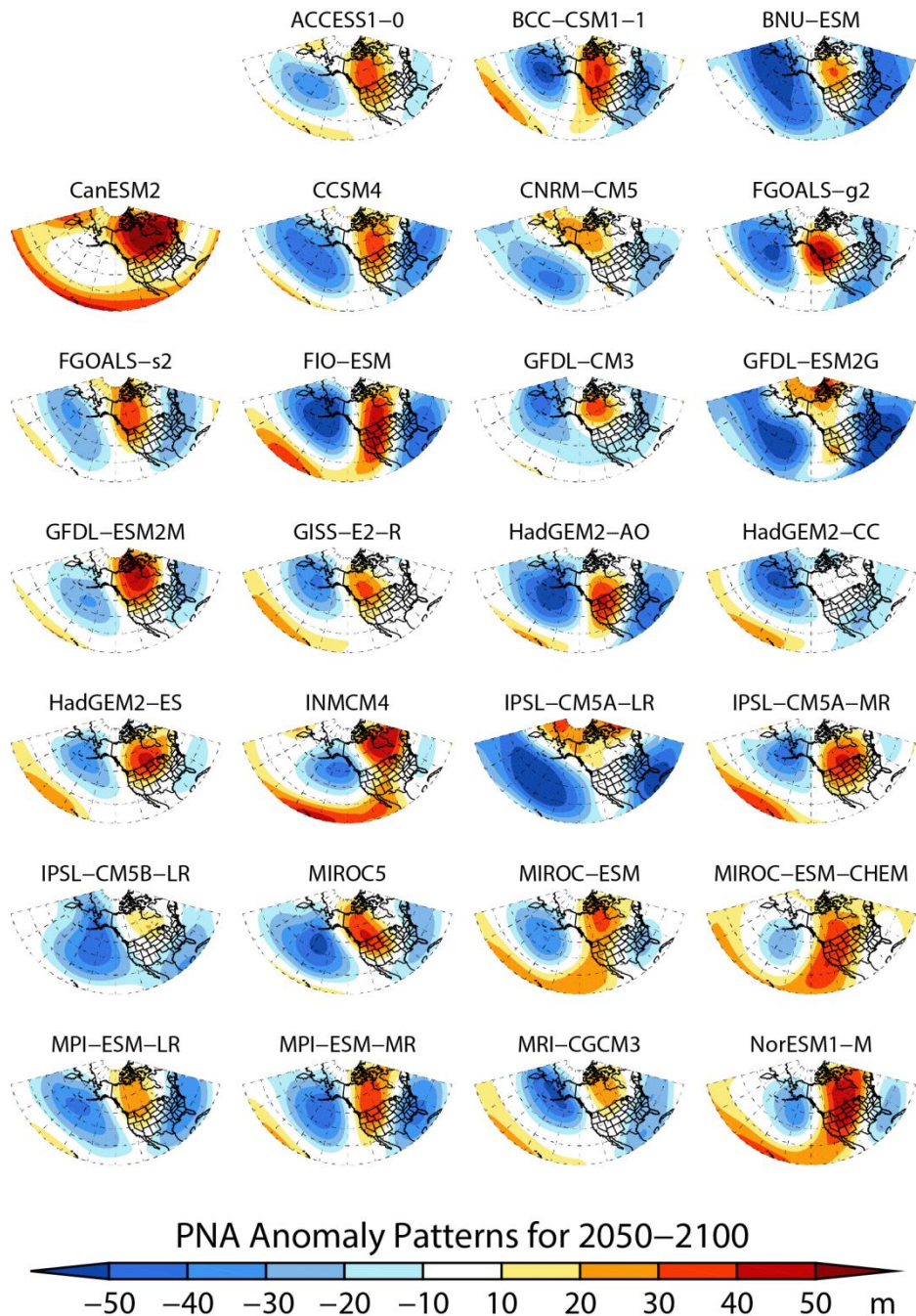


**Figure 4.7** The PNA teleconnection loading pattern as defined by the projection of the PNA index time series for each model onto the 500-hPa geopotential height anomaly field used to calculate the index for all Januaries from 1950-2000. The January anomalies are relative to the DJF winter season. The values displayed are in meters represent the strength of the anomalies associated with the PNA pattern at each grid point.

**Table 4.7** The P1, P2, and P3 center anomaly differences, in meters, between the Historical and RCP85 time periods (calculated as (RCP85 minus Historical)). The values are calculated using the absolute values of the center anomalies so that the magnitude of the differences are respective to zero; a negative (positive) difference corresponds to a weaker (stronger) absolute anomaly (e.g., a value of -15.50 m at P1 for ACCESS1-0 indicates that the magnitude of the anomaly center for RCP85-1 is *weaker* than the magnitude for the Historical time period). The rank is based on the absolute value of the average difference.

MODEL	P1	P2	P3	Average Difference	Rank
ACCESS1-0	-15.50	4.50	-6.63	-5.88	12
BCC-CSM1.1	8.85	0.58	3.72	4.38	10
BNU-ESM	11.41	-12.45	13.65	4.20	8
CanESM2	-35.37	13.73	-21.15	-14.26	22
CCSM4	-17.55	-27.04	-20.87	-21.82	26
CNRM-CM5	-7.82	-13.31	-9.51	-10.21	19
FGOALS-g2	15.86	19.05	12.89	15.93	23
FGOALS-s2	-18.35	-3.09	-2.06	-7.84	17
FIO-ESM	23.03	-2.34	15.38	12.02	21
GFDL-CM3	-5.98	3.56	-2.67	-1.70	4
GFDL-ESM2G *	4.90	-17.29	35.54	7.72	16
GFDL-ESM2M	-8.90	24.81	-3.64	4.09	7
GISS-E2-R	9.78	-13.10	-14.69	-6.01	13
HadGEM2-AO	3.05	1.57	8.45	4.36	9
HadGEM2-CC *	-0.78	-15.32	-13.12	-9.74	18
HadGEM2-ES	-8.33	2.93	-0.97	-2.12	6
INM-CM4 *	12.45	23.84	-2.13	11.38	20
IPSL-CM5A-LR *	31.13	-8.77	34.48	18.95	25
IPSL-CM5A-MR	11.10	-3.74	-7.02	0.11	1
IPSL-CM5B-LR	-6.16	-8.49	-7.57	-7.41	15
MIROC5	8.58	-3.38	-3.54	0.55	2
MIROC-ESM	-11.40	6.90	-9.32	-4.61	11
MIROC-ESM-CHEM	-35.98	15.63	-27.57	-15.97	24
MPI-ESM-LR	10.26	-21.29	6.08	-1.65	3
MPI-ESM-MR	1.56	-8.35	0.98	-1.94	5
MRI-CGCM3	-28.34	-38.95	-10.49	-25.92	27
NorESM1-M	-7.25	4.44	-16.12	-6.31	14
All-model mean	<b>-4.50</b>	<b>-2.51</b>	<b>-4.46</b>	<b>-3.83</b>	--

\* Models excluded from the all-model means.

**Table 4.8** As in Table 4.7, for the difference between NCEP and RCP85 (calculated as (RCP85 minus NCEP)).

MODEL	P1	P2	P3	Average Difference	Rank
<b>NCEP</b>	<b>-60.29</b>	<b>65.34</b>	<b>-41.78</b>	--	--
ACCESS1-0	-24.31	-26.36	-27.81	-26.16	23
BCC-CSM1.1	-4.95	-24.03	-5.17	-11.38	7
BNU-ESM	2.04	-34.04	7.05	-8.32	5
CanESM2	-52.64	-2.27	-38.10	-31.00	27
CCSM4	-14.22	-31.17	1.82	-14.52	9
CNRM-CM5	-23.53	-36.23	-11.77	-23.84	22
FGOALS-g2	-8.21	-12.24	-6.44	-8.96	6
FGOALS-s2	-27.93	-29.24	-14.03	-23.73	21
FIO-ESM	8.47	-18.16	7.24	-0.82	2
GFDL-CM3	-14.75	-27.46	-14.84	-19.02	15
GFDL-ESM2G *	-1.80	-30.92	31.02	-0.57	1
GFDL-ESM2M	-29.02	-14.45	-13.47	-18.98	14
GISS-E2-R	-18.04	-31.57	-32.71	-27.44	25
HadGEM2-AO	-1.20	-23.59	4.68	-6.70	4
HadGEM2-CC *	-6.00	-57.63	-18.65	-27.43	24
HadGEM2-ES	-22.49	-21.75	-24.49	-22.91	20
INM-CM4	-12.64	-15.48	-27.32	-18.48	13
IPSL-CM5A-LR *	8.37	-43.03	17.63	-5.68	3
IPSL-CM5A-MR	-13.01	-23.08	-25.05	-20.38	17
IPSL-CM5B-LR	-10.69	-45.21	-10.32	-22.07	19
MIROC5	-4.93	-23.55	-15.70	-14.73	10
MIROC-ESM	-19.98	-30.88	-14.55	-21.81	18
MIROC-ESM-CHEM	-32.04	-24.73	-33.66	-30.14	26
MPI-ESM-LR	-17.70	-36.45	-4.06	-19.41	16
MPI-ESM-MR	-12.89	-26.65	0.24	-13.10	8
MRI-CGCM3	-7.93	-36.09	-11.34	-18.45	12
NorESM1-M	-22.33	-14.82	-15.19	-17.45	11
<b>All-model mean</b>	<b>-16.04</b>	<b>-25.40</b>	<b>-13.54</b>	<b>-18.33</b>	--

\* Models excluded from the all-model means.

phases. On the other hand, a discrepancy between the strengths of P1 and P2 can lead to a dampening of the wave structure during positive phases. We define the SSI as:

$$SSI = D_{model} - D_{NCEP}, \text{ where}$$

$$D = (P2_{lat} - P1_{lat}) - (P2_{mag} - P1_{mag}).$$

The “lat” and “mag” subscripts refer to the latitude coordinate and magnitude of the anomaly, respectively, for P1 and P2. The SSI is intended to quantify a model’s ability to reproduce the flow see-saw, and we assume that SSI values between 0 and 10 provide more realistic representations of the PNA spatial structure over the North Pacific and western North America. Models with index values between 10 and 20 only partially reproduce the shift in flow patterns, and models with index values  $\geq 20$  do not reproduce the shift.

The average SSI values remain little changed between the two time periods (16.76 for Historical and 17.32 for RCP85) and the changes are not statistically significant (Table 4.9). Based on the definition of the SSI, these numbers imply that the flow see-saw in the CMIP5 models is generally poorly represented regardless of the time period considered. Similar to the Historical analysis, the number of models with SSI values  $< 10$ , between 10 and 20, and  $\geq 20$  are about the same for RCP85. The index time series analysis revealed an increase in the number of positive PNA events compared to the number of negative events (Table 4.1); positive PNA events are characterized by meridional flow, and high average SSI values are therefore consistent with the increase in positive events.

**Table 4.9** The see-saw index (SSI) for the Historical and RCP85 time periods.

Model	Historical <sup>1</sup>	RCP85-2 <sup>2</sup>	Average <sup>1,2</sup>	Rank
<b>ACCESS1-0</b>	17.06	7.05	12.06	8
<b>BCC-CSM1.1</b>	2.56	22.45	12.51	11
<b>BNU-ESM</b>	12.81	31.09	21.95	19
<b>CanESM2</b>	2.11	52.57	27.34	20
<b>CCSM4</b>	10.01	19.50	14.76	14
<b>CNRM-CM5</b>	19.02	39.92	29.47	22
<b>FGOALS-g2</b>	2.22	4.62	3.42	2
<b>FGOALS-s2</b>	16.55	7.93	12.24	9
<b>FIO-ESM</b>	0.95	4.89	2.92	1
<b>GFDL-CM3</b>	21.26	15.72	18.49	15
<b>GFDL-ESM2G</b>	8.00	66.60	37.30	25
<b>GFDL-ESM2M</b>	24.26	2.69	13.48	12
<b>GISS-E2-R</b>	13.65	6.54	10.10	7
<b>HadGEM2-AO</b>	20.91	17.39	19.15	16
<b>HadGEM2-CC</b>	42.10	47.89	45.00	26
<b>HadGEM2-ES</b>	15.52	1.98	8.75	6
<b>INM-CM4</b>	19.27	5.34	12.31	10
<b>IPSL-CM5A-LR</b>	29.24	89.99	59.62	27
<b>IPSL-CM5A-MR</b>	13.57	0.01	6.79	3
<b>IPSL-CM5B-LR</b>	42.35	27.63	34.99	23
<b>MIROC5</b>	7.26	20.62	13.94	13
<b>MIROC-ESM</b>	32.57	22.65	27.61	21
<b>MIROC-ESM-CHEM</b>	50.46	23.47	36.97	24
<b>MPI-ESM-LR</b>	10.34	28.67	19.51	17
<b>MPI-ESM-MR</b>	2.58	12.50	7.54	4
<b>MRI-CGCM3</b>	13.67	29.90	21.79	18
<b>NorESM1-M</b>	4.86	10.62	7.74	5
<b>All-model mean</b>	<b>16.76</b>	<b>17.32</b>	<b>16.44</b>	--

<sup>1</sup> All-model mean excludes INM-CM4.<sup>2</sup> All-model mean excludes GFDL-ESM2G, HadESM2-CC, and IPSL-CM5A-LR.

The 500-hPa surface contour, or “isohypse”, maps show spatial representations of these SSI values (Fig. 4.8). Models with higher SSI values (e.g., CNRM-CM5 and GFDL-CM3) reveal contours with little or no difference for positive and negative PNA modes, and as a result these models present substantial biases in the periodicity of their PNA index time series because they are locked into either a positive or negative mode for up to a decade at a time (Fig. 4.1). Models with lower indices (e.g., HadGEM2-ES and FIO-ESM) more accurately reproduce the PNA pattern with ridged flow during positive modes and zonal flow during negative modes.

A “Difference Factor” (DF), the sum of the average location differences and the average magnitude differences relative to NCEP (Tables 4.6 and 4.8), includes the influence of all three centers, and provides a general assessment of overall model performance with respect to spatial variability (Table 4.10). Models with DF values closer to zero better represent the spatial PNA pattern (e.g., FIO-ESM, GFDL-ESM2M, and MPI-ESM-MR). The sum of the SSI and DF produces a ranking value that combines center location, anomaly strength, and the ability to reproduce distinct meridional and zonal flow patterns (Table 4.11). The lowest rankings (highest ranking value) are associated with those models that failed to produce a recognizable PNA pattern in one of the analyzed time periods, resulting in spatial differences that far outweigh the other models (e.g., HadGEM-CC, GFDL-ESM2G, and IPSL-CM5A-LR), while FIO-ESM, IPSL-CM5A-MR, and FGOALS-s2 show the highest rankings (lowest ranking value) and provide the most consistent analyses of the PNA relative to the parameters defined by NCEP.

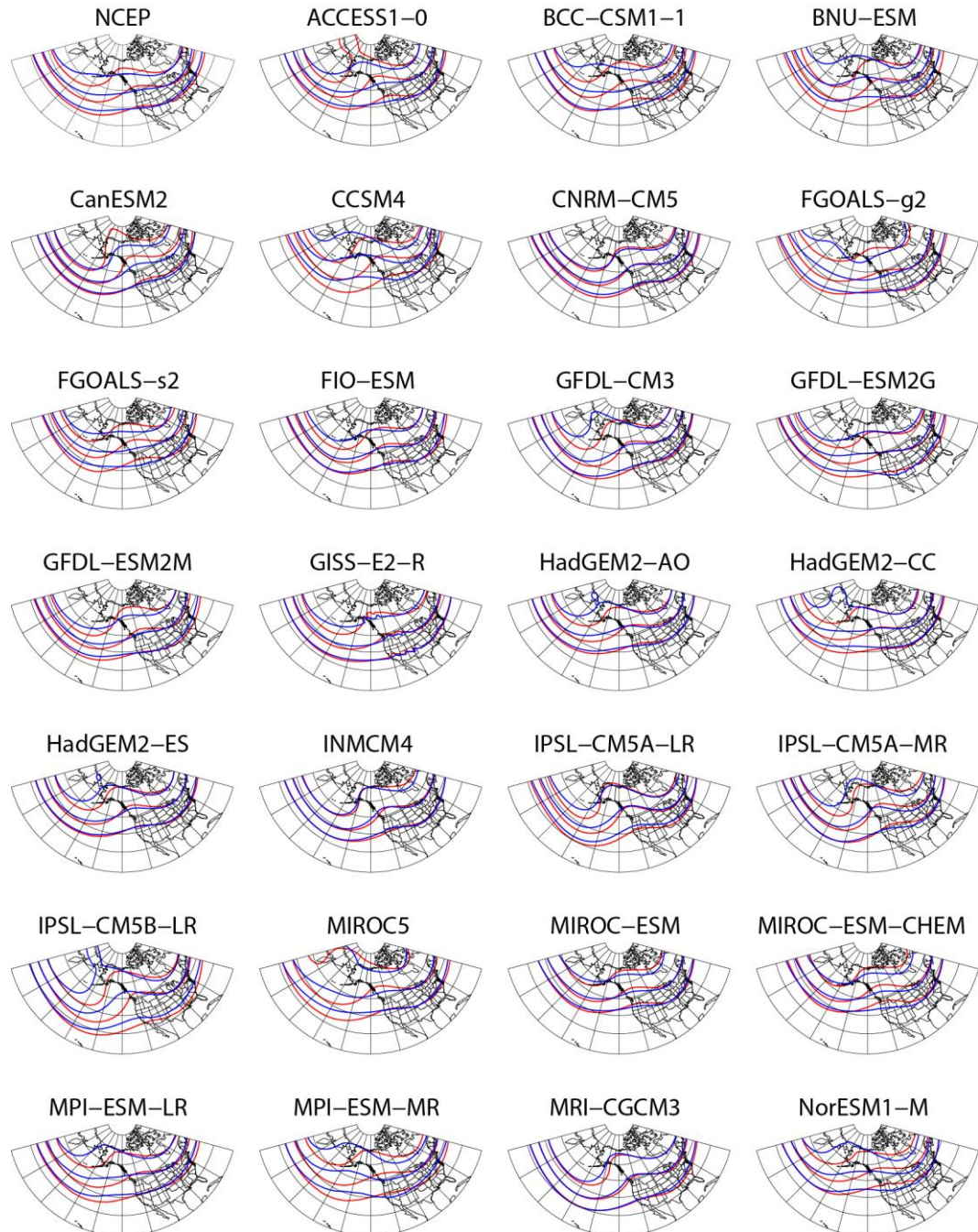


**Figure 4.8** 500-hPa isohypses for positive (greater than 0.5; red lines) and negative (less than -0.5; blue lines) PNA indices for 2050-2100. The northernmost contours are for the 5280-m isohypse, the middle contours are for the 5460 m isohypse, and the southernmost contours are for the 5640 m isohypse.

**Table 4.10** The difference factor (DF) for the Historical and RCP85 time periods.

Model	Historical <sup>1</sup>	RCP85-2 <sup>2</sup>	Average <sup>1,2</sup>	Rank
<b>ACCESS1-0</b>	33.36	15.05	24.21	9
<b>BCC-CSM1.1</b>	27.05	38.45	32.75	16
<b>BNU-ESM</b>	21.71	53.09	37.40	20
<b>CanESM2</b>	30.18	77.57	53.88	25
<b>CCSM4</b>	21.24	33.50	27.37	11
<b>CNRM-CM5</b>	22.93	62.92	42.92	23
<b>FGOALS-g2</b>	34.99	8.62	21.80	7
<b>FGOALS-s2</b>	29.79	16.93	23.36	8
<b>FIO-ESM</b>	25.14	9.89	17.52	1
<b>GFDL-CM3</b>	31.43	27.72	29.57	15
<b>GFDL-ESM2G</b>	17.26	92.60	54.93	26
<b>GFDL-ESM2M</b>	31.60	5.69	18.64	3
<b>GISS-E2-R</b>	37.71	13.54	25.62	10
<b>HadGEM2-AO</b>	26.67	30.39	28.53	14
<b>HadGEM2-CC</b>	27.18	71.89	49.53	24
<b>HadGEM2-ES</b>	33.73	3.98	18.86	4
<b>INM-CM4</b>	44.26	11.34	27.80	12
<b>IPSL-CM5A-LR</b>	40.54	116.99	78.76	27
<b>IPSL-CM5A-MR</b>	34.44	1.01	17.73	2
<b>IPSL-CM5B-LR</b>	27.08	46.63	36.85	19
<b>MIROC5</b>	19.99	35.62	27.81	13
<b>MIROC-ESM</b>	26.57	39.65	33.11	17
<b>MIROC-ESM-CHEM</b>	26.39	41.47	33.93	18
<b>MPI-ESM-LR</b>	26.33	48.67	37.50	21
<b>MPI-ESM-MR</b>	15.15	23.50	19.33	5
<b>MRI-CGCM3</b>	29.50	50.90	40.20	22
<b>NorESM1-M</b>	19.71	20.62	20.16	6
<b>All-model mean</b>	<b>27.60</b>	<b>29.86</b>	<b>29.41</b>	--

<sup>1</sup> All-model mean excludes INM-CM4.<sup>2</sup> All-model mean excludes GFDL-ESM2G, HadESM2-CC, and IPSL-CM5A-LR.

**Table 4.11** The overall model ranking, with respect to NCEP, for the Historical and RCP85 time periods. The ranking value is the sum of the SSI and DF.

Model	Historical <sup>1</sup>	RCP85-2 <sup>2</sup>	Average <sup>1,2</sup>	Rank
<b>ACCESS1-0</b>	50.42	22.10	36.26	10
<b>BCC-CSM1.1</b>	29.61	60.90	45.26	14
<b>BNU-ESM</b>	34.52	84.18	59.35	18
<b>CanESM2</b>	32.29	130.14	81.22	24
<b>CCSM4</b>	31.25	53.00	42.13	13
<b>CNRM-CM5</b>	41.95	102.84	72.39	23
<b>FGOALS-g2</b>	37.21	13.24	25.22	3
<b>FGOALS-s2</b>	46.34	24.86	35.60	8
<b>FIO-ESM</b>	26.09	14.78	20.44	1
<b>GFDL-CM3</b>	52.69	43.44	48.06	16
<b>GFDL-ESM2G</b>	25.26	159.20	92.23	25
<b>GFDL-ESM2M</b>	55.86	8.38	32.12	7
<b>GISS-E2-R</b>	51.36	20.08	35.72	9
<b>HadGEM2-AO</b>	47.58	47.78	47.68	15
<b>HadGEM2-CC</b>	69.28	119.78	94.53	26
<b>HadGEM2-ES</b>	49.25	5.96	27.61	5
<b>INM-CM4</b>	63.53	16.68	40.10	11
<b>IPSL-CM5A-LR</b>	69.78	206.98	138.38	27
<b>IPSL-CM5A-MR</b>	48.01	1.02	24.52	2
<b>IPSL-CM5B-LR</b>	69.43	74.26	71.84	22
<b>MIROC5</b>	27.25	56.24	41.75	12
<b>MIROC-ESM</b>	59.14	62.30	60.72	19
<b>MIROC-ESM-CHEM</b>	76.85	64.94	70.89	21
<b>MPI-ESM-LR</b>	36.67	77.34	57.01	17
<b>MPI-ESM-MR</b>	17.73	36.00	26.87	4
<b>MRI-CGCM3</b>	43.17	80.80	61.98	20
<b>NorESM1-M</b>	24.57	31.24	27.90	6

<sup>1</sup> All-model mean excludes INM-CM4.

<sup>2</sup> All-model mean excludes GFDL-ESM2G, HadESM2-CC, and IPSL-CM5A-LR.

## 4.6 Relationship with surface climate

### 4.6.1 Correlation analysis

#### 4.6.1.1 *Near-surface temperature*

A model's ability to reproduce the PNA pattern translates into how well the model simulates long-term climate of North America, particularly for strongly related surface temperature and precipitation. Although a model may accurately simulate global climate changes based on the analyses present in the previous sections, resolving these changes on regional scales is imperative to capture climate extremes that are of great concern when considering mitigation and policymaking. The locations and strengths of the three centers of action that define the PNA pattern ultimately determine these related surface climate connections and the strength of the anomalies associated with the PNA patterns directly relate to the magnitude of the surface anomalies. The barotropic instability associated with fluctuations between positive and negative PNA phases is characterized by cold troughs and warm ridges, such that during positive (negative) phases the general regions of P1 and P3 are cold (warm) and P2 is warm (cold). That is, the positive correlation between geopotential heights and temperature translates to a negative correlation between the PNA and surface temperature.

This relationship between PNA phase and surface temperature is resolved in all of the CMIP5 models but, due to the variability in the models' loading patterns, there are some relatively large differences in structure and magnitude for both future time periods (Fig. 4.9). The temperature correlation patterns are consistent with the PNA

loading patterns (Fig. 4.4), such that the strength of the loading pattern center (P1, P2, and P3) is proportional to the strength of the correlation between the PNA and surface temperature in that region. Similar to the Historical analysis, the correlations in the models are weaker than those in NCEP, especially over the North Pacific. Nine models in RCP85 fail to produce a coherent region of negative correlations in the North Pacific, which we attribute to a weak geopotential height anomaly, a misplaced P1 center, or both (e.g., CanESM2 and MIROC-ESM).

Compared to the Historical analysis, most CMIP5 models exhibit a weakened correlation associated with the P2 center, consistent with the anomaly strength analysis in Section 4.4.2.2 (Table 4.8). Due to the diminished P1 center in CanESM2, positive correlations with temperature are present throughout the entire PNA sector. Similar, but less severe, cases occur in five other models (e.g., IPSL-CM5A-MR and MIROC-ESM-CHEM). The negative-positive-negative pattern, as seen in NCEP, generally exists for each of the CMIP5 models in RCP85, yet for many models the relationship is less structured (e.g., HadGEM2-ES and MRI-CGCM3). We attribute this primarily to weaker height anomalies for all three centers, an indication that either the simulated future PNA pattern deviates substantially from the known historical pattern, or that many climate models cannot accurately simulate the PNA-temperature relationship under a changing climate.

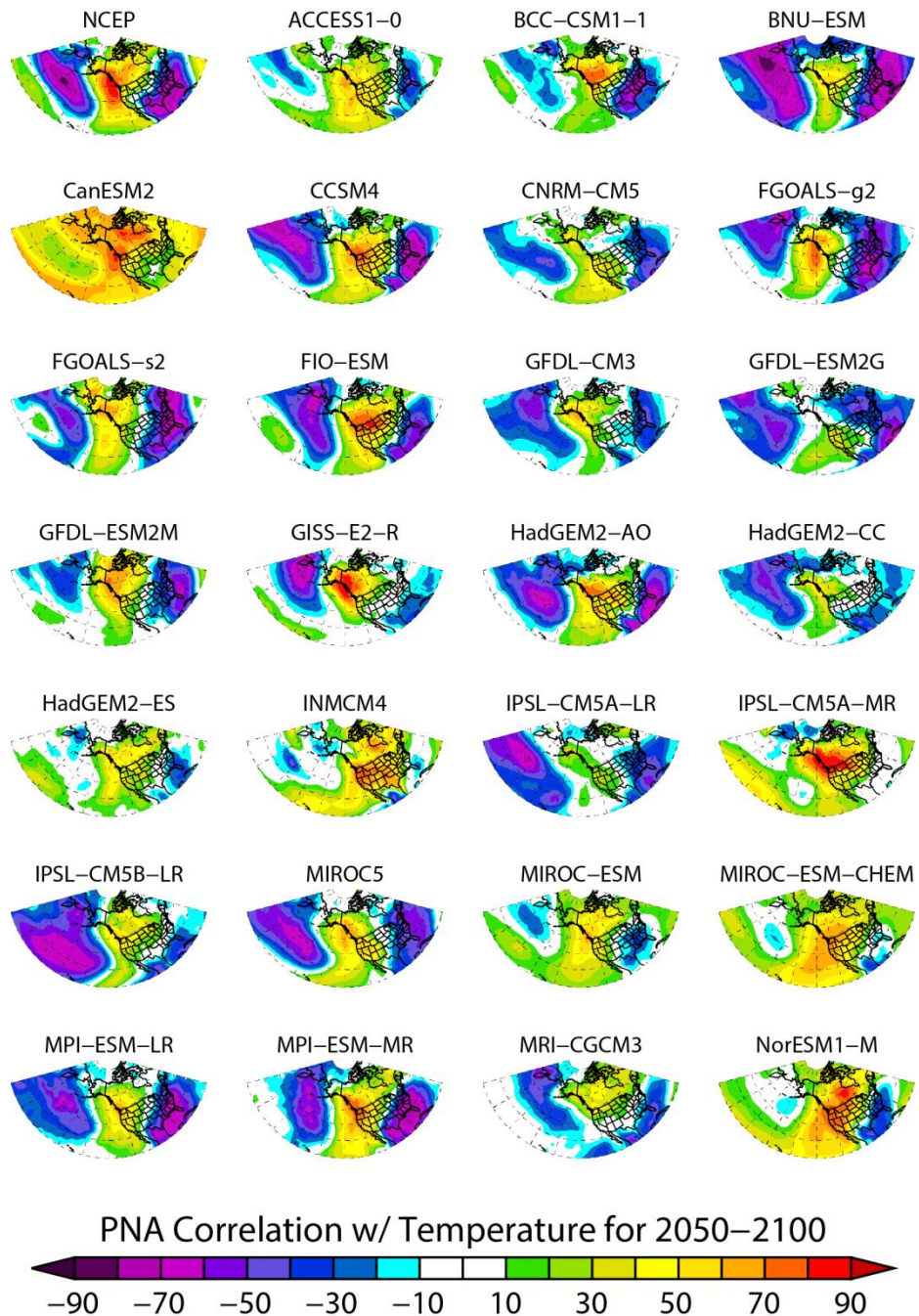


**Figure 4.9** The temporal correlation between the 2-m surface temperature anomalies and the PNA index for the month of January relative to the DJF winter season for RCP85. The historical NCEP map is displayed for comparison.

#### *4.6.1.2 Precipitation*

In both NCEP and the CMIP5 models correlations between the PNA and precipitation are generally weaker than those with temperature, although some distinct patterns exist (Fig. 4.10). Negative (positive) geopotential height anomalies are associated with low (high) pressure and increased (decreased) storminess. The most prominent feature in the NCEP precipitation pattern is the dipole between positive and negative correlations over the Pacific Ocean, which is driven by the Aleutian low at P1. The widespread region of positive correlations off the west coast of North America in the NCEP field are associated with the winter jet stream and “Pineapple Express” events, a robust feature of North American climate. Strong negative height anomalies associated with positive PNA events pull warm, moist air from Hawaii toward the west coast of the U.S. resulting in increased precipitation over the cooler eastern Pacific. Much of North America is covered by negative correlations due to the ridging over Canada. During negative PNA events when air flow is more zonal across North America, the U.S. Rocky Mountains and Appalachians receive increased precipitation due to the orographic effects of the mountain range. The lee side of the Rocky Mountains and the Southwest experience a zero correlation with precipitation, likely due to low precipitation amounts in these regions overall.

Most of the CMIP5 models capture the dipole over the Pacific Ocean in RCP85, but exhibit substantial differences across the rest of North America. About half of the models produce a region of positive correlation that, compared to NCEP, is too concentrated and does not feature the “tongue” that extends westward from the

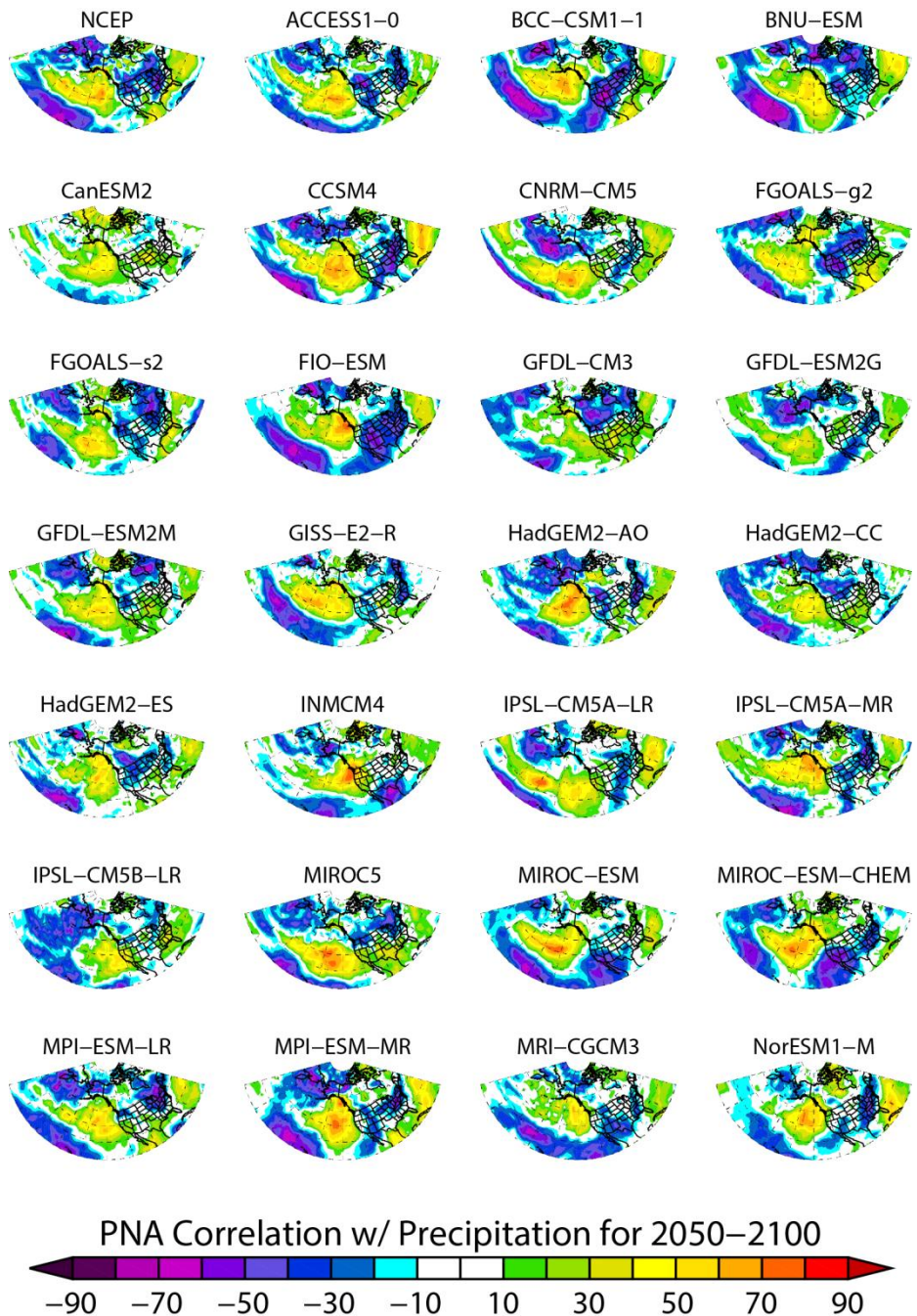


**Figure 4.10** As in Fig. 4.9, for the precipitation rate anomalies.

continent or does not influence a large enough section of the west coast or both (e.g., BCC-CSM1-1, GFDL-ESM2M, and HadGEM2-ES). Several models overestimate the strength of the negative correlation over North America as consequence of an extension of the P2 anomalies southwest toward, and sometimes connecting to, the subtropical high over Hawaii (e.g., BNU-ESM and FGOALS-s2).

Changes in the precipitation correlation patterns between the historical and future time periods are generally smaller and less organized than those for temperature, partly due to the natural variability of precipitation. The area of largest discrepancy between the two time periods is the west coast of North America. Shifts in the positioning and changes in the height anomaly magnitudes of P1 and P2—the quantities measured by the SSI—largely affect the location of the positive precipitation correlation over the eastern Pacific. An westward-shifted P1 and P2, as exhibited by many models, will pull moisture offshore, creating a drying effect in the coastal regions that were once under a positive correlation. Furthermore, the shift of P2 creates a region of negative correlation in the North Pacific and into Alaska, producing a complete reversal in sign in the region around the Aleutian Islands.

#### 4.6.2 Extreme events

We create composite anomaly maps for the top and bottom 33% of PNA indices to show the behavior of the North American climate in response to strong positive and negative PNA events. The magnitude of the temperature anomalies associated with positive and negative PNA phases should generally resemble the

patterns displayed in the correlation maps. The temperature data for RCP85 is detrended to remove the effects of global warming. For most CMIP5 models, the average winter temperature over North America increases  $\sim 3^{\circ}\text{C}$  between 2050 and 2100, justifying the need for detrending before performing the extremes analysis (Fig. 4.11). For reference, the map showing the Historical values for NCEP is located in the upper left corner of each figure. We use the notation “PNA+” for extreme positive PNA and “PNA-“ for extreme negative PNA.

#### *4.6.2.1 Near-surface temperature*

The CMIP5 temperature anomaly patterns for the future are consistent with the correlation patterns: those models that produce a recognizable PNA loading pattern also produce an anomaly pattern that more closely resembles NCEP (Figs. 4.12-4.13). The difference between the magnitudes of the 500-hPa height anomalies of the three centers is especially important in controlling the strength of the temperature anomalies associated with both PNA+ and PNA- events. If P2 is substantially stronger than P1 or P3, during strong PNA+ events any negative temperature anomalies associated with the P1 or P3 centers are overwhelmed by the strength of the positive anomalies associated with the P2 center (e.g., INM-CM4 and MIROC-ESM-CHEM in Fig. 4.12). Compared with the Historical analysis, however, most models exhibit a decrease in the strength or the areal extent of the positive temperature anomaly, or both, associated with P2 due to a weakening or shrinking of particularly the Aleutian low. The “Pineapple Express” associated with PNA+ brings warm air from the subtropics,

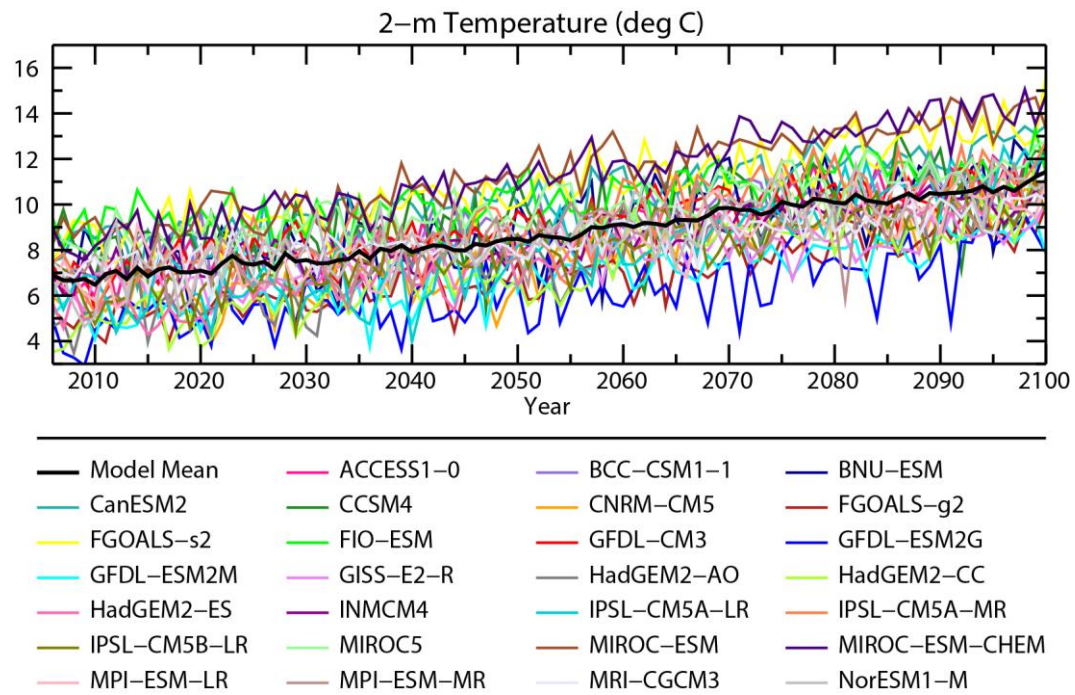


**Figure 4.11** Near-surface temperature for the DJF winter months averaged over North America for the years 2006-2100.

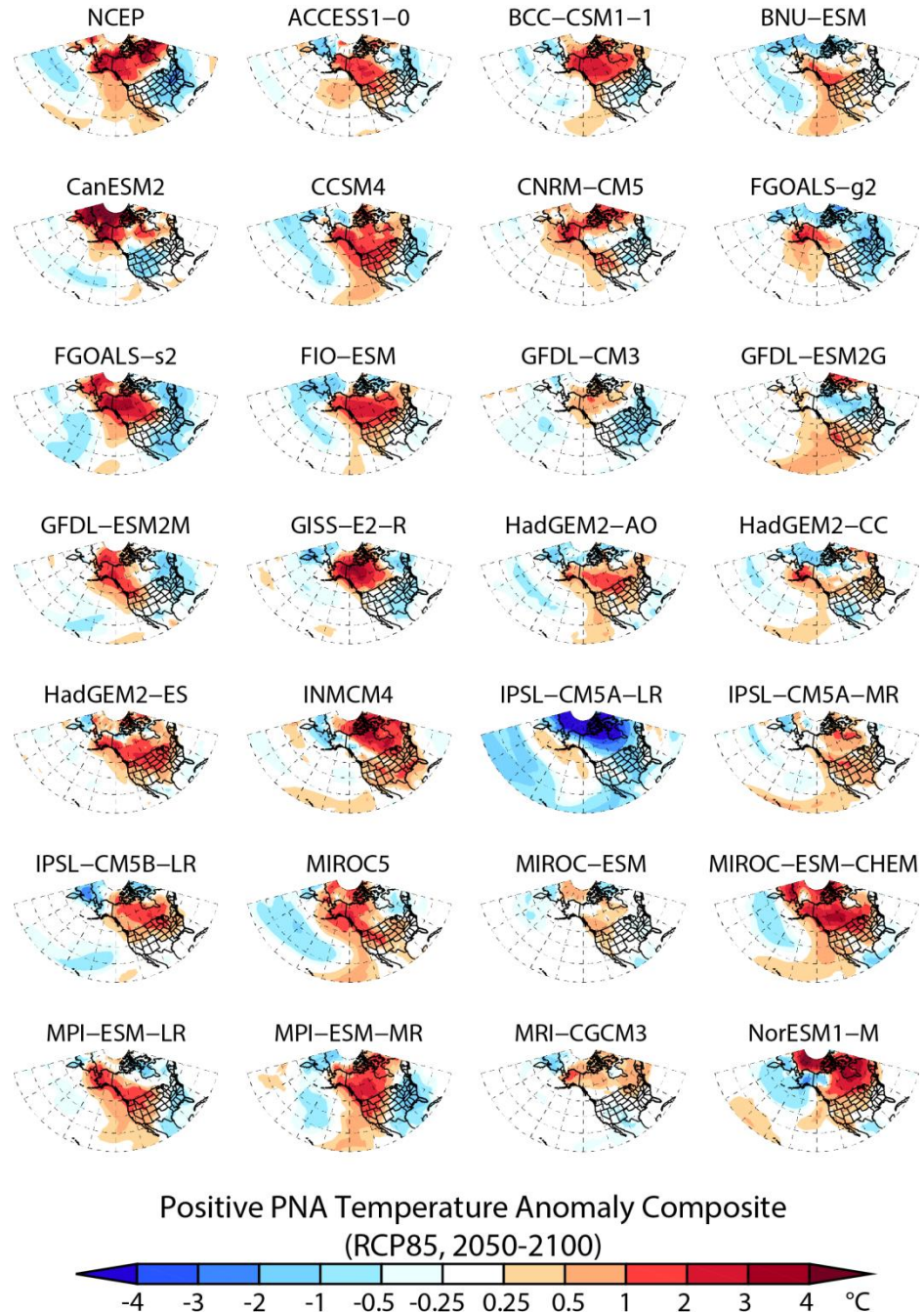


**Figure 4.12** Composite maps for the temperature anomalies during the top 33% of positive PNA years for RCP85. Anomalies are taken from the 2050-2100 climatology.

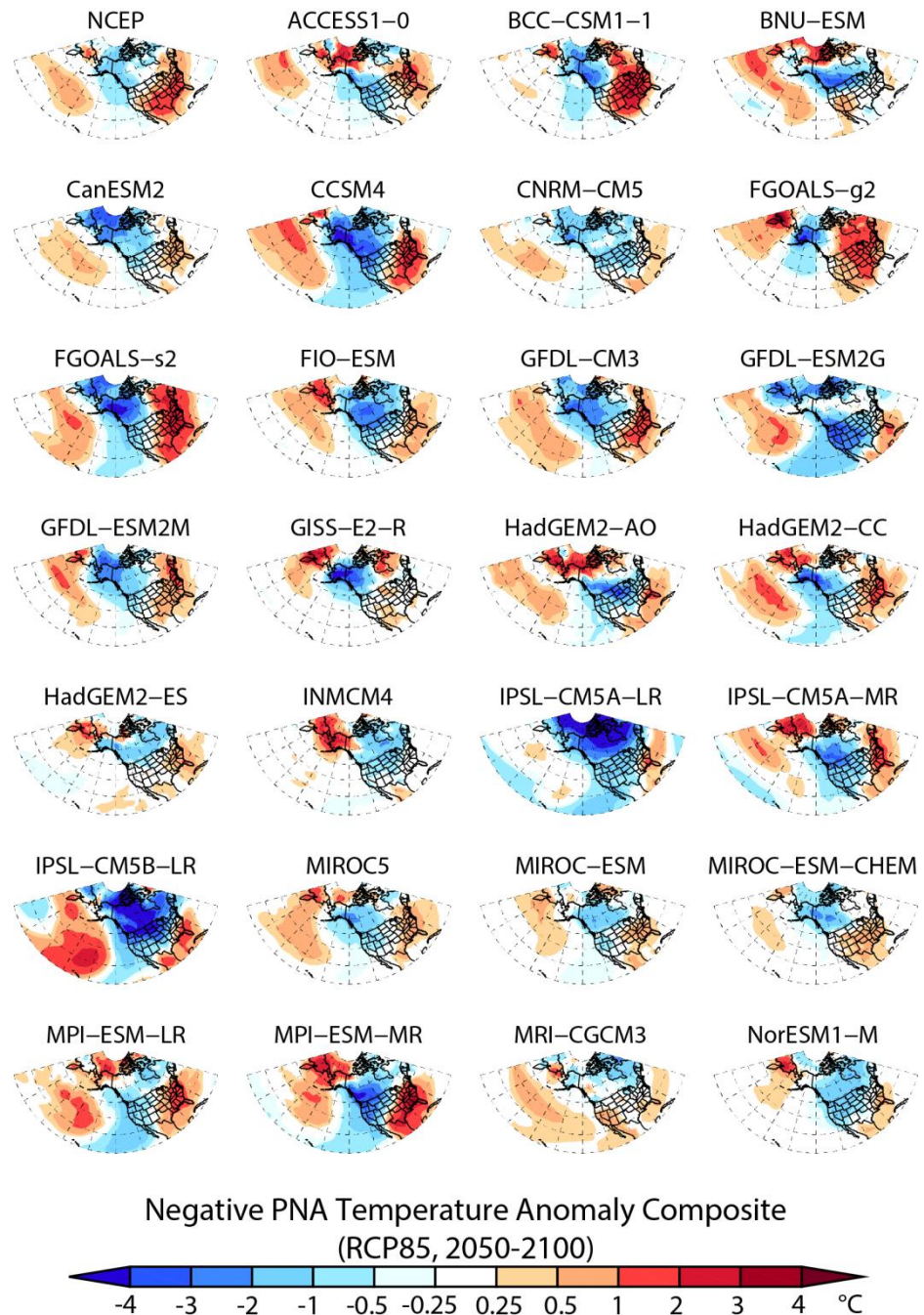


**Figure 4.13** As in Fig. 4.12, for the bottom 33% of negative PNA years.

which contributes to the magnitude of the positive temperature anomalies at P2. If the Aleutian low is too weak, the atmospheric conveyor belt that brings this warmth and moisture toward North America is also considerably weaker (e.g., GFDL-CM3 and MRI-CGCM3).

The PNA- temperature anomalies are near-opposites of the PNA+ patterns (Fig. 4.13). The same CMIP5 models that produced widespread positive anomalies during PNA+ events also produce widespread negative anomalies during PNA- events (e.g., CanESM2, MIROC-ESM-CHEM, and NorESM1-1). Models with high SSI values that do not adequately reproduce the shift in flows between PNA+ and PNA- events produce negative temperature anomalies that are too strong and/or too far south over western North America (see Table 4.9; e.g. CNRM-CM5, IPSL-CM5B-LR, and MPI-ESM-LR). Additionally, many models continue to overestimate the positive anomalies over the Pacific Ocean, a consequence of a dominant P1 center relative to P2.

#### *4.6.2.2 Precipitation*

As in the correlation analysis between the PNA and precipitation, the most prominent PNA+ feature in NCEP is the dipole between positive and negative precipitation anomalies over the Pacific Ocean (Fig. 4.14). The positive anomalies in this region reach ~2 mm/day in the positive area and 1 mm/day in the negative area surrounding Hawaii. Precipitation throughout most of Canada, the central U.S., and much of Mexico appears unaffected by both PNA+ and PNA- events, as evidenced by

neither positive nor negative anomalies for either case. The NCEP patterns associated with PNA- are comparably weaker than those with PNA+ (Fig. 4.15). A region of negative anomalies up to -1.5 mm/day appear over the North Pacific, a response to the high pressure associated with P1 during PNA-, with scattered areas of 0.5-1 mm/day positive anomalies to the north and south. The remainder of the PNA sector is largely unaffected, except for a few scattered regions of ~0.5 mm/day positive anomalies across the U.S.

Changes in RCP85 compared to the Historical simulation vary according to the individual model's representation of the PNA pattern. Only about one-quarter of the CMIP5 models reproduce the north-south dipole between positive and negative precipitation anomalies for PNA+ events in both Historical and RCP85 (Fig. 4.14). In most cases, the anomalies over the Pacific Ocean lack coherence and strength, suggesting a disrupted flow that fails to pull sufficient moisture out of the subtropics or that these models show no distinction in flow between PNA+ and PNA- (e.g., CNRM-CM5, GFDL-CM3, and MIROC-ESM). Accordingly, each of these models exhibit either a weak geopotential height anomaly at P1 or relatively high SSI values (refer to Fig. 4.7 and Table 4.9). Those models that do feature a coherent region of increased precipitation over the North Pacific often position them too far south and east, and the influence moves over land in many cases. We attribute this shift in location to a shifted P1 center that forces the airflow trajectory to the south and allows precipitation to make landfall over the west coast of the U.S (e.g., INM-CM4, IPSL-CM5A-MR, and MIROC5). Several models also misrepresent the negative anomaly

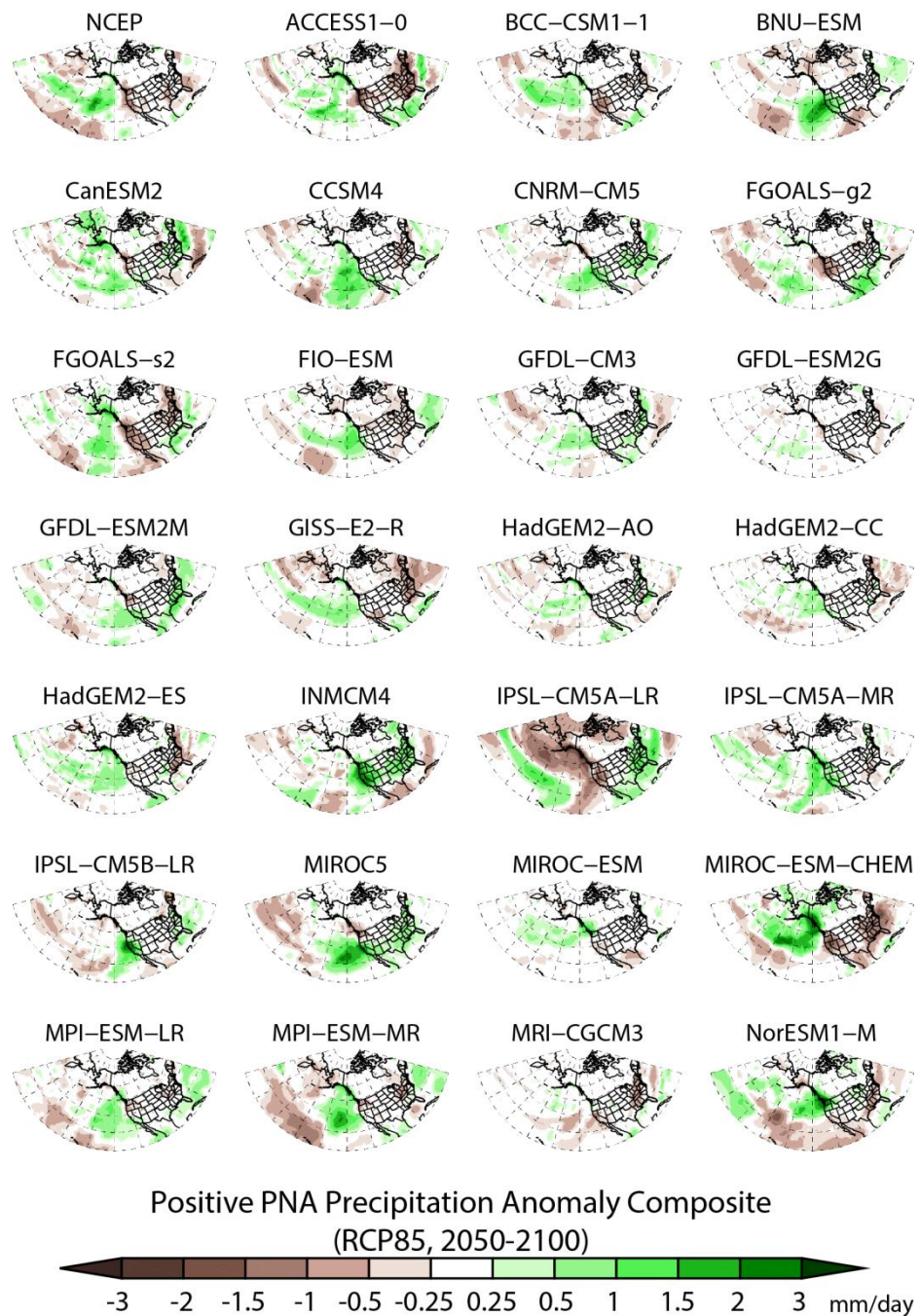


**Figure 4.14** Composite maps for the precipitation anomalies during the top 33% of positive PNA years for RCP85. Anomalies are taken from the 2050-2100 climatology.

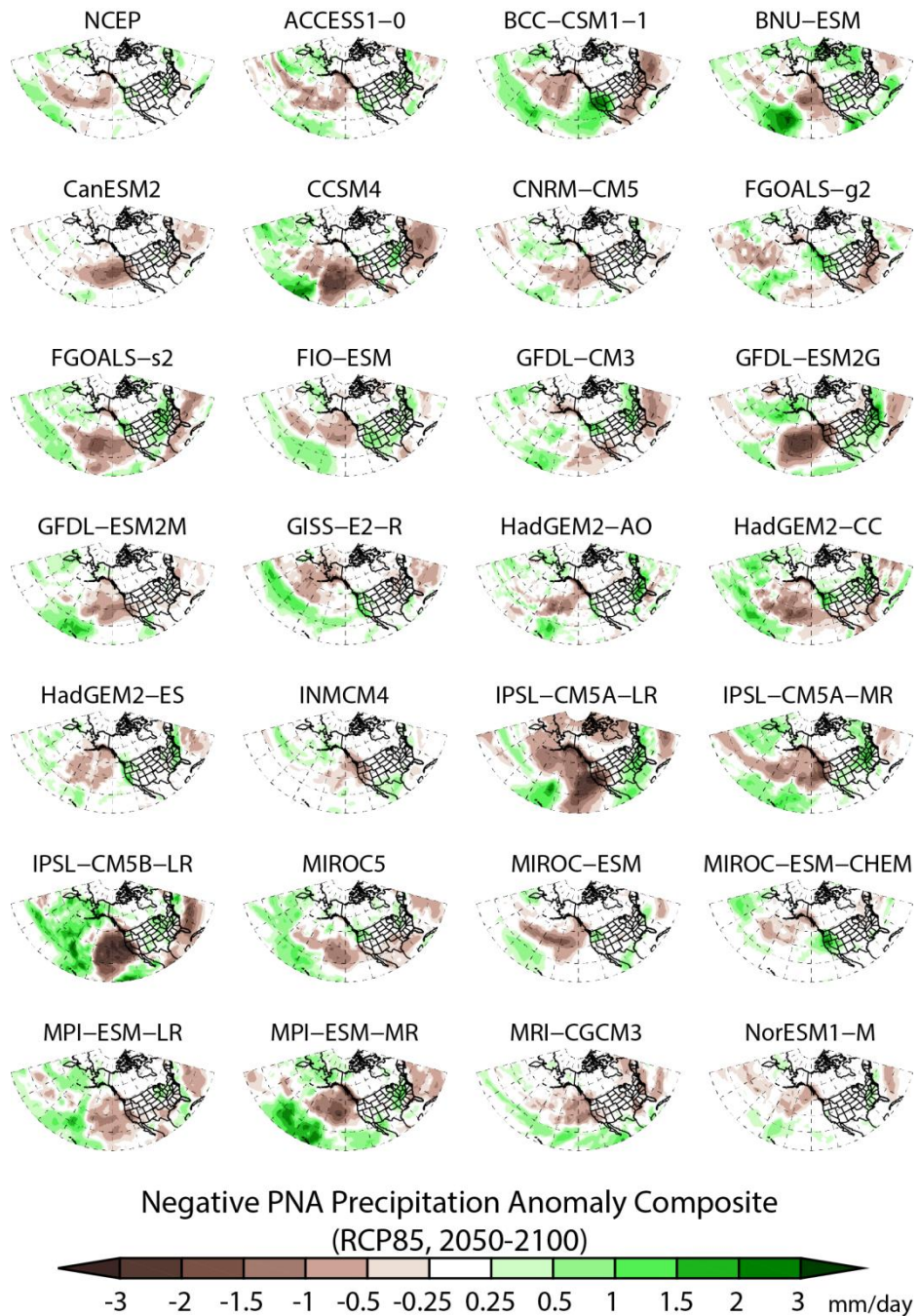


**Figure 4.15** As in Fig. 4.14, for the bottom 33% of negative PNA years.

over the southeast U.S. as a result of a too strong P3 height anomaly, which likely pulls moisture from the warm Gulf of Mexico waters (e.g., FIO-ESM and GFDL-CM3).

The most prominent feature among the CMIP5 models for PNA- events is the large negative precipitation anomaly off the west coast of North America relative to NCEP, which increases in strength by the end of the 21<sup>st</sup> century (Fig. 4.15). This region is much too dry in at least half of the models, particularly in CCSM4 and IPSL-CM5B-LR (IPSL-CM5A-LR does not represent the PNA in RCP85). We associate this anomaly with a P1 center that is too strong and too widespread, which, during PNA- events, creates subsidence that dries out the air and suppresses precipitation formation. Several models also show a positive anomaly near the subtropics that, compared to NCEP, is also too strong and shifted too far north (e.g., BNU-ESM and MRI-ESM-MR). We attribute this to the influence of the relative low pressure over Hawaii. Similar to the Pineapple Express in PNA+, regions of low pressure in the extratropics pull warm, moist air northward where it precipitates as it moves over cooler ocean waters. A subtropical center that is too strong and shifted too far north will carry these positive precipitation anomalies north, as well.

#### *4.6.2.3 The “neutral zone”*

While many models exhibit large changes in both temperature and precipitation anomaly patterns in one area of the PNA sector, changes are more subtle and less pronounced in other areas, making them appear inconsequential on a global

scale. These smaller changes, however, can have large impacts on climate at the regional level. The location of the “neutral zone”, or the transition between areas of positive and negative anomalies, largely influences the climate for the regions within and on either side of the zone. Shifts in the neutral zone can mean the differences between, for example, anomalously warm and dry or anomalously cold and wet conditions, especially on seasonal or annual time scales.

The location of the neutral zone varies widely among the models for all time periods. NCEP displays a distinct line of zero temperature anomalies for PNA+ and PNA- (Figs. 4.12 and 4.13) that extends north from Baja California, then east across the United States and north through eastern Canada. For PNA+ events, regions north of this zone experience warmer than normal temperatures, while regions to the south experience cooler than normal temperatures. The historical analysis showed that most models positioned this zone too far south, a consequence of a weak P3 center relative to P2. Similar discrepancies appear for RCP85, where in nearly half of the models the area of negative temperature anomalies associated with P3 is too small and/or too weak, which pulls the neutral zone south and creates warmer (cooler) than normal conditions over most of the United States during PNA+ (PNA-).

The neutral zone is less defined in the precipitation correlation maps, but is largely influential along the length of the west coast of North America (Figs. 4.14 and 4.15). The region of positive precipitation anomalies just off the west coast is highly sensitive to both the strength and position of the Aleutian low (P1 center). A deepening of the low or small shifts to the east push the positive precipitation

correlations onto land, bringing anomalously wet conditions to coastal regions that may otherwise experience “normal” conditions under the neutral zone. About one-third of the models in RCP85 display positive precipitation anomalies over the west coast, a feature that produces largely different climates over land compared to those models that keep the moisture over the ocean.

#### 4.7 Conclusions

Our analysis of 27 CMIP5 AOGCMs and ESMs reveals that the Pacific-North American teleconnection persists in future climate simulations through the year 2100. In Part I of this study, we found that individual differences among the models, such as grid resolution, model complexity, and parameterization schemes, led to substantial differences in the ability of those models to simulate the PNA. These differences persist under the RCP85 future climate scenario, and while individual models exhibit varying temporal and spatial PNA patterns, the models reveal several general and important trends.

The temporal analysis revealed that on a monthly time scale the models still produce index time series that are too periodic and do not capture the natural variability and noise present in the climate system. We found that many of the models produce more power at much lower frequencies, a symptom of these models becoming “locked” into a positive or negative PNA mode during the winter season. The mean model indices trend toward more positive values in the future, indicating a shift

toward more meridional flows and more ridging over the western half of North America.

Spatial variability among the models increases substantially, although the models reveal a general lengthening of the 500-hPa wave field over the North Pacific and North America, as indicated by a westward shift of P1 and P2 and an eastward shift of P3. Furthermore, several models suggest a possible poleward shift of the PNA pattern. These results confirm studies that show a lengthening of the eddy length scale accompanied by a poleward shift of mid-latitude jet streams (Chase et al., 2000; Kidston et al., 2010; Kidston et al., 2011). Overall, the strengths of the anomalies remain significantly weaker than NCEP throughout the 21<sup>st</sup> century, suggesting that simulated PNA patterns are generally “less robust” than the observations. The NCEP/NCAR Reanalysis reveals the PNA teleconnection as the second leading mode of a rotated-EOF analysis, explaining 13% of the variance in the 500-hPa geopotential height field (Fig. 3.4). While the CMIP5 models consistently reveal the PNA as one of the ten leading modes, the amount of explained variance is often quite small compared to NCEP (Tables 3.3 and 4.4). This indicates that the PNA is less prominent, or “less robust”, than other physical processes and teleconnections in the CMIP5 models’ 500-hPa height fields.

A model’s ability to produce a recognizable PNA pattern largely depends on the presence and location of a P2 center. The P1-P2 relationship determines a model’s ability to reproduce the see-saw between meridional and zonal flows, while the P2-P3 is responsible for the correct positioning of the neutral zone, especially for temperature

correlations. Because the correlation and anomaly patterns with temperature and precipitation depend so heavily on the structure of the PNA, the variability among the CMIP5 models' loading patterns in both future time periods creates similar variability in these surface climate variables. Nonetheless, analyzing these relationships is important for understanding the influence of the PNA on surface climate, as temperature and precipitation drive other surface variables such as soil moisture, snowpack, and runoff.

While the CMIP5 models are able to consistently produce a PNA pattern, the disagreement among models regarding the evolution of the teleconnection illustrates the complexity of the climate system and the uncertainties present in individual climate models. Because future observations do not exist, we therefore base any future model assessments on their performance in the historical analysis relative to NCEP and on their consistency between the Historical and RCP85 simulations. FIO-ESM emerges as the most consistent model in terms of reproducing the PNA pattern throughout the 21<sup>st</sup> century, as well as in its comparison to NCEP. While the performance ranking of most models remains relatively consistent between the Historical and RCP85 time periods, we find that assuming a model's future performance based on its evaluation against NCEP is sometimes misleading. Compared to a high ranking in the Historical analysis, the ability of several models to reproduce the PNA pattern diminished greatly in RCP85 (e.g., CanESM2, GFDL-ESM2G, and MIROC5). Opposite cases are true for GFDL-ESM2M and IPSL-CM5A-MR whose rankings improved relative to NCEP under the future scenario.

Consequently, the model performance results presented here are subjective and model consistency must also be considered. Furthermore, due to limited data availability, the analyses performed in this study utilized only one ensemble member for each simulation. Ensemble means, which include several simulations starting from varying locations within the control run, might better capture of the natural variability within the climate system and lead to a better representation of large-scale atmospheric dynamics. The analysis provided here is only a baseline for future studies.

#### 4.8 Acknowledgements

We acknowledge the World Climate Research Programme's Working Group on Coupled Modelling, which is responsible for CMIP, and we thank the climate modeling groups (listed in Table 3.1 of this paper) for producing and making available their model output. For CMIP the U.S. Department of Energy's Program for Climate Model Diagnosis and Intercomparison provides coordinating support and led development of software infrastructure in partnership with the Global Organization for Earth System Science Portals. Funding for this research was provided by the U.S. Geological Survey.

#### 4.9 References

Abatzoglou, J.T. (2010): Influence of the PNA on declining mountain snowpack in the Western United States. *Intl. J. Clim.*, 8 pp.

- Bao, Q., G. Wu, Y. Liu, J. Yang, Z. Wang, T. Zhou (2010): An introduction to the coupled model FGOALS1.1-s and its performance in East Asia. *Adv. Atmos. Sci.*, **27**(5), 1131-1142.
- Barnston, A.G. and R.E. Livezey (1987): Classification, seasonality and persistence of low-frequency atmospheric circulation patterns. *Mon. Wea. Rev.*, **115**, 1083-1126.
- Bi, D. (2012): ACCESS: The Australian coupled climate model for IPCC AR5 and CMIP5. 2012 Australian Meteorological and Oceanographic Society (AMOS) Conference; Sydney, Australia: <https://wiki.csiro.au/confluence/display/ACCESS/ACCESS+Publications>.
- Chase, T.N., R.A. Pielke Sr., T.G.F. Kittel, R.R. Nemani, and S.W. Running (2000): Simulated impacts of historical land cover changes on global climate in northern winter. *Clim. Dyn.*, **16**, 93-105.
- Chen, W.Y. and H. van den Dool (2003): Sensitivity of teleconnection patterns to the sign of their primary action center. *Mon. Wea. Rev.*, **131**, 2885-2899.
- Chylek, P., J. Li, M.K. Dubey, M. Wang, and G. Lesins (2011): Observed and model simulated 20th century Arctic temperature variability Canadian Earth System Model CanESM2. *Atmos. Chem. Phys. Discuss.*, **11**, 22893-22907.
- Collins, N. Bellouin, M. Doutriaux-Boucher, N. Gedney, Hinton, C.D. Jones, S. Liddicoat, G. Martin, F. O'Connor, Rae, C. Senior, I. Totterdell, S. Woodward, Reichler, and J. Kim (2008): Evaluation of the HadGEM2 model. Hadley Centre technical note 74, 47 pp.
- Donner, L.J., B.L. Wyman, R.S. Helmer, L.W. Horowitz, Y. Ming, M. Zhao, J.-C. Golaz, P. Ginoux, S.-J. Lin, M.D. Schwarzkopf, J. Austin, G. Alaka, W.F. Cooke, T.L. Delworth, S.M. Freidenreich, C.T. Gordon, S.M. Griffies, I.M. Held, W.J. Hurlin, S.A. Klein, T.R. Knutson, A.R. Langenhorst, H.-C. Lee, Y. Lin, B.I. Magi, S.L. Malyshev, P.C.D. Milly, V. Naik, M.J. Nath, R. Pincus, J.J. Ploshay, V. Ramaswamy, C.J. Seman, E. Shevliakova, J.J. Sirutis, W.F. Stern, R.J. Stouffer, R.J. Wilson, M. Winton, A.T. Wittenberg, and F. Zeng (2011): The dynamical core, physical parameterizations, and basic simulation characteristics of the atmospheric component AM3 of the GFDL global coupled model CM3. *J. Climate*, **24**, 3484-3519.
- Dufresne, J.-L., M.-A. Foujols, S. Denvil, A. Caubel, O. Marti, O. Aumont, Y. Balkanski, S. Bekki, H. Bellenger, R. Benshila, S. Bony, L. Bopp, P. Braconnot, P. Brockmann, P. Cadule, F. Cheruy, F. Codron, A. Cozic, D. Cugnet, N. de Noblet, J.-P. Duvel, C. Ethé, L. Fairhead, T. Fichefet, S. Flavoni, P. Friedlingstein, J.-Y. Grandpeix, L. Guez, E. Guilyardi, D. Hauglustaine, F. Hourdin, A. Idelkadi, J.

Ghattas, S. Joussaume, M. Kageyama, G. Krinner, S. Labetoulle, A. Lahellec, M.-P. Lefebvre, F. Lefevre, C. Levy, Z.X. Li, J. Lloyd, F. Lott, G. Madec, M. Mancip, M. Marchand, S. Masson, Y. Meurdesoif, J. Mignot, I. Musat, S. Parouty, J. Polcher, C. Rio, M. Schulz, D. Swingedouw, S. Szopa, C. Talandier, P. Terray, and N. Viovy (2012): Climate change projections using the IPSL-CM5 Earth System Model: From CMIP3 to CMIP5. *Clim. Dyn.*, submitted, 53 pp.

Dunne, J.P., J.G. John, A.J. Adcroft, S.M. Griffies, R.W. Hallberg, E. Shevliakova, R.J. Stouffer, W. Cooke, K.A. Dunne, M.J. Harrison, 8 J.P. Krasting, S.L. Malyshev, P.C.D. Milly, P.J. Phillipps, L.A. Sentman, B.L. Samuels, M.J. Spelman, M. Winton, A.T. Wittenberg, N. Zadeh (2012): GFDL's ESM2 global coupled climate-carbon Earth System Models Part I: Physical formulation and baseline simulation characteristics. *J. Climate* [Early online release: <http://journals.ametsoc.org/doi/pdf/10.1175/JCLI-D-11-00560.1>], 64 pp.

Ganguly, A.R., K. Steinhaeuser, D.J. Erikson III, M. Branstetter, E.S. Parish, N. Singh, J.B. Drake, and L. Buja (2009): Higher trends but larger uncertainty and geographic variability in 21st century temperature and heat waves. *PNAS*, **106**(37), 15555-15559.

Gent, P.R., G. Danabasoglu, L.J. Donner, M.M. Holland, E.C. Hunke, S.R. Jayne, D.M. Lawrence, R.B. Neale, P.J. Rasch, M. Vertenstein, P.H. Worley, Z-L. Yang, M. Zhang (2011): The Community Climate System Model Version 4. *J. Climate*, **24**, 4973-4991.

Gilman, D.L., F.J. Fuglister, and J.M. Mitchell Jr. (1963): On the power spectrum of “red noise”. *J. Atmos. Sci.*, **20**, 182-184.

Hourdin, F., M.-A. Foujols, F. Codron, V. Guemas, J.-L. Dufresne, S. Bony, S. Denvil, L. Guez, F. Lott, J. Ghattas, P. Braconnot, O. Marti, Y. Meurdesoif, L. Bopp (2012): Impact of the LMDZ atmospheric grid configuration on the climate and sensitivity of the IPSL-CM5A coupled model. *Clim. Dyn.*, submitted, 39 pp.

IPCC (2007): Climate Change 2007: The Physical Science Basis. Contribution of Working Group I to the Fourth Assessment Report of the Intergovernmental Panel on Climate Change [Solomon, S., D. Qin, M. Manning, Z. Chen, M. Marquis, K.B. Averyt, M. Tignor and H.L. Miller (eds.)]. Cambridge University Press, Cambridge, United Kingdom and New York, NY, USA.

Jungclaus J.H., S.J. Lorenz, C. Timmreck, C.H. Reick, V. Brovkin, K. Six, J. Segschneider, M.A. Giorgetta, T.J. Crowley, J. Pongratz, N.A. Krivova, L.E. Vieira, S.K. Solanki, D. Klocke, M. Botzet, M. Esch, V. Gayler, H. Haak, T.J. Raddatz, E. Roeckner, R. Schnur, H. Widmann, M. Claussen, B. Stevens, and J.

- Marotzke (2010): Climate and carbon-cycle variability over the last millennium. *Clim. Past*, **6**, 723-737.
- Kalnay, E., M. Kanamitsu, R. Kistler, W. Collins, D. Deaven, L. Gandin, M. Iredell, S. Saha, G. White, J. Woollen, Y. Zhu, A. Leetmaa, B. Reynolds, M. Chelliah, W. Ebisuzaki, W. Higgins, J. Janowiak, K.C. Mo, C. Ropelewski, J. Wang, R. Jenne, and D. Joseph (1996): The NCEP/NCAR 40-year reanalysis project. *Bull. Amer. Met. Soc.*, **77**, 437-471.
- Kidston, J., G.K. Vallis, S.M. Dean, and J.A. Renwick (2011): Can the increase in eddy length scale under global warming cause the poleward shift of the jet streams? *J. Climate*, **24**, 3764-3780.
- Kitoh, A., et al. (2007): Model development at MRI. 3rd China-Korea-Japan Joint Conference on Meteorology; Beijing, China.
- Le Quéré, C., M.R. Raupach, J.G. Canadell, G. Marland, L. Bopp, P. Ciais, T.J. Conway, S.C. Doney, R.A. Feely, P. Foster, P. Friedlingstein, K. Gurney, R.A. Houghton, J.I. House, C. Huntingford, P.E. Levy, M.R. Lomas, J. Majkut, N. Metzl, J.P. Ometto, G.P. Peters, I.C. Prentice, J.T. Randerson, S.W. Running, J.L. Sarmiento, U. Schuster, S. Sitch, T. Takahashi, N. Viovy, G.R. van der Werf, and F.I. Woodward (2009): Trends in the sources and sinks of carbon dioxide. *Nat. Geo.*, **2**, 831-836.
- Leathers, D.J., B. Yarnal, M.A. Palecki (1991): The Pacific/North American teleconnection pattern and United States climate. Part I: Regional temperature and precipitation associations. *J. Climate*, **4**, 517-528.
- Martin, G.M., N. Bellouin, W.J. Collins, I.D. Culverwell, P.R. Halloran, S.C. Hardiman, T. J. Hinton, C.D. Jones, R.E. McDonald, A.J. McLaren, F.M. O'Connor, M.J. Roberts, J.M. Rodriguez, S. Woodward, M.J. Best, M.E. Brooks, A.R. Brown, N. Butchart, C. Dearden, S.H. Derbyshire, I. Dharssi, M. Doutriaux-Boucher, J.M. Edwards, P.D. Falloon, N. Gedney, L.J. Gray, H.T. Hewitt, M. Hobson, M.R. Huddleston, J. Hughes, S. Ineson, W.J. Ingram, P.M. James, T.C. Johns, C.E. Johnson, A. Jones, C.P. Jones, M.M. Joshi, A.B. Keen, S. Liddicoat, A.P. Lock, A.V. Maidens, J.C. Manners, S.F. Milton, J.G.L. Rae, J.K. Ridley, A. Sellar, C.A. Senior, I.J. Totterdell, A. Verhoef, P.L. Vidale, and A. Wiltshire (2011): The HadGEM2 family of Met Office Unified Model Climate configurations. *Geosci. Mod. Dev. Discuss*, **4**, 765-841.
- Moss, R.H., J.A. Edmonds, K.A. Hibbard, M.R. Manning, S.K. Rose, D.P. van Vuuren, T.R. Carter, S. Emori, M. Kainuma, T. Kram, G.A. Meehl, J.F.B. Mitchell, N. Nakicenovic, K. Riahi, S.J. Smith, R.J. Stouffer, A.M. Thomson, J.P.

- Weyant, and T.J. Wilbanks (2010): The next generation of scenarios for climate change research and assessment. *Nature*, **463**, 747-756.
- Otterå, O.H. (2011): Simulating the climate from Paleocene to present-day and beyond: Challenges in climate modeling. 10th Annual Meeting on High Performance Computing and Infrastructure in Norway; Oslo, Norway.
- Rogelj, J., M. Meinshausen, and R. Knutti (2012): Global warming under old and new scenarios using IPCC climate sensitivity range estimates. *Nat. Clim. Change*, 6 pp.
- Simmons, A.J., J.M. Wallace, and G.W. Branstator (1983): Barotropic wave propagation and instability, and atmospheric teleconnection patterns. *J. Atmos. Sci.*, **40**(6), 1363-1392.
- Stoner, A.M.K., K. Hayhoe, and D.J. Weubbles (2009): Assessing general circulation model simulations of atmospheric teleconnection patterns. *J. Climate*, **22**, 4348-4372.
- Straus, D.M. and J. Shukla (2002): Does ENSO force the PNA? *J. Climate*, **15**, 2340-2358.
- Taylor, K.E., R.J. Stouffer, and G.A. Meehl (2012): An overview of CMIP5 and the experiment design. *Bull. Amer. Met. Soc.*, 485-498.
- van Vuuren, D.P., J. Edmonds, M. Kainuma, K. Riahi, A. Thomson, K. Hibbard, G.C. Hurtt, T. Kram, V. Kray, J.-F. Lamarque, T. Masui, M. Meinshausen, N. Nakicenovic, S.J. Smith, and S.K. Rose (2011): The representative concentration pathways: an overview. *Clim. Change*, **109**, 5-31.
- Voldoire, A., E. Sanchez-Gomez, D. Salas y Melia, B. Decharme, C. Cassou, S. Se'ne'si, S. Valcke, I. Beau, A. Alias, M. Chevallier, M. De'que', J. Deshayes, H. Douville, E. Fernandez, G. Madec, E. Maisonnave, M.-P. Moine, S. Planton, D. Saint-Martin, S. Szopa, S. Tyteca, R. Alkama, S. Belamari, A. Braun, L. Coquart, and F. Chauvin (2012): The CNRM-CM5.1 global climate model: description and basic evaluation. *Clim. Dyn.*, 31 pp.
- Volodin, E.M., N.A. Dianskii, and A.V. Gusev (2010): Simulating present-day climate with the INMCM4.0 coupled model of the atmospheric and oceanic general circulations. *Atm. Oc. Phys.*, **46**(4), 414-431.
- Wallace, J.M. and D.S. Gutzler (1981): Teleconnections in the geopotential height field during the Northern Hemisphere winter. *Mon. Wea. Rev.*, **109**, 784-812.

- Watanabe, M., T. Suzuki, R. O’Ishi, Y. Komuro, S. Watanabe, S. Emori, T. Takemura, M. Chikira, T. Ogura, M. Sekiguchi, K. Takata, D. Yamazaki, T. Yokohata, T. Nozawa, H. Hasumi, H. Tatebe, M. Kimoto (2010): Improved climate simulation by MIROC5: Mean states, variability, and climate sensitivity. *J. Climate*, **23**, 6312-6335.
- Watanabe, S., T. Hajima, K. Sudo, T. Nagashima, T. Takemura, H. Okajima, T. Nozawa, H. Kawase, M. Abe, T. Yokohata, T. Ise, H. Sato, E. Kato, K. Takata, S. Emori, and M. Kawamiya (2011): MIROC-ESM: Model description and basic results of CMIP5-20c3m experiments. *Geosci. Model Dev. Discuss.*, **4**, 1063-1128.
- Yu, Y., H. Zhi, B. Wang, H. Wan, C. Li, H. Liu, W. Li, W. Zheng, and T. Zhou (2008): Coupled model simulations of climate changes in the 20th century and beyond. *Adv. Atmos. Sci.*, **25**(4), 641-654.
- Zanchettin, D., A. Rubino, and J.H. Jungclaus (2010): Intermittent multidecadal-to-centennial fluctuations dominate global temperature evolution over the last millennium. *Geo. Res. Let.*, **37**(L14702), 6 pp.

## Chapter 5: Conclusions

This thesis focuses on understanding of the role of the Pacific-North American teleconnection in both global and regional climate models. The analyses provide a comprehensive qualitative and quantitative assessment of the presence of the PNA and its influence over climate in North America. The PNA is expressed as a robust pattern in all models analyzed in this thesis that persists under both historical and future climate simulations.

Chapter 2 challenges the accuracy of a nested RCM by analyzing the PNA in both the ECHAM5 GCM and the ECHAM5-forced RegCM3 output for the same time periods and under the same climate scenarios. The coupling between the NCEP and ECHAM5 GCMs with RegCM3 was very successful in that the PNA is resolved in both models with little loss of information between the GCM and RCM, allowing for a high-resolution assessment of climate with an inherent skill comparable to that of the global model used as a forcing.

The PNA index is generally independent of the calculation method used, as a three- and four-point modified linear pointwise calculation for both the RegCM3 and ECHAM5 model simulations reveal very comparable results to each other, and to the index extracted from an RPCA. These results persist in Chapters 3 and 4 for each of the 27 analyzed CMIP5 models. The computed PNA index under the A2 and RCP85 future climate scenarios used in Chapter 2 and Chapters 3 and 4, respectively, reveal a trend toward more frequent positive PNA events by the end of the 21<sup>st</sup> century. The ratios of positive-to-negative PNA events are substantially larger for the CMIP5

models under RCP85 than for ECHAM5 under the A2 scenario; the reason for this is attributed to either the magnitude of the warming in RCP85 compared to A2 (RCP85 projects warmer temperatures by 2100 than does A2), or selecting a single ECHAM5 model compared to the 27-model mean from CMIP5. Because the ECHAM5 model precedes the two CMIP5 MPI models, comparable model performance is assumed, especially at the 500-hPa level where the flow is geostrophic (e.g., unaffected by surface friction). The CMIP5 MPI models produce much larger ratios than ECHAM5 for the 2050-2100 index time series, suggesting that the differences between the RCP85 and A2 scenarios, or warmer global temperatures, are responsible for the increase in positive PNA events by the end of the 21<sup>st</sup> century. The trend toward positive indices also indicates a shift toward more meridional flows over the western half of North America. Maps of 500-hPa isohypsuses validate this finding and show increased ridging in this region associated with the P2 center of action.

The spatial pattern of the PNA teleconnection emerges as a leading mode of variability in a rotated-EOF analysis for each model analyzed, although the strength of the teleconnections is consistently weaker than NCEP. The evolution of the spatial patterns shows a lengthening of the 500-hPa geopotential height wave field, an observation consistent with projections of increasing eddy length scales under global warming. Results from Chapters 2 and 4 indicate a westward shift in the P1 and P2 centers, and an eastward shift of the P3 centers in ECHAM5 and the CMIP5 27-model mean by the end of the 21<sup>st</sup> century. Furthermore, the models suggest a poleward shift

of one or more of the PNA centers of action, also consistent with previous studies of the behavior of mid-latitude jets under a warming climate.

The PNA index is highly correlated with North American climate, notably winter temperature and precipitation. These relationships, in turn, lead to antecedent conditions and slightly less well-defined correlations between the PNA and summer soil moisture levels and late-spring snowpack. In Chapter 2, the correlation and anomaly patterns produced by the NCEP- and ECHAM5-forced RegCM3 simulations verify the ability of the models to downscale accurately the climatic influences of large-scale atmospheric dynamics onto a high-resolution grid. The correlation patterns associated with the PNA and surface climate variables produced by the regional NCEP simulation are remarkably similar to the global NCEP Reanalysis product available on the CPC website (online at: <http://www.cpc.ncep.noaa.gov/data/teledoc/pna.shtml>). Discrepancies are attributed to the limited temporal extent of the regional analysis, which excludes the first 30 years of the 1950-2000 time period.

The results from all three chapters reveal that the ability of a model to accurately reproduce the PNA spatial pattern is directly related to the positioning of the Aleutian low (P1) and Canadian high (P2), the two main drivers of upper-atmospheric circulation in the PNA sector, while the low over the southeast U.S. (P3) influences the patterns associated with the temperature and precipitation correlation and anomaly maps. The P1-P2 relationship determines a model's ability to reproduce the see-saw between meridional and zonal flows, while the P2-P3 relationship has a greater influence over the positioning of the zone that separates regions of positive and

negative PNA over North America, an important feature in defining the correlation and anomaly patterns.

Chapters 3 and 4 illustrate the differences between climate models and that their ability to simulate large-scale atmospheric phenomena depends heavily on model resolution, complexity, and parameterization schemes. Future model assessments are necessarily based on their simulation of present climate relative to NCEP and on their consistency between the present and future simulations. The conclusions from this thesis verify the robustness of multi-model and ensemble means, suggesting that the cumulative results of multiple climate models outperform the results from individual models and single model runs. Ensemble means effectively cancel large model-specific discrepancies thereby retaining only the most robust features of the model runs, which leads to a better representation of climate dynamics. While this thesis did not fully explore the advantages of ensemble means, the results presented here provide a sound baseline for understanding the role of the PNA in future climate modeling studies.